Technical Report Documentation Page

1. Report No.	2. Government Accession No.	3. Recipient's Catalog No.
FHWA/TX-05/0-2102-1		

4. Title and Subtitle	5. Report Date
BEHAVIOR AND DESIGN OF DAPPED STEEL PLATE GIRDERS	February 2005
	6. Performing Organization Code

7. Author(s)	8. Performing Organization Report No.
Gary T. Fry, Breanna M. Bailey, Justin L. Farr, Jeffery E. Elliott, and Peter B. Keating	Report 0-2102-1

9. Performing Organization Name and Address	10. Work Unit No. (TRAIS)
Texas Transportation Institute The Texas A&M University System College Station, Texas 77843-3135	11. Contract or Grant No. Project 0-2102

12. Sponsoring Agency Name and Address	13. Type of Report and Period Covered
Texas Department of Transportation Research and Technology Implementation Office P. O. Box 5080 Austin, Texas 78763-5080	Technical Report: September 1999 – August 2002
	14. Sponsoring Agency Code

15. Supplementary Notes

Project performed in cooperation with the Texas Department of Transportation and the Federal Highway Administration.
Project Title: Study of Dapped Girder Ends on Steel Structures
URL: http://tti.tamu.edu/documents/0-2102-1.pdf

16. Abstract

The objective of this project is to provide a technical basis for the standardized design of dapped girder ends on steel highway bridges. The dapped end girder details investigated in this project, both as test specimens and analytical models, were based upon designs that are in service in the state of Texas. Analytical and full-scale experimental investigations were performed to provide information about the fatigue behavior and the ultimate strength behavior of the dapped girder ends considered in the study. Several engineering recommendations are forwarded based upon the results of the investigations.

17. Key Words	18. Distribution Statement
Steel Bridge Design, Steel Plate Girders, Dapped Details, Full-Scale Testing, Post-Buckling Strength, Fatigue Strength, Finite Element Analysis, Traffic Live Load Simulation	No restrictions. This document is available to the public through NTIS: National Technical Information Service Springfield, Virginia 22161 http://www.ntis.gov

19. Security Classif.(of this report)	20. Security Classif.(of this page)	21. No. of Pages	22. Price
Unclassified	Unclassified	174	

Form DOT F 1700.7 (8-72) Reproduction of completed page authorized

BEHAVIOR AND DESIGN OF DAPPED STEEL PLATE GIRDERS

by

Gary T. Fry, Ph.D., P.E.
E. B. Snead Associate Professor I
Department of Civil Engineering, Texas A&M University

Breanna M. Bailey
Graduate Research Assistant
Department of Civil Engineering, Texas A&M University

Justin L. Farr
Graduate Research Assistant
Department of Civil Engineering, Texas A&M University

Jeffery E. Elliott
Graduate Research Assistant
Department of Civil Engineering, Texas A&M University

and

Peter B. Keating, Ph.D.
Associate Professor
Department of Civil Engineering, Texas A&M University

Report 0-2102-1
Project 0-2102
Project Title: Study of Dapped Girder Ends on Steel Structures

Performed in cooperation with the
Texas Department of Transportation
and the
Federal Highway Administration

February 2005

TEXAS TRANSPORTATION INSTITUTE
The Texas A&M University System
College Station, Texas 77843-3135

DISCLAIMER

The contents of this report reflect the views of the authors, who are responsible for the facts and the accuracy of the data presented herein. The contents do not necessarily reflect the official view or policies of the Federal Highway Administration (FHWA) or the Texas Department of Transportation (TxDOT). This report does not constitute a standard, specification, or regulation. The engineer in charge was Dr. Gary T. Fry, P.E. (TX #94066).

ACKNOWLEDGMENTS

This project was conducted in cooperation with TxDOT and FHWA. The investigators gratefully acknowledge the professional contributions of several individuals from TxDOT whose names are listed below. Each of these people not only provided essential guidance for the project but also conveyed an earnest willingness in offering their support that was very much appreciated by the investigators. We extend especial thanks to the project coordinator, Mr. Tom Yarbrough. We wish to recognize the project directors, Mr. Alan Crozier and Mr. Michael Flaming, as well as the other members of the Project Monitoring Committee: Mr. John Holt and Mr. Mark Steves. Additionally, Mr. David Hohmann and Mr. Richard Wilkison are thanked for providing valuable insight and support. We wish to recognize two TxDOT engineers who provided special assistance, guidance, and insight for a large number of important issues over the course of this project: Mr. Kenneth Ozuna and Mr. John Vogel. A critical task of this project was selection of a study bridge and specific dapped girder end details that would form the basis for the investigation. We gratefully acknowledge the following individuals who participated in the case-study selection process: Mr. Joseph Banki, Pan, Banki & Associates; Mr. Kenneth Ozuna, TxDOT, Houston; Mr. Jerry Pan, Pan, Banki & Associates; and Mr. Edwin Suchicki, Brown & Root.

Test specimens used in this study were fabricated by Trinity Industries of Houston, Texas. Laboratory fixtures were fabricated by Central Texas Iron Works of Waco, Texas. The investigators thank Mr. Donald Krenek of Trinity Industries and Mr. Roy Eaton and Mr. David Harwell of Central Texas Iron Works for their support. The staff of the Texas Engineering Experiment Station High-Bay Structural Testing Laboratory is thanked for their assistance in performing the experiments. Dr. Laurence Rilett, professor, Department of Civil Engineering, University of Nebraska-Lincoln, is thanked for providing the traffic flow simulation data used in this study.

The study of dapped girders in Japan was made possible by the generous assistance of several individuals. The project supervisor happily acknowledges a special debt of gratitude to his colleagues in Japan: Dr. Chitoshi Miki, dean, Graduate School of Science and Engineering, Tokyo Institute of Technology; Dr. Takuyo Konishi, project manager, and Mr. Atsushi Shibuya, project engineer, both of the Tokyo Metropolitan Expressway Retrofit Project; and Dr. Eiichi

Sasaki, assistant professor, and Mr. Hisatada Suganuma, doctoral candidate, both of the Department of Civil Engineering, Tokyo Institute of Technology.

TABLE OF CONTENTS

Page

LIST OF FIGURES

LIST OF TABLES

Page

CHAPTER 1:
INTRODUCTION

PROJECT OBJECTIVE

The objective of this project is to provide a technical basis for the standardized design of dapped girder ends on steel highway bridges.

BACKGROUND

Bridges in the state of Texas often comprise long steel girder spans immediately adjacent to shorter prestressed concrete girder spans. In such cases, there is usually a mismatch in member depth where the steel and concrete girders meet end-to-end over a common bent. This geometric problem is commonly resolved in one of two ways. A step is sometimes placed in the bent cap to accept the shallow concrete girder on one side and the deep steel girder on the other (Figure 1a). Alternatively, the deep steel girder can be made shallower at its terminal end, or dapped, to rest at the proper elevation on a flat bent cap end-to-end with the concrete girder (Figure 1b). The dapped alternative (Figure 1b) is the subject of this project. Note that there can be other design situations that call for the use of dapped steel girders in bridge construction projects. For example, architectural program requirements might stipulate the use of a dapped girder end detail.

Figure 1. (a) Stepped Bent Cap. (b) Dapped Girder.

Three different dapped details, ones commonly employed in Texas, are considered in this study as indicated schematically in Figure 2: a notched detail, a 90-degree rounded detail, and a tapered detail. At the present time, design standards for dapped details do not exist. Consequently, engineers have employed many variations of dapped details based on the three

common geometries shown in Figure 2. Some of the variations involve complicated arrangements of stiffener plates and welds and associated high fabrication costs. There are also cases where dapped details have developed severe problems with fatigue cracking. Engineers, therefore, need a design standard to guide them away from unnecessarily expensive details and to ensure performance reliability in terms of ultimate strength and fatigue resistance.

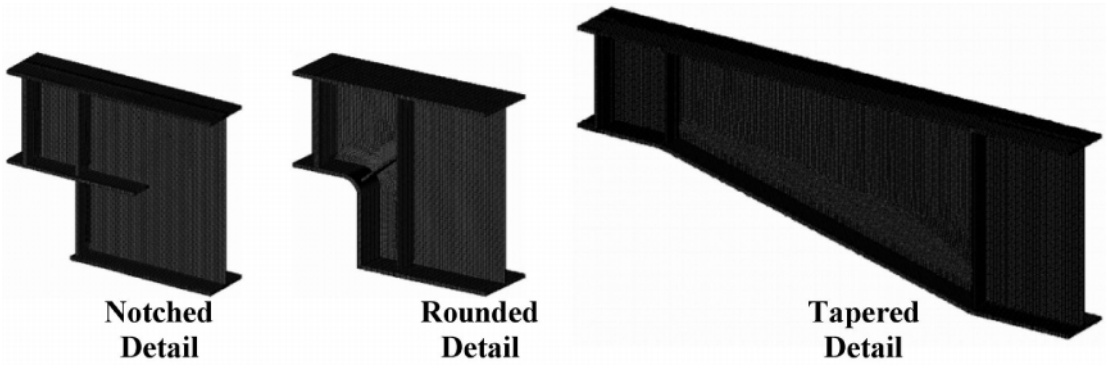

Figure 2. Case-Study Dapped Girder End Details.

OVERVIEW OF RESEARCH TASKS

The aim of this report is to provide enough technical information to support a set of design standards for dapped girder ends on steel highway bridges. In this project, analytical and experimental investigations were performed. These investigations were designed to provide information about the fatigue behavior of dapped girder ends and to provide information about the ultimate strength behavior of dapped girder ends.

Selection of Case-Study Bridge and Dapped Girder End Details

The dapped end girder details investigated in this project, both as test specimens and analytical models, were based upon actual designs that are in service in the state of Texas. At the end of a meeting with private consulting engineers and a representative of the TxDOT Houston District, it was agreed that the TxDOT office in Houston would provide detailed drawings of a bridge that would be used as a "case study" in the project. The case-study bridge is located in Montgomery County on IH-45 (District No. 12, Control No. 0110, and Section No. 04). For the

purposes of this project, researchers considered the bridge to be representative of bridges employing dapped details. In addition, drawings were provided by the Houston TxDOT office for a representative notched detail and a representative rounded detail as depicted in Figure 2. The case-study bridge itself incorporated a tapered detail. Each of the three details was studied in turn as though it constituted the dapped girder ends of this bridge.

Investigation of Fatigue Behavior

Summary of Dapped Detail Fatigue Cracks in Japan

In Japan a dapped girder is usually referred to as a "cut-off" girder. Since the early 1960s, dapped steel girders have been used widely in Japan, the most common application being the 90-degree rounded detail. Since the mid-1970s, hundreds of instances of fatigue cracking have been reported in Japan involving this detail. Generally, the cracks initiate at either the root or the toe of a fillet weld where the weld joins the web plate to the curved portion of the flange plate. Subsequently, the cracks propagate within the web vertically and also within the web around the bent flange. The flange plate itself remains completely undamaged.

Analytical Tasks

Because the dapped region of the girders is subjected to a variable-amplitude, multi-axial stress history, a special effort was required to investigate the fatigue behavior of the dapped details analytically under service load conditions. Three-dimensional finite-element models were assembled for the entire case-study bridge. In these "global" models of the bridge superstructure, shell elements modeled the girders and composite concrete deck and multi-point constraints linked the deck to the girders to simulate composite behavior. Solid elements modeled the bearing pads. In addition to the global models, local refined submodels of the dapped regions were constructed using solid elements. These submodels were "driven" at their edges by the displacement results from the global models after they were subjected to simulated traffic loading. The specific wheel loads used in the simulation were determined based on a stochastic procedure calibrated against weigh-in-motion (WIM) data provided by TxDOT. The WIM data were coupled with an advanced traffic flow simulation program called CORSIM. With input from the three-dimensional stress histories of the solid submodels, a multi-axial, critical-plane

fatigue parameter called Findley's parameter was used to quantify the fatigue demand experienced at critical locations within each of the three dapped details considered in this study. Researchers used the results of these procedures to establish and compare the fatigue strength among the three details.

Experimental Tasks

Because of the proximity of the dapped detail to the girder support, the reaction force at the support primarily determines the state of stress at critical locations within the dapped region, the assumption being that critical stresses in the dapped region are proportional to the support reaction. In such a case, accurate fatigue tests of the details are straightforward to accomplish. For each detail (i.e., notched, rounded, and tapered) a 281-in. long, full-scale, I-shaped, bare-steel specimen was fabricated according to the original drawings provided by TxDOT. The dapped end of each specimen rested on a bearing pad, and the other end of the specimen was simply supported. Two actuators were used to load the specimen. The actuator controllers were programmed to create a desired support reaction history as the input fatigue load for the specimen. Reaction histories from the analytical models described above for the fatigue analysis were used to determine the load histories for the fatigue experiments.

Investigation of Ultimate Strength Behavior

Analytical Tasks

The ultimate strength behavior of dapped girder ends was examined analytically using a series of three-dimensional finite-element models. The models accommodated material and geometric nonlinearity to allow analytical assessment of girder behavior under ultimate load conditions. For each specimen considered, the modeling technique involved three steps. First, a three-dimensional model of the bare-steel specimen was constructed using shell elements. Second, a linear eigenvalue analysis of the model was completed. Third, researchers used the results from the eigenvalue analysis to construct a fully geometric and material nonlinear analysis of the specimen from which they could determine the ultimate strength of the specimen. Based upon the results from the initial set of analytical models, three specimens for laboratory testing were designed. These test specimens were modeled analytically in a similar fashion for comparison of the analytical predictions with experimental results.

Experimental Tasks

Three full-scale, bare-steel, I-shaped dapped girder end specimens were fabricated and tested. The specimens were roughly 62 in. deep at full section, 31 in. deep at dap section, and incorporated 0.25-in. thick web plates and 1.25-in. by 18-in. flange plates. Each specimen was tested as a cantilever beam over a 288-in. span with load applied at its tip (dapped end). The maximum height-to-thickness ratio for the web plate was 240. Two specimens incorporated a 4:1 tapered detail. One of these included intermediate welded transverse stiffeners at each of the two bends in the flange plate in addition to bearing stiffeners at support locations. The other tapered specimen used bearing stiffeners at support locations only; no other stiffeners were present in the test panel. The third specimen incorporated a 90-degree rounded detail. Similar to the second tapered specimen, the rounded specimen used bearing stiffeners at support locations only; no other stiffeners were present in the test panel. The goal of the tests was to examine nominal shear force resistance and specifically the post-buckling behavior of the test panels.

CHAPTER 2:
ANALYSIS OF CASE-STUDY BRIDGE

CHAPTER OVERVIEW

To generate data for comparing the performance among the three dapped details selected for this project, and also for examining the performance of possible improved details, a special analysis of the case-study bridge was performed. In this study, detailed three-dimensional, hierarchical finite element analyses are coupled with an advanced traffic simulation program and weigh-in-motion traffic surveys to determine local stress histories in critical regions of the dapped girders under simulated service live-load conditions. This procedure for bridge simulation was invented for this project, and a summary is provided in this chapter. The details of the procedure are reported in the master's thesis of a coauthor of this report (*1*).

DESCRIPTION OF CASE-STUDY BRIDGE

The TxDOT office in Houston provided detailed drawings of a bridge in Montgomery County on IH-45 (District No. 12, Control No. 0110, and Section No. 04). This bridge includes five three-span, continuous steel girders with dapped end details. The spans are 125 ft long at either end of the bridge, and the midspan is 155 ft long. The girders are spaced on approximately 9-ft centers. The steel used in the girders is type A709-50W. The bridge deck is 42 ft, 10 in. wide, 8 in. thick, and carries three lanes of one-directional northbound traffic. The existing bridge in Montgomery County employed the tapered dapped girder end detail shown in Figure 2.

GLOBAL FINITE-ELEMENT MODELS

A schematic drawing of a portion of the global finite-element model for the case-study bridge is provided in Figure 3. The particular model shown incorporates the tapered detail. Other models of this bridge incorporate the notched detail and the 90-degree round detail. Figure 4 shows a special view of the notched girder global model in which only the girders are visible. Composite action from the concrete deck of the bridge is included in the models directly, as well as contact and potential separation behavior at support locations. It was determined that the diaphragms had little impact on the loads in the regions of interest. To simplify the analyses they were excluded from the model. The geometrical effects of camber were also included in this

simulation. Standard properties of steel and concrete, such as unit weight, Poisson's ratio, and modulus of elasticity, were used in the analyses.

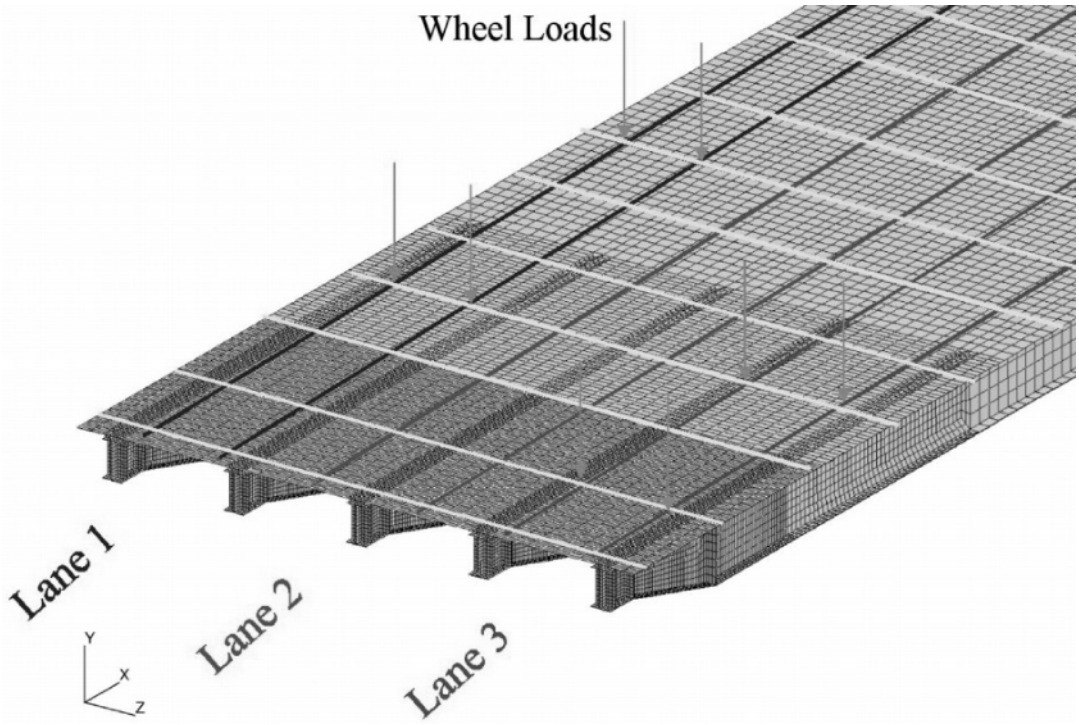

Figure 3. Global Finite-Element Model of Case-Study Bridge.

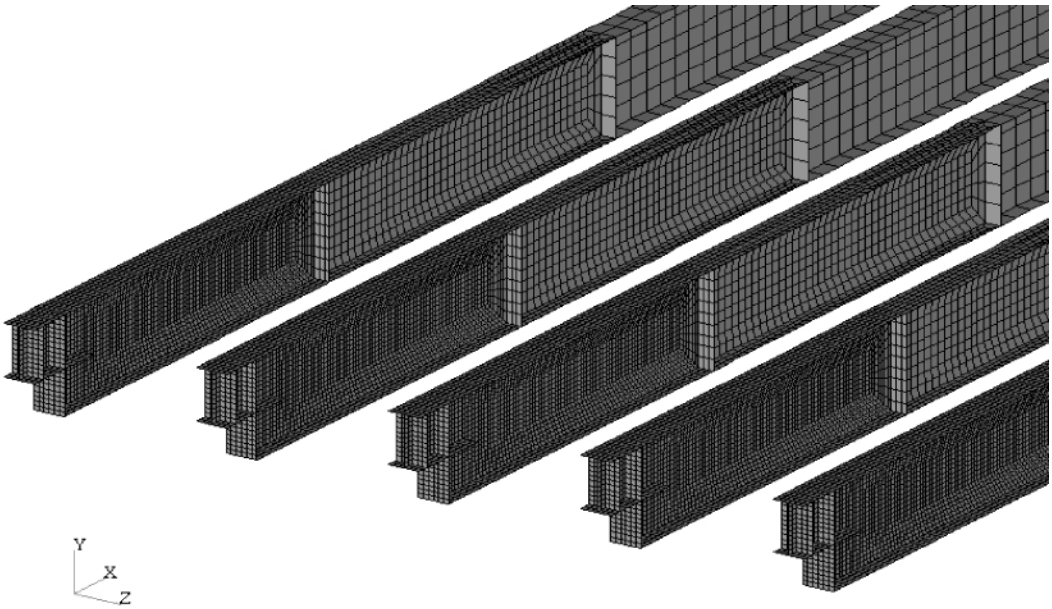

Figure 4. Global Model for the Notched Girder Detail.

In the global models, shell elements modeled the girders and concrete deck, while solid elements modeled the bearing pads. Since the main area of interest in the global model is the dapped region, more elements were used near these support locations. Shell elements in the dapped region had a characteristic edge length of 76 mm (3 in.), while shell elements that were remote from the supports had a characteristic edge length of 305 mm (12 in.). Solid elements used in the bearing pads had a characteristic edge length of 25 mm (1 in.). This element refinement provided an acceptable approximation in the areas where more accurate results were required. The global model contained on the order of 150,000 elements and 160,000 nodes. The models were generated using Patran (version 8.5) and solved using ABAQUS (version 5.8) software (*2*, *3*).

While creating the global model, researchers paid special attention to the interface between the top flanges of the girders and the concrete deck. Both the top flanges of the steel girders and the concrete bridge deck were modeled using two-dimensional shell elements. All shells were placed at the midthickness of the object they represented. This geometry created a gap between the top flanges of the girders and the concrete deck so that there was no direct nodal connectivity between the deck and top flange elements. Multiple point constraints (MPCs) established connectivity between these elements.

Tied MPCs constrain two nodes at different points in space to have the same value for all components of displacement and rotation (3). About 4 in., or one-half of the deck thickness, separated the layer of shells comprising the top flanges and the layer of shells comprising the concrete deck. The tied MPCs established connectivity between the nodes at the midthickness of the concrete deck and nodes at the midthickness of the top flange (see Figure 5). The tied MPCs ensured that the displacement of the nodes in the top flanges below the concrete deck were equal to the displacements in the concrete deck.

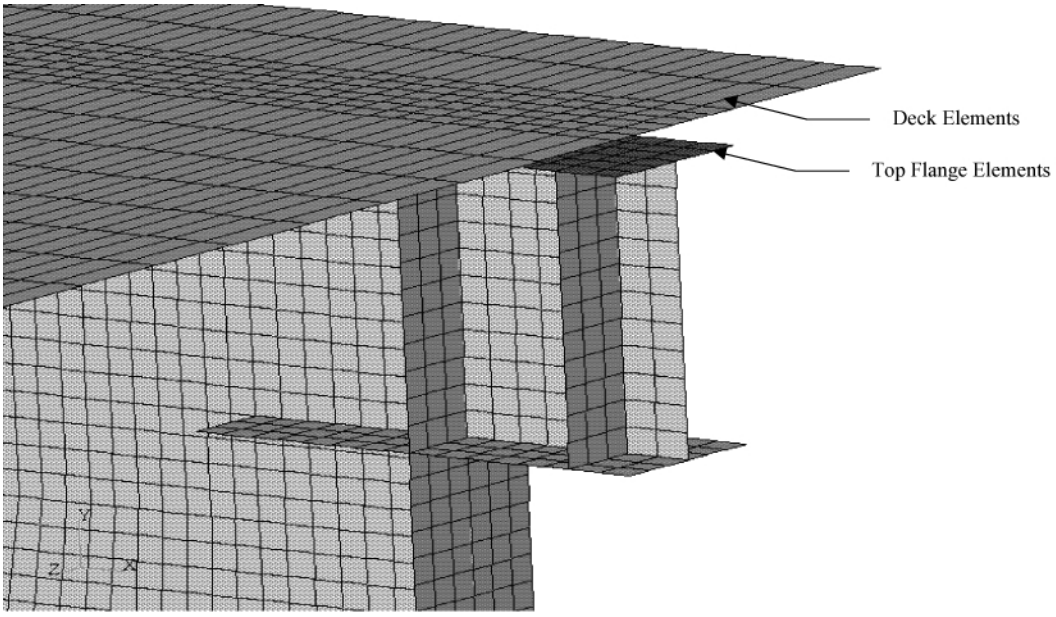

Figure 5. Closeup View of Deck and Girder Elements in Global Model.

By constraining the displacements of the top flanges to be equal to the displacements of the concrete deck, the tied MPCs represent full composite connection between the deck and girder. A pinned MPC defined the connection between the bottom of the flange and the top of the bearing pad (see Figure 6). The solid elements used to model the bearing pads were assigned the properties of an elastomeric bearing material. The element mesh was selected for the solid bearing pad elements to provide a suitable approximation of the support behavior. This element refinement, deemed necessary, caused a size difference between the shell elements on the bottom flange and the solid elements in the bearing pad. In order to impose the deflection of the bottom flange onto the bearing pad, a pinned MPC was created between every node on the top of the

bearing pad and the nearest node on the bottom flange. A pinned MPC causes the displacements of two nodes to be equal but leaves rotation independent (3).

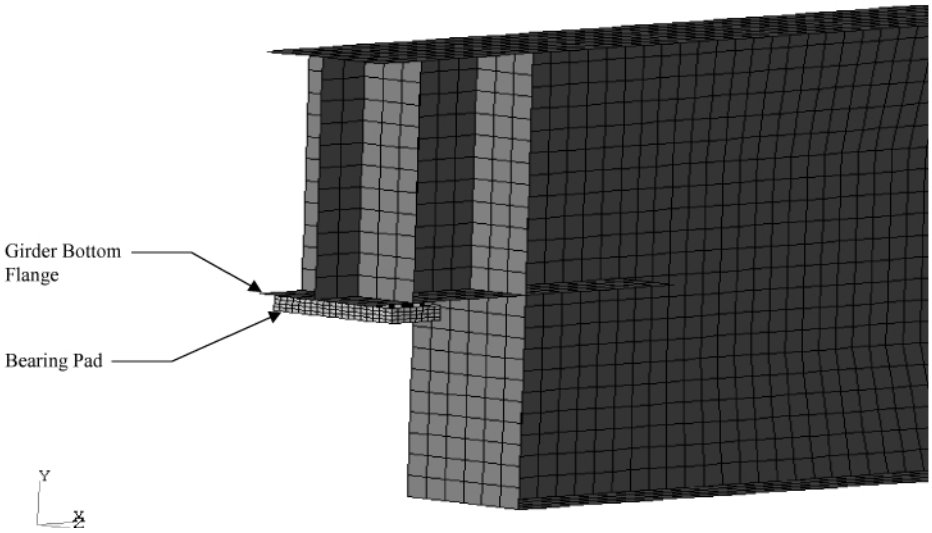

Figure 6. Closeup View of Bearing Pad in Global Model.

Every pinned MPC in the global model required that a command line be added to the ABAQUS input file containing the node identification numbers of the two nodes belonging to the MPC. To simplify this process, a computer program was written to generate the necessary command lines. The MPC writer Fortran program uses the spatial coordinates in the ABAQUS input file to calculate the shortest distance between a node on the bottom flange and the top of the bearing pad. The program then writes the necessary command lines for the ABAQUS input file in the correct order and with the correct node identification numbers. Refer to Figure 7 for a flowchart.

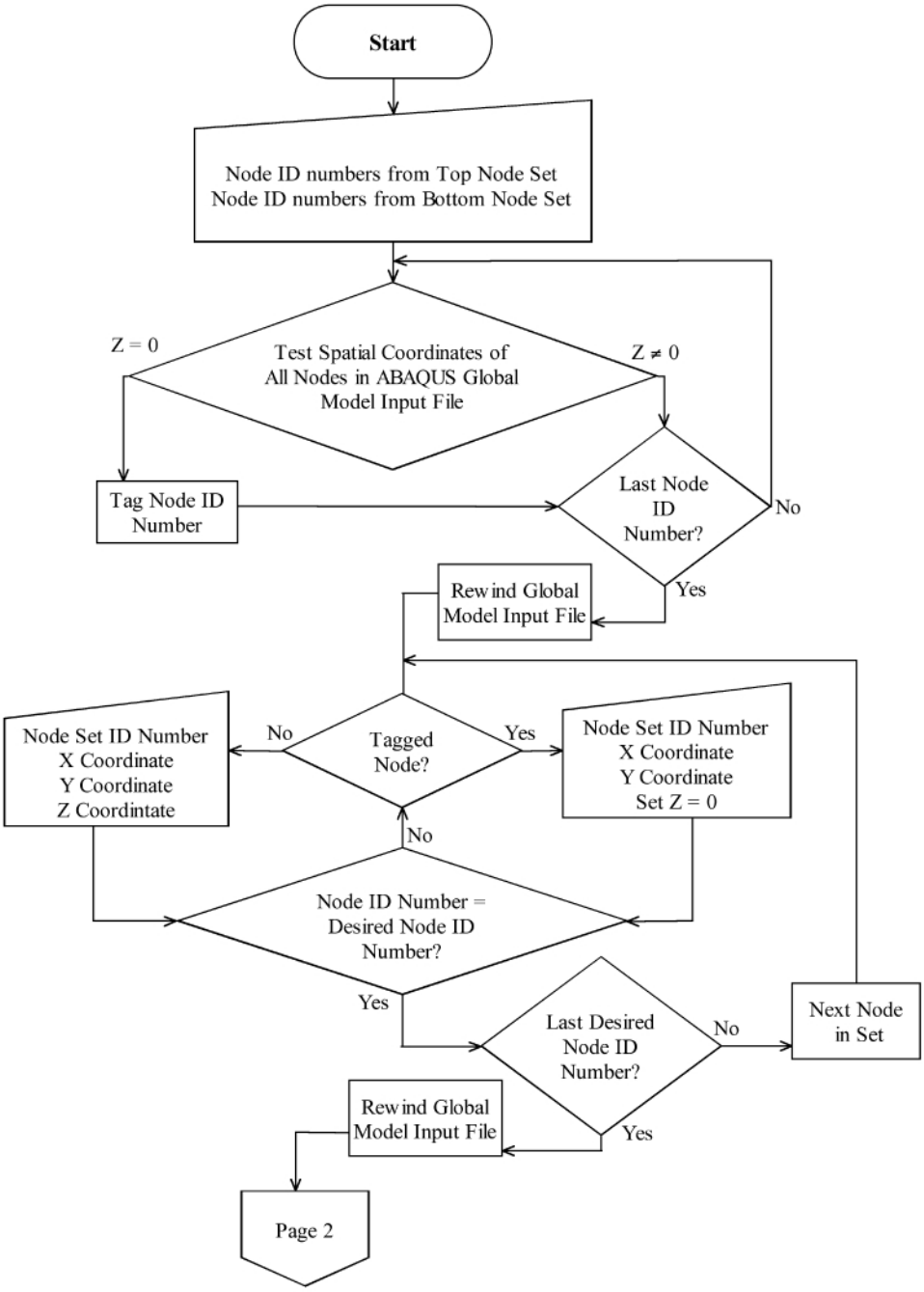

Figure 7. Flowchart for the MPC Writer Program.

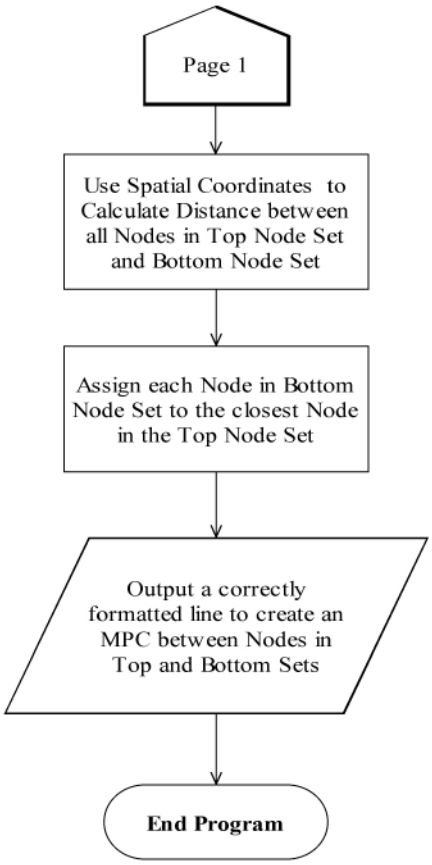

Figure 7. Flowchart for the MPC Writer Program (continued).

LOCAL FINITE-ELEMENT MODELS

Researchers used submodeling to create a refined analysis for the dapped region. In submodeling, a separate finite-element model that includes only the local area of interest is created using the same coordinate system used in the global model. This local model has a far more refined mesh than the region it represents in the global model and includes more precise geometric details than can be included in the global model. The local model used for the rounded dap detail is shown in Figure 8. To "load" a local submodel, displacements from the global model are imposed on all of the "cut edges" of the submodel (i.e., where it would connect to the global model if it were part of the global model).

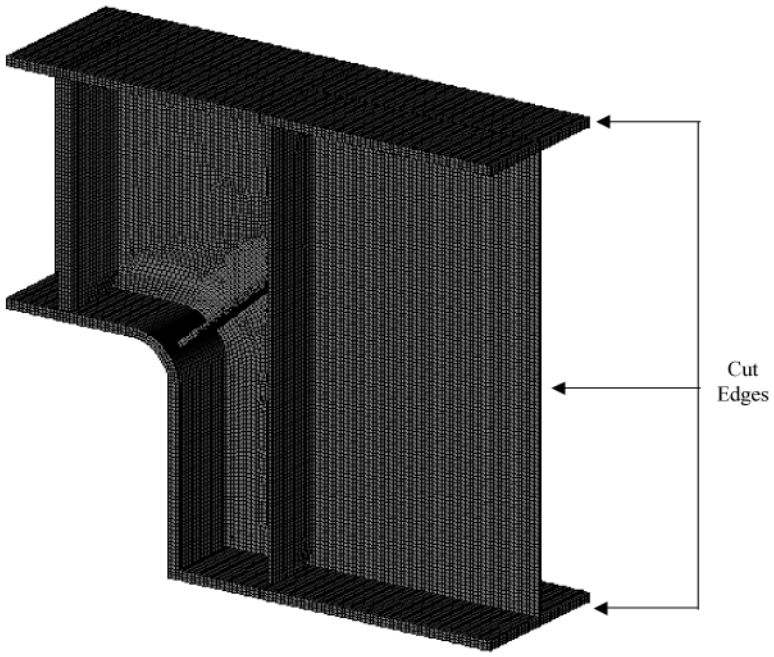

Figure 8. Local Model for the 90-Degree Rounded Detail.

The local models included the dapped region of the girders, the bearing pad, and a sufficient extension into the span to include any unusual stress distributions that result from the dapped end. Local models were built of solid, rather than shell, elements. Solid elements account for through thickness shear stresses not considered in the formulation of shell elements. Models for the notched and round dap region had approximately 80,000 elements and 110,000 nodes, while the tapered local model required 170,000 elements and 250,000 nodes. The tapered model had more elements because the dapped region covered a larger area than the notched and rounded details; therefore, a longer portion of the girder needed to be modeled to accommodate the full length of the slope.

The web was modeled with two elements through the thickness, the flange used three elements through the thickness, and the number of elements through the thickness of the stiffeners varied from two to four. The local model also accounted for many of the geometric details that had to be omitted from the global model. Stiffeners were no longer extended to the edge of the flange but were dimensioned according to the TxDOT drawings. The stiffener weld clips near the web to flange interface were also included in the local model.

The stresses caused by the bearing support had a significant effect on the stresses in the dapped region of the girder. Contact elements accurately modeled the behavior of the bearing support. Four parameters in ABAQUS had to be properly defined in order to model the contact interaction between the bottom flange of the girder and the bearing pad: the master-slave relationship, the adjustment tolerance, the normal interaction, and the sliding behavior of the interface. The material properties of the bearing pad were taken as typical for a rubber bearing type elastomeric material. The support condition at the base of the pad was taken as fixed.

Contact pairs in ABAQUS follow a strict master-slave relationship. The contact interface consists of two surfaces, a master and a slave surface. The nodes of the elements that are in contact form these surfaces. For each node on the slave surface, ABAQUS finds the nearest node on the master surface by determining where the normal to the master surface intersects the slave surface. The interaction is then discretized between the point on the master surface and the nearest node on the slave surface (*3*).

The nodes of the bottom flange of the dapped girder directly above the bearing pad were modeled as the master surface, as shown in Figure 9. Additionally, a small region of the bottom flange that was near, but not directly above, the bearing pad was included in the master surface to allow the girder to move and still remain in contact with the bearing pad. The top surface of the bearing pad was modeled as the slave surface. The master surface nodes were approximately 0.1 in. above the nodes comprising the bearing pad.

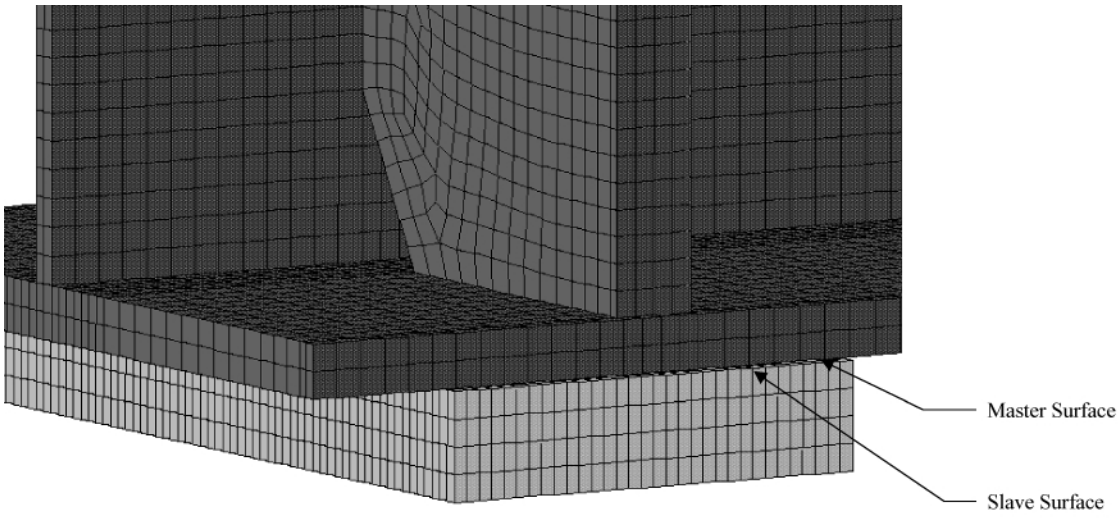

Figure 9. Bearing Detail in Local Model.

During model creation, the master and slave surfaces cannot be defined with the same spatial coordinates because of numerical problems. Even though the two surfaces will end up in "contact," they must originally be created with a small separation. This separation is eliminated by moving the master and slave surfaces into contact before analyzing the local model. The "adjust" tolerance, the maximum distance through which nodes may be moved, defines which nodes to move into contact. The tolerance was typically on the order of, but slightly greater than, 0.1 in. For the local model, ABAQUS moved the nodes comprising the bearing pad up a small distance until they were in contact with the bottom flange.

ABAQUS also required a normal interaction definition between the master and slave surfaces; normal interaction describes the way stress is transferred normal to the contact surfaces. This analysis used the interaction model described as hard contact in the ABAQUS manual (3). Hard contact allows any amount of pressure to be applied while the surfaces are in contact, but the pressure reduces to zero as the surfaces separate. Figure 10 graphically illustrates this concept. Hard contact ensured that the bearing would not transfer tensile forces between the bearing pad and the girder. The girder was free to lift off or separate from the bearing pad.

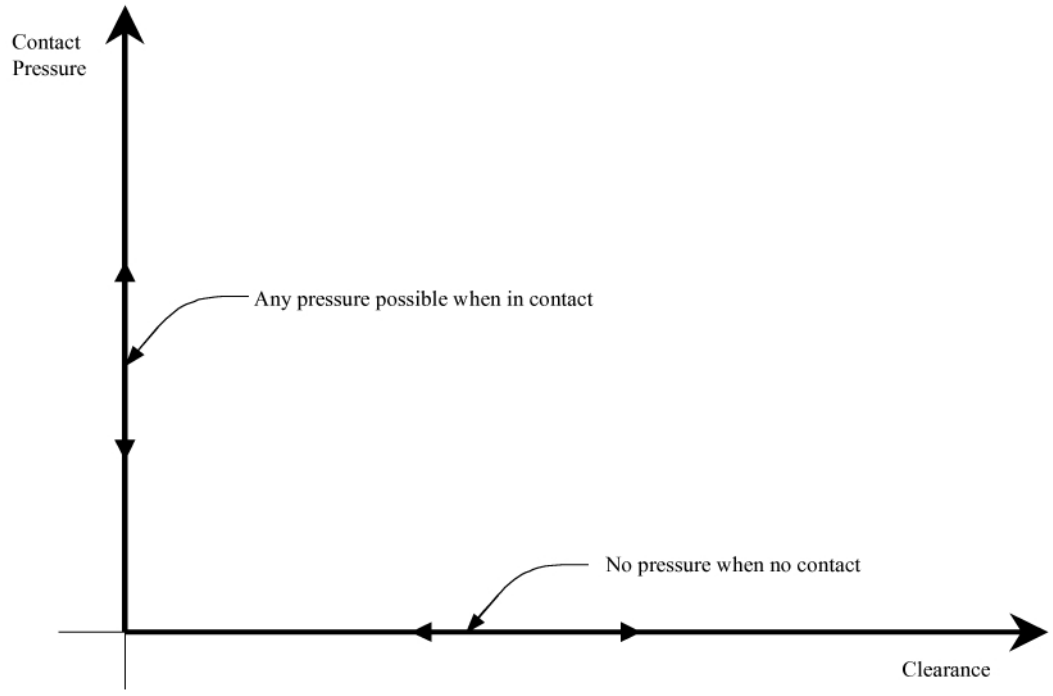

Figure 10. Description of Hard Contact Model for Bearing Surface Interface.

A nonlinear finite element analysis allowed the use of the finite sliding algorithm to model the behavior of the contact interaction. In ABAQUS, finite sliding allows for arbitrary separation, sliding, and rotation between two surfaces. As the surfaces slide by each other, the nodes on the slave surface are tracked by ABAQUS. Tracking is the process by which the slave nodes are assigned a new master node after each solution iteration. Updating the master-slave relationship gives the model the freedom to slide as needed and still remain in contact. Finite sliding is the most general sliding allowed in ABAQUS. This finite sliding parameter modeled the contact interaction as frictionless. The frictionless behavior allows the two surfaces to slide freely by one another with no resistance. Researchers made the assumption that neglecting friction would not significantly affect the stresses in the bearing region.

The bearing pad dimensions were changed slightly to avoid a numerical problem known as chattering. Chattering is a numerical instability associated with contact interaction in which a slave surface node becomes trapped behind the master surface. When this problem occurs, a node on the slave surface is not always in contact with the master surface. When a node begins to behave in this way, the numerical solution to the model will not converge. Chattering often occurs when the slave surface nodes are near the perimeter of the master surface. Trimming the bearing pad by 0.25 in. eliminated this problem.

The purpose of carefully modeling the bearing region was to ensure that the stresses in the local model were accurate. The bearing region is important because of its close proximity to the dapped region. Aspects of the bearing region model were the selection of an elastomeric material (as in the global model) and the creation of a contact region between the bearing pad and bottom of the girder.

SIMULATION OF TRAFFIC FLOW

CORridor SIMulation (CORSIM) is a high-fidelity, medium-scale traffic simulation package employed to define a flow of traffic crossing the case-study bridge in this project. The highway micro-simulation module of CORSIM is based on the FRESIM model, which is in turn derived from the INTRAS model developed in the late 1970s (*4*, *5*). CORSIM may be categorized as fine resolution because it models each vehicle and driver in a discrete manner and medium scale because it models primarily freeway and arterial networks but not local streets (*6*). More importantly, it can be classified as high fidelity because it attempts to represent the spatial

interaction of drivers on a continuous, rather than a discrete, basis and because it attempts to model the car-following logic of the drivers in detail.

Because the overall goal is to mimic both the small-scale and large-scale dynamics of traffic, the modeler has control over a large number of parameters including grade, percentage of nine distinct vehicle types, driver aggressiveness, free-flow speed, acceleration and deceleration capabilities, etc. CORSIM can be calibrated for any stretch of highway for which sufficient traffic data exist. Researchers adopted CORSIM in this project because it is used extensively for operational analyses and is a state-of-the-practice traffic micro-simulation tool (*7*). The results of the traffic simulation model include vehicle identification number, vehicle type, vehicle position, lane identification, time of record, velocity, and acceleration. The vehicle identification number is an identifier for a vehicle at any time. The vehicle type is a number that represents a specific type of predefined vehicle. Vehicle position is the distance from the vehicle to a datum point. Lane identification indicates which lane the vehicle is traveling in at any given time. From this information, traffic types and positions can be tracked, for example, as they move across a bridge.

For the present study, CORSIM was calibrated on a 22.4 km (36-mi.) section of the main lanes of Interstate 10 in Houston, Texas. Volume data were collected using pneumatic tubes in May and June of 1996. The I-10 corridor is monitored as part of the Houston TRANSTAR advanced traffic management system and has five automatic vehicle identification (AVI) readers, which correspond to four AVI links, along its length. The AVI data were used to calculate the average space mean travel time for each AVI link by time of day during the time period when volume data were collected. One of the fundamental requirements of highway micro-simulation models is an origin-destination (O-D) matrix that represents the system demand. Because collecting O-D information is extremely expensive, synthetic techniques are typically used. In this project, the O-D was estimated using observed AVI data (*8*). An analysis of the travel time data was performed, and three time periods were identified: the AM peak period (7:00 A.M. to 8:00 A.M.), the PM peak period (5:00 P.M. to 6:00 P.M.), and the off-peak period (2:00 P.M. to 3:00 P.M.).

Calibration of the CORSIM model was challenging because the default values gave very poor results. The car-following headway, referred to as the sensitivity factor in CORSIM, was adjusted from the default setting of (15, 14, 13, 12, 11, 10, 9, 8, 7, 6) for driver types 1 through

10, respectively, to (4, 4, 4, 4, 3, 3, 3, 3, 3, 2, 1). The gap acceptance parameter was changed from the default value of 3 to 6 in order to make the drivers more aggressive. Researchers found that these factors significantly affected the results to the point of creating large bottlenecks where none were observed to exist in the field. Other authors report similar findings regarding the calibration of the car-following headway (*9*, *10*). The mean absolute error ratio (MAER) for the AM peak, off-peak, and PM peak analyses were 0.20, 0.08, and 0.03, respectively.

WEIGH-IN-MOTION SYSTEMS

Weigh-in-motion is a process of measuring the dynamic tire forces of a moving vehicle and estimating the corresponding tire loads for a static vehicle (*11*). The use of WIM systems is governed by the American Society for Testing and Materials (ASTM) specification E 1318-94. There are various types of WIM systems in use; however, piezoelectric systems are the most economical and most common system used.

Typically, the entire system is embedded in the roadway during construction and calibrated before regular traffic begins. In addition to wheel loads, WIM systems can also measure and store the following data parameters: gross vehicle weights, vehicle speed, lane of operation, date and time of passage, number and spacing of axles, and vehicle classification (according to axle arrangement). WIM systems can typically identify up to 14 different vehicle classifications. The accuracy of WIM systems is such that 95 percent of vehicles register within ±10 percent of their static weight.

TxDOT maintains several locations throughout the state (see Figure 11) where WIM data are collected (*12*). Information collected at these sites includes vehicle class, gross vehicle weight, wheel loads, total vehicle length, and inter-axle spacing. WIM data used in this simulation were obtained from site 512 on I-37, Live Oak County, between San Antonio and Corpus Christi, Texas, between January and August of 1999.

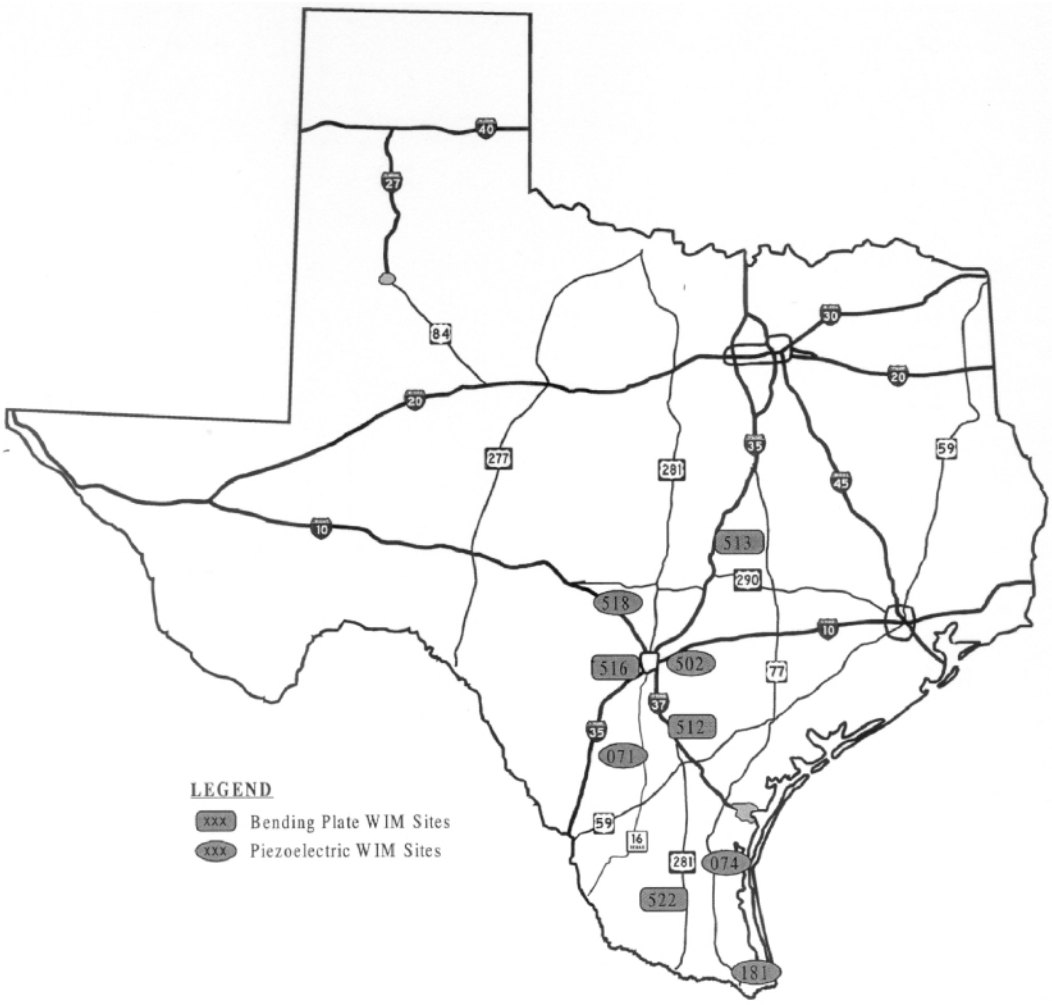

Figure 11. WIM Locations in the State of Texas.

PROCEDURES FOR ANALYSIS OF CASE-STUDY BRIDGE

Generation of Simulated Live Load History

In order to make an accurate assessment of component fatigue strength, both the component and its service environment must be modeled as realistically as possible. Capturing this behavior is a major goal of this project. Therefore, careful attention was paid to the manner in which traffic live loading was defined. Two sources of data were combined to create a traffic live load environment for the case-study bridge: traffic flow data sets created by the CORSIM traffic simulation package and actual WIM traffic survey data sets provided by TxDOT. The specific wheel loads used in this simulation were determined based on a stochastic procedure calibrated against the WIM data.

CORSIM may model only a limited number of vehicle types. Therefore, researchers grouped the various cars and trucks that comprise the FHWA and TxDOT classification systems into broader categories. Of the 14 predefined vehicle types and 34 subtypes in the WIM data set, the 9 most significant vehicle types had to be chosen. Subtypes were identified to distinguish among vehicles of the same type with different numbers of axles. The nine most significant subtypes represented those vehicles that were heavy enough and/or frequent enough to pose fatigue problems. This provided a combination of very heavy vehicles, which occur rarely, and lighter vehicles, which occur more often. Selection of these nine types neglected only 9 percent of the total WIM data.

WIM data are used to ascribe gross weight to a vehicle in the simulation, while axle length and wheel loads dictate load placement. Of course, not all vehicles within a class have the same characteristics, and it is important to capture this diversity in the simulation. Therefore, the records gathered at the WIM site were combined to form a database of possible wheel load configurations for each vehicle class. In order to create this database, the WIM data were separated into tables according to CORSIM class. Data in the table were sorted in ascending order by gross vehicle weight, and each record was assigned a percentile value using Equation 1.

$$p = \frac{i}{n+1}. \qquad \text{(Equation 1)}$$

A cumulative distribution function (CDF) was defined at discrete points for all nine CORSIM vehicle types. These CDFs can be used to assign pseudo-random weights to each vehicle that crosses the bridge.

Figure 12 illustrates schematically how the simulation assigns a pseudo-random weight to a vehicle. The main Fortran program (to be described later) generates a random number between 0 and 1. This number represents a percentile rank for the vehicle being assigned a weight. Using the appropriate CDF for the vehicle type of interest, the program then selects a gross vehicle weight by interpolating between discrete points on the CDF closest to the pseudo-random percentile rank. Once a gross vehicle weight is determined, a set of corresponding wheel loads is pseudo-randomly chosen from the set of all vehicles of the same type with an identical gross

vehicle weight. Thus, representative wheel loads and spacing are selected from the tables of WIM data according to the frequency of their occurrence in the class population.

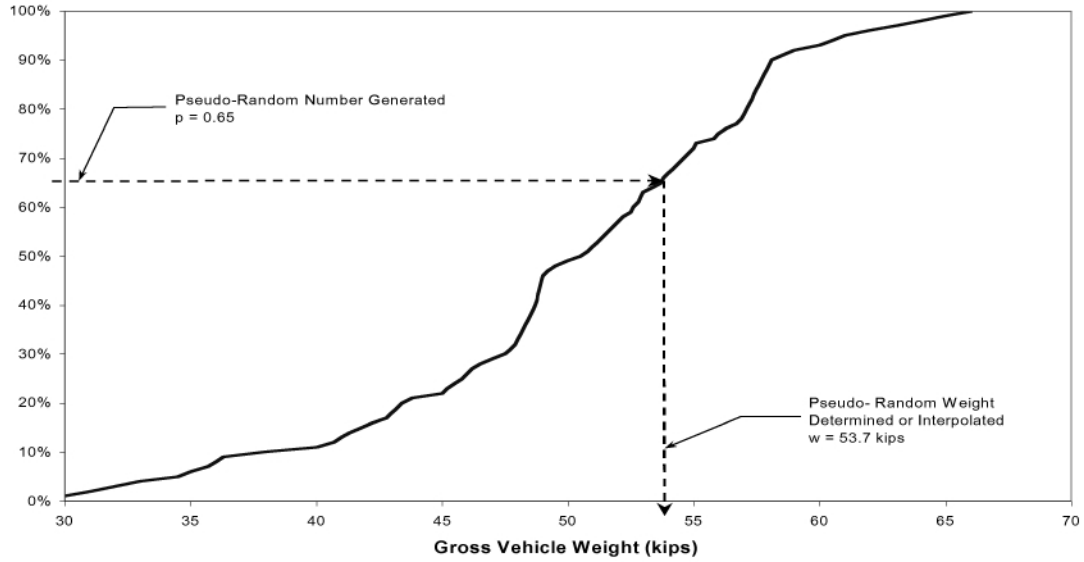

Figure 12. Assignment of Weight Based on Vehicle Class.

CORSIM can provide traffic simulations that track vehicle movement across lanes and across the length of the bridge. The WIM data may then be invoked to give each vehicle in the CORSIM traffic stream a reasonable set of wheel loads, creating a load history for the bridge as a function of time and placement on the bridge deck. At any given time during the simulation, this load history can identify the location and magnitude of all wheel loads on the bridge.

Another critical input parameter is the frequency with which each vehicle class occurs. CORSIM organizes vehicle classes into a fleet component category to group similar types of vehicles. Therefore, both fleet component percentages and relative percentages are needed to determine vehicle frequency. Initially, the relative percentages and fleet percentages provided directly by the WIM data were used to create simulations for links 13 and 19. However, it was later determined that the original percentages represented an excessive amount of truck traffic. Therefore, the simulations that contain these percentages were considered an unattainable upper limit. To obtain more realistic percentages, two additional sets of simulations were performed by assuming the truck fleet component was 10 and 20 percent. This is in contrast to the approximately 80 percent truck fleet component shown by the WIM data. However, the fleet percentages remained the same regardless of the truck fleet component used. Additionally, the

passenger car fleet component was increased to account for the reduction in the truck fleet component. In this way, more realistic traffic simulations can be obtained.

One-hour blocks of traffic for AM peak, off-peak, and PM peak were each obtained for all three truck fleet component percentages and for both links. This produced a total of 18 different traffic simulations, identified by link number, percent of trucks, and peak period.

In its initial form, CORSIM output is provided at 1-second intervals. A vehicle moving at 60 mph traverses 88 ft/second. At this speed, the vehicle crosses the case-study bridge in ≈4.6 seconds, with at most only five CORSIM records shown. To overcome this problem, a Fortran program, TRFASSEM.F, was written to use the acceleration and velocity information given in the CORSIM records to calculate vehicle position at every 0.1 seconds, providing an average of 50 records for each vehicle traveling across the case-study bridge. Equation 2 is the standard Newtonian mechanics equation describing particle motion and was used to refine vehicle positions between CORSIM time steps.

$$x' = \frac{1}{2}at^2 + vt + x\,. \qquad \text{(Equation 2)}$$

In addition to calculating vehicle positions, the program also sorts traffic records by time. A flowchart illustrating the major processes of the program is shown in Figure 13. The output file from TRFASSEM.F gives a time history of traffic for the bridge in question. Eighteen such histories were created, corresponding to the CORSIM traffic models for the two different lengths with truck fleet and traffic peak variations. When combined with WIM data, these time histories can give a realistic loading scenario for the bridge.

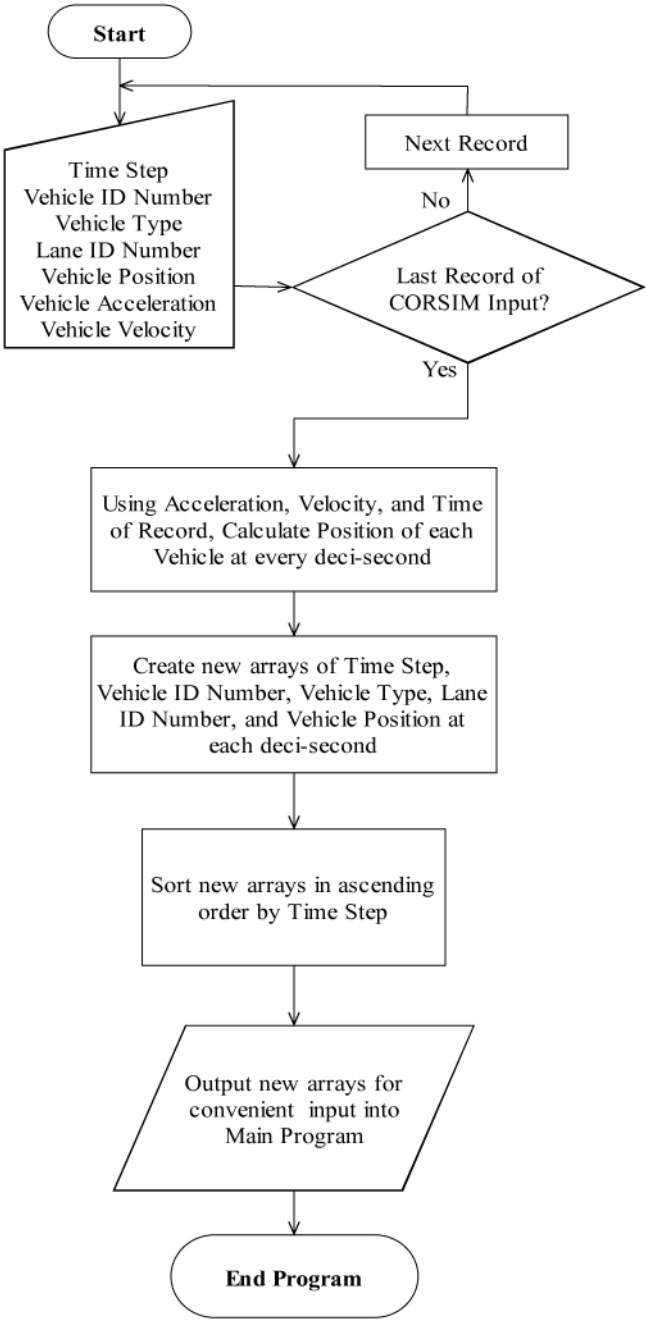

Figure 13. Flowchart Describing Functions of the TRFASSEM.F Program.

Structural Response Simulation

The traffic simulation provided by CORSIM and WIM provides the flexibility to place multiple vehicles on the bridge at any given time, thus creating a wealth of loading configurations. Our finite element analysis (FEA) solutions must exhibit the same flexibility, since a process that requires problems to be resolved for each new load configuration would

become cumbersome to the extent of impracticality. Linear superposition provides this flexibility.

In linear superposition, a finite-element model can be solved for a "unit" load placed at varying locations along the bridge. The solution at a given point may then be scaled according to actual vehicle weight and added to solutions for other vehicles, thus building a picture of reactions from the total load history. This process is illustrated in Figures 14 and 15.

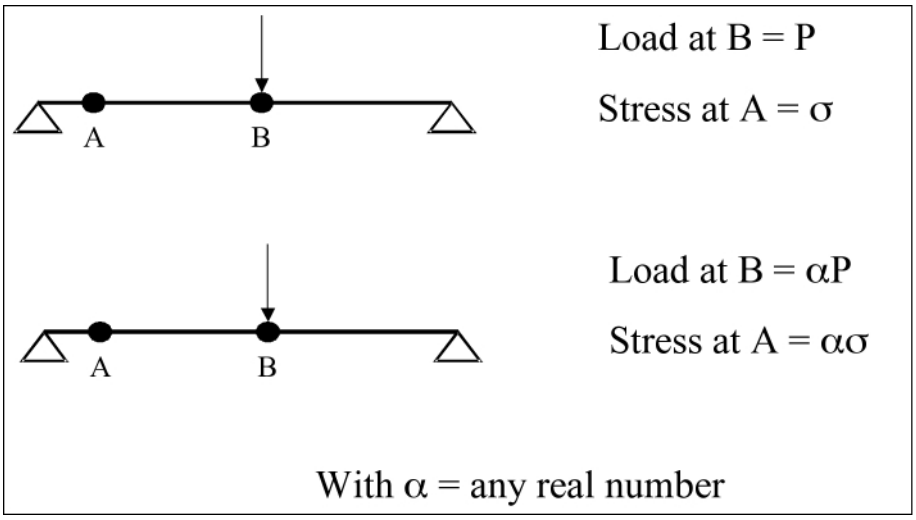

Figure 14. Concept of Load and Stress Proportionality in a Linear System.

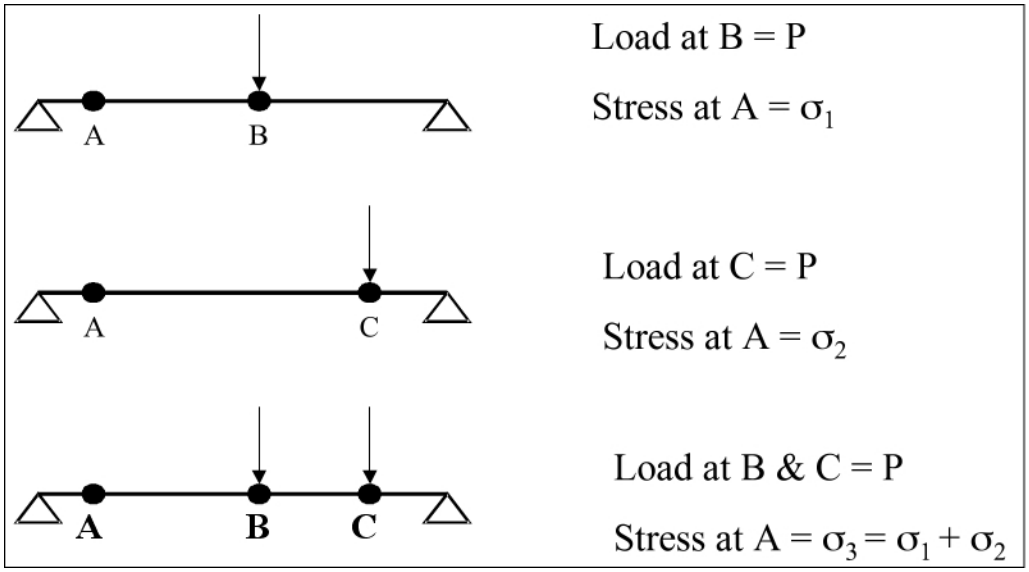

Figure 15. Concept of Linear Superposition.

Of course, in order for linear superposition to be valid, the total stresses in the bridge due to dead and live loads must be below the yield point of the steel. This assumption seems reasonable since the design of bridges includes safety factors to avoid the limit state of yielding. Therefore, stresses in the girders will be in the linear elastic region and can be scaled and combined as any linear system. This simplifying, yet realistic, assumption reduces calculation of stresses in the bridge members to addition and multiplication of the stresses that result from unit loads. (Note that the nonlinearity arising from contact in the model had negligible impact on the stress results because the live load to dead load ratios encountered in this problem were not large enough to cause uplift at the supports.)

Having provided the framework for combining the individual FEA results, the application of these loads to the models themselves can be discussed.

An accurate model of bridge loading must account for both the self-weight of the structure as well as the traffic loads that travel across the deck. The ABAQUS distributed load feature imposed the self-weight of the bridge by using the gravity parameter on the *DLOAD command (3). ABAQUS uses the defined material densities, model geometry, and specified gravity acceleration to apply the self-weight to the bridge. The self-weight load was applied only to the global model because the displacements are enforced on the nodes of the local model. Applying self-weight to the local model would have caused the effects of dead weight to be counted twice.

To account for the traffic live loads, all possible wheel load locations needed to be determined. In a real structural system, wheel loads can be applied anywhere on the bridge deck. However, using the same idea of discretization that FEA uses, the bounded, continuous, two-dimensional area of the bridge deck can be represented by a grid. Each point on the grid is a load application point where a wheel load can act. Regardless of the exact location of a vehicle on the bridge, each of the wheel loads is assigned to the nearest possible load application point. By increasing the refinement of the grid, the number of points where wheel loads can act increases, and by choosing an adequate level of refinement, the grid can closely approximate the actual continuous nature of the bridge deck.

Figure 3 shows a grid of load application points on the top of the concrete deck. The grid of load application points consisted of six wheel lines, two each for the three lanes of traffic, and discrete load application points along those lines at stations spaced 3 m (10 ft) apart. A total of

246 load application points were thus created. The longitudinal spacing was determined taking into account an estimate of average vehicle velocity entering the bridge and a 1 deci-second vehicle position update during the analysis process. In this way, a finite number of possible locations were generated upon which a wheel load could act. Regardless of the exact location of a simulated vehicle on the bridge, each of the wheel loads was assigned to its nearest pre-established load application point (see Figure 3). Wheel loads were represented as concentrated loads at their assigned nodes.

To complete the analysis, a database of finite element results was built using every load application point. Global analyses were performed with a "unit" point load at each of the load application points. The effects of self-weight were also included in all 246 global analyses. Each global results file was then used to drive a local model analysis. Local model analyses may then be combined as necessary to create stress tensor profiles for the dapped region.

This information was used to find the stresses in the dapped region under any arbitrary traffic load using the main Fortran program, as will shortly be described. Point loads of 10 kips served as the "unit" load, since a more intuitive 1-kip point load would create stresses so small that their effects would be lost to computational round off. Division of the stress tensor results by an order of magnitude is then required and was performed in the main program.

An ABAQUS FEA provides two main types of output: binary files with a "fil" extension and American Standard Code for Information Interchange (ASCII) files with a "dat" extension. The "fil" files are used by Patran to create graphic representations of stress and displacement fields. The "dat" files contain the stress tensors at every node in the local model.

These results files are typically very large and inconvenient for practical purposes. Therefore, a Fortran program, ASSEM3.F, was written to extract stress tensor information for specific nodes. This program allows the user to examine different nodes in the dapped region. In this way, an FEA only has to be performed once for each loading condition. If the region of interest changes at a later time, it is necessary to rerun only the Fortran program and not the ABAQUS FEA. The ABAQUS stress assembler removed relevant data from local analyses of the rounded dap. The stress tensors for user-specified nodes are then written in a manner that may be input to the main simulation program (to be described shortly).

Where possible, model symmetry was exploited in the analyses to reduce the number of required analyses. The notched global model is symmetric about the x-y plane in the middle of

the bridge; this symmetry did not exist for the tapered girder. However, girders for all three dapped details are symmetric about x-y planes through the center of the girder webs.

In order to take advantage of symmetry, the response due to a load must equal the response at a mirrored location due to a load of equal magnitude applied at that location. This principle is illustrated in Figure 16. A mirrored location is defined as a location that is on the same perpendicular line and the same distance to the x-y plane of symmetry as the location it mirrors. This fact is useful since half of the load application points are symmetric about the x-y plane in the middle of the bridge with the notched detail. Therefore, the stress tensors that result from the first half of the analyses can predict the stress tensors for the second.

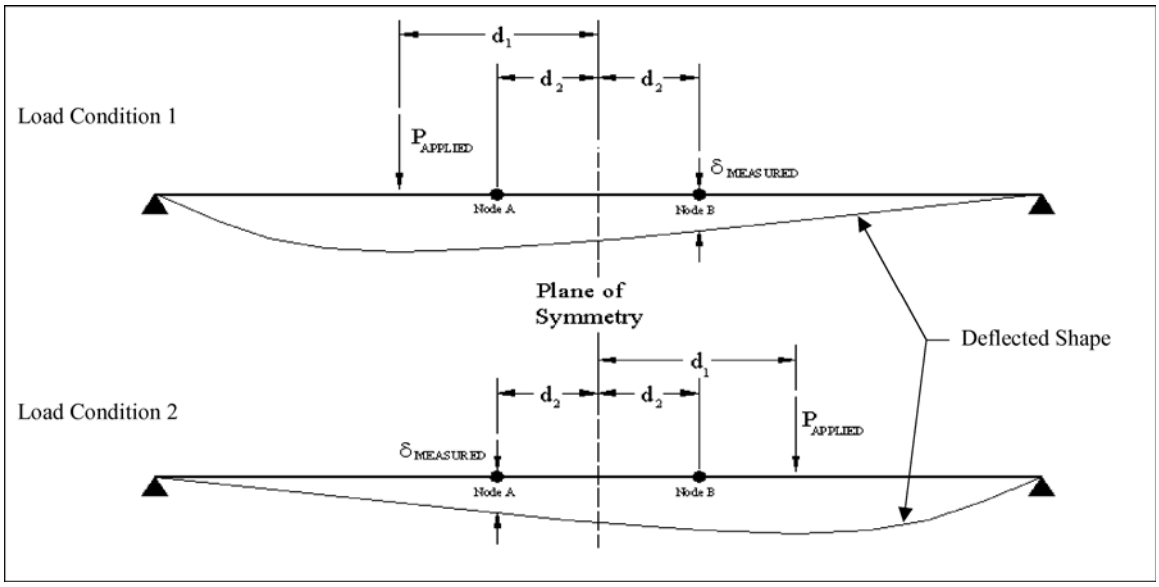

Figure 16. Illustration of Symmetric Response for Mirror Nodes.

The ABAQUS stress assembler program uses the spatial coordinates from the local model input file to find the location of the "mirror" nodes. When creating the input file for the main Fortran program, the assembler program finds the stress tensor at a mirror node when looking for a stress due to a load at a mirror location. One side effect of exploiting symmetry in this fashion is a sign change of two components of the stress tensor. Two of the shear components, τ_{xz} and τ_{yz}, reverse their direction in the mirroring process (see Figure 17). The signs of these two components change if the stress quantities are obtained from a mirror node.

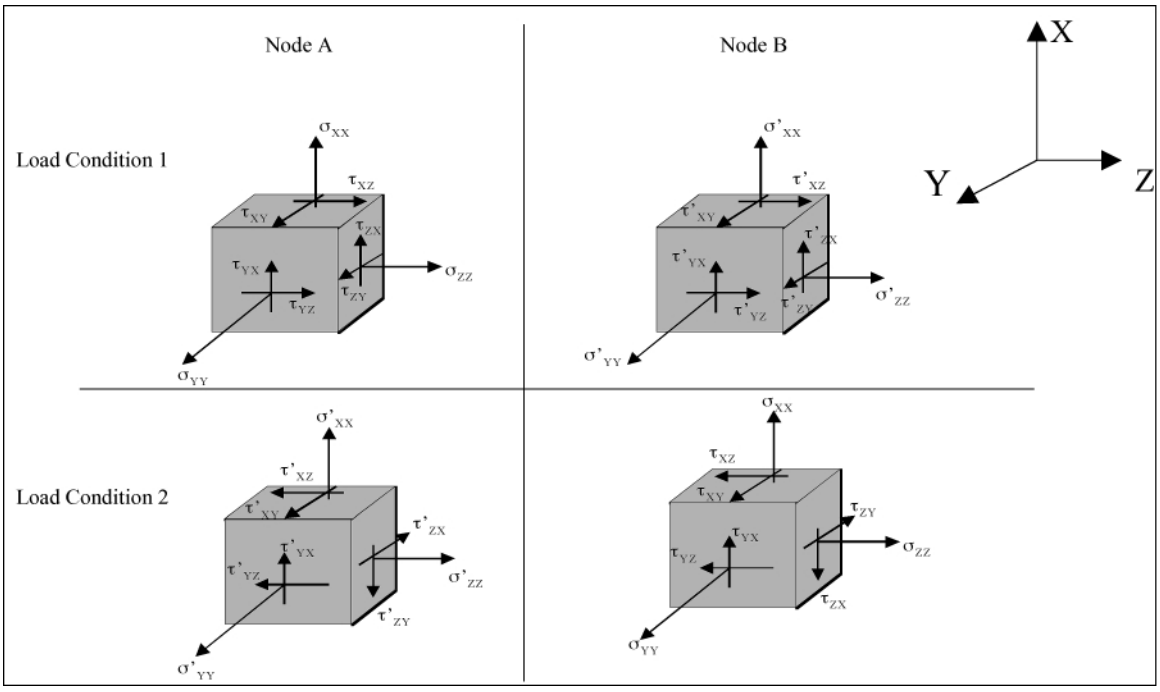

Figure 17. Symmetry of Shear Stresses.

See Figure 18 for a flowchart of this program. The main routine of this program concerns finding the correct nodes and any relevant mirror nodes. The extraction of stress tensors occurs in a subroutine, a flowchart of which is shown in Figure 19.

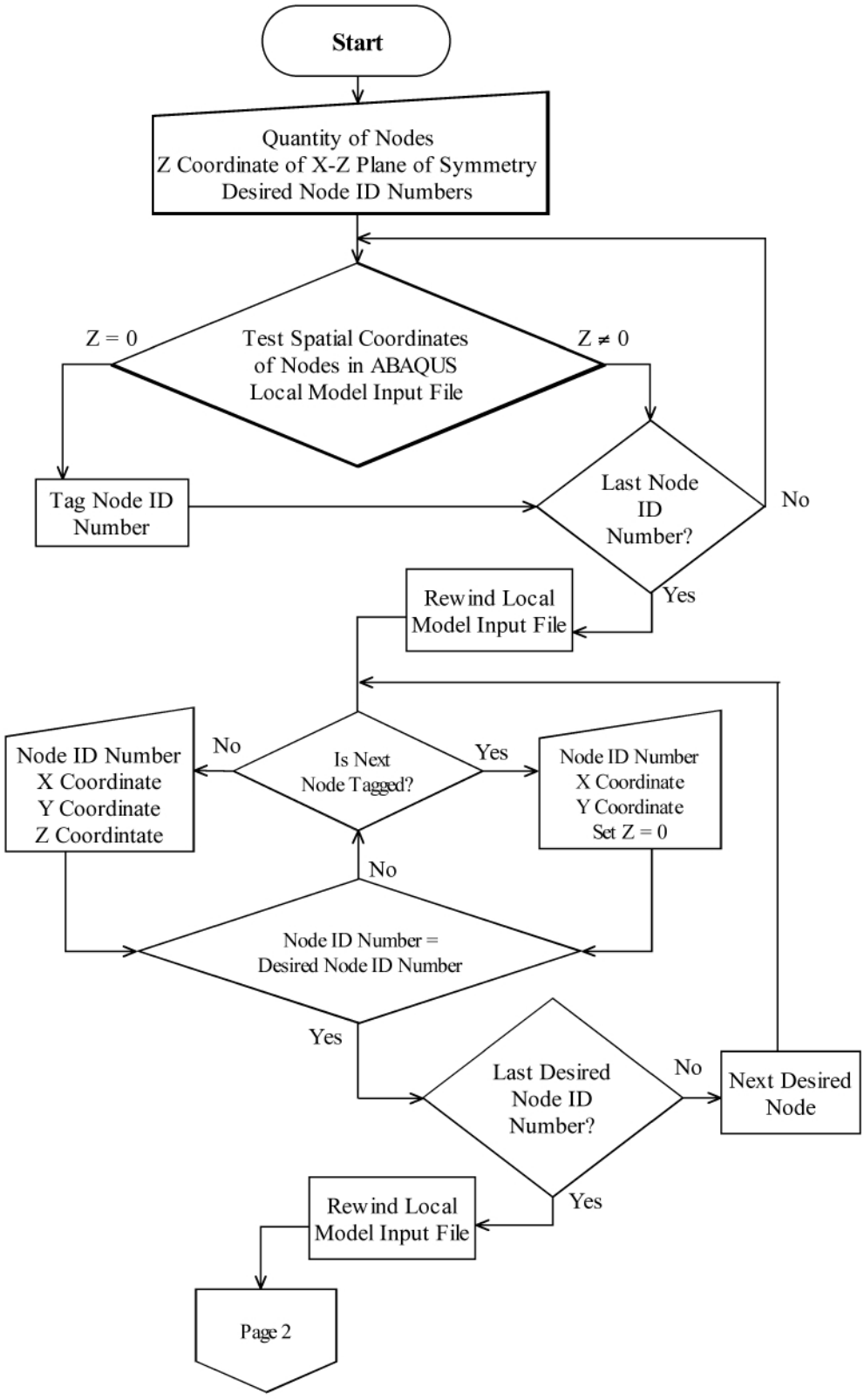

Figure 18. Flowchart for the Stress Assembler Program.

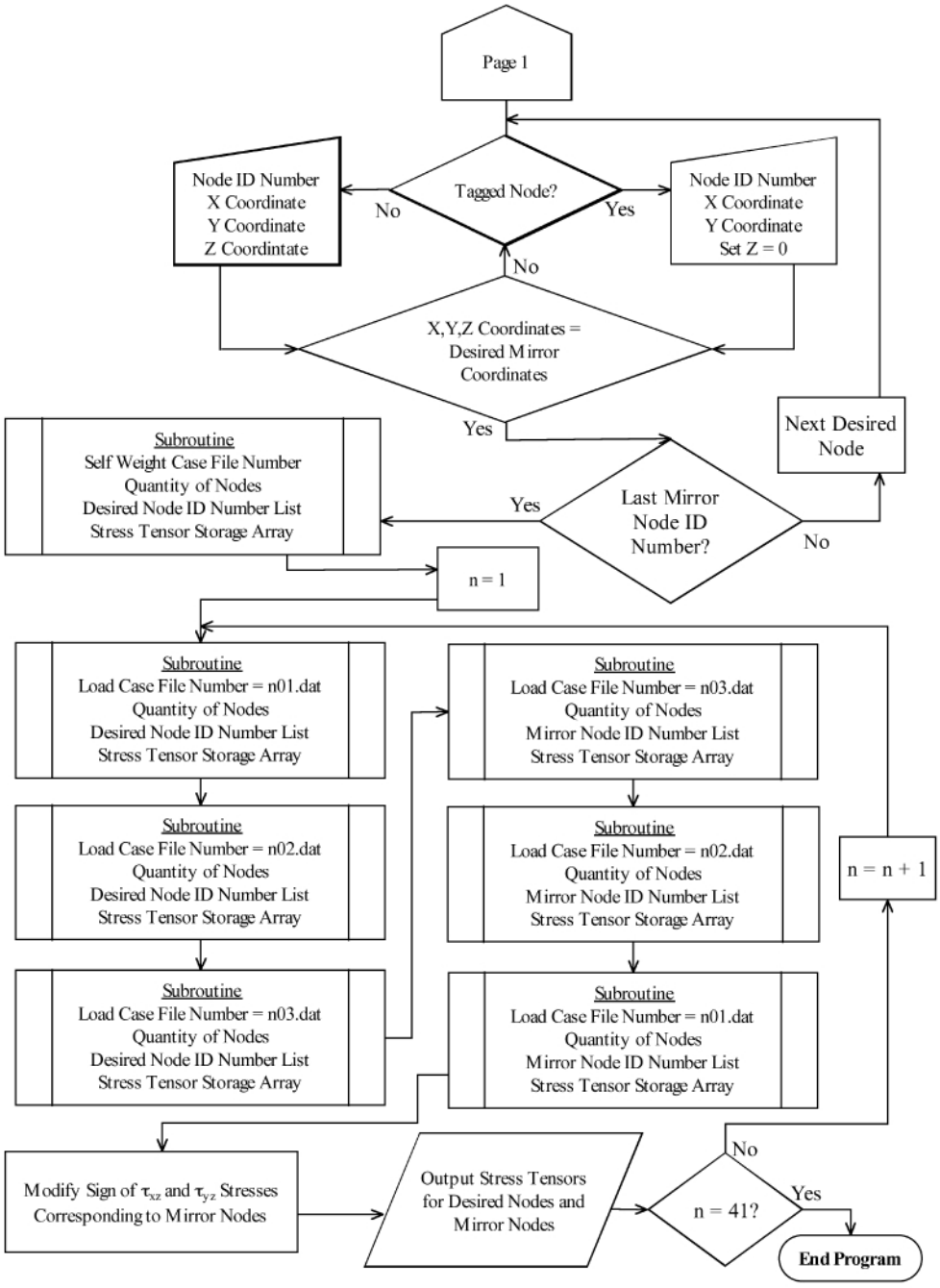

Figure 18. Flowchart for the Stress Assembler Program (continued).

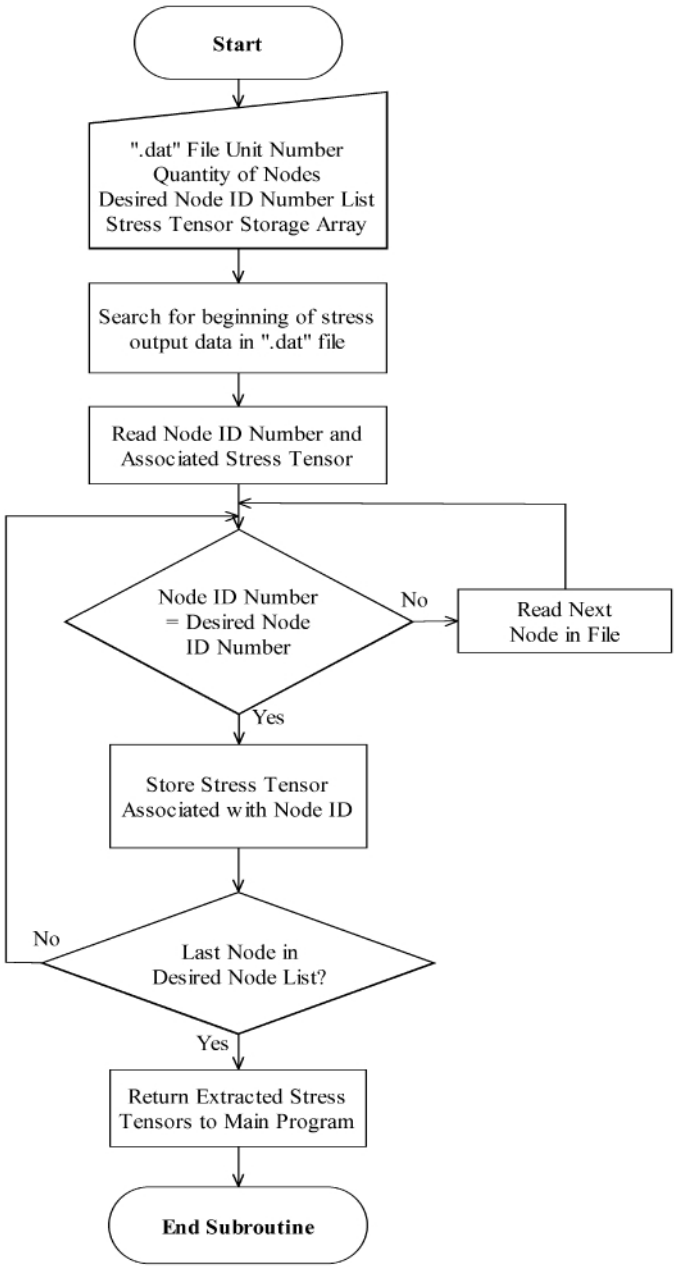

Figure 19. Flowchart for Stress Extractor Subroutine.

During load application, the prevention of support uplift becomes very important to the global model analysis. Uplift is defined as the change of a compressive support reaction to a tensile reaction. In reality, normal traffic loads do not cause girders to lift from the supports. However, a combination of loads that will cause uplift in the finite-element model is conceivable. If a global model with uplift were used to drive a local model, the results would

have no physical meaning. The local model contact interaction assumes that the girder and bearing pad begin in contact. Violation of this assumption produces meaningless results. In order to check for uplift, reactions due to self-weight at every support in the global model need to be calculated.

Integration of the vertical stress across the midthickness of each bearing pad provides the required support reaction. A Fortran program, BREACT.F, was created to perform this operation on the global model output. Using the spatial coordinates and known dimensions of each bearing pad, the program extracts the vertical stress components from these locations and integrates them over the area of the bearing pad to produce the support reaction. Reactions resulting from the 246 "unit" load analyses, which included self-weight, were calculated. The reaction at each support due to self-weight alone was then subtracted. The result is the change in each reaction support due to a "unit" load at each load application point. This information, when provided to the main Fortran program, can be used to test for uplift at any support. A flowchart of this program is shown in Figure 20 below; it also makes use of the extraction subroutine shown in Figure 19.

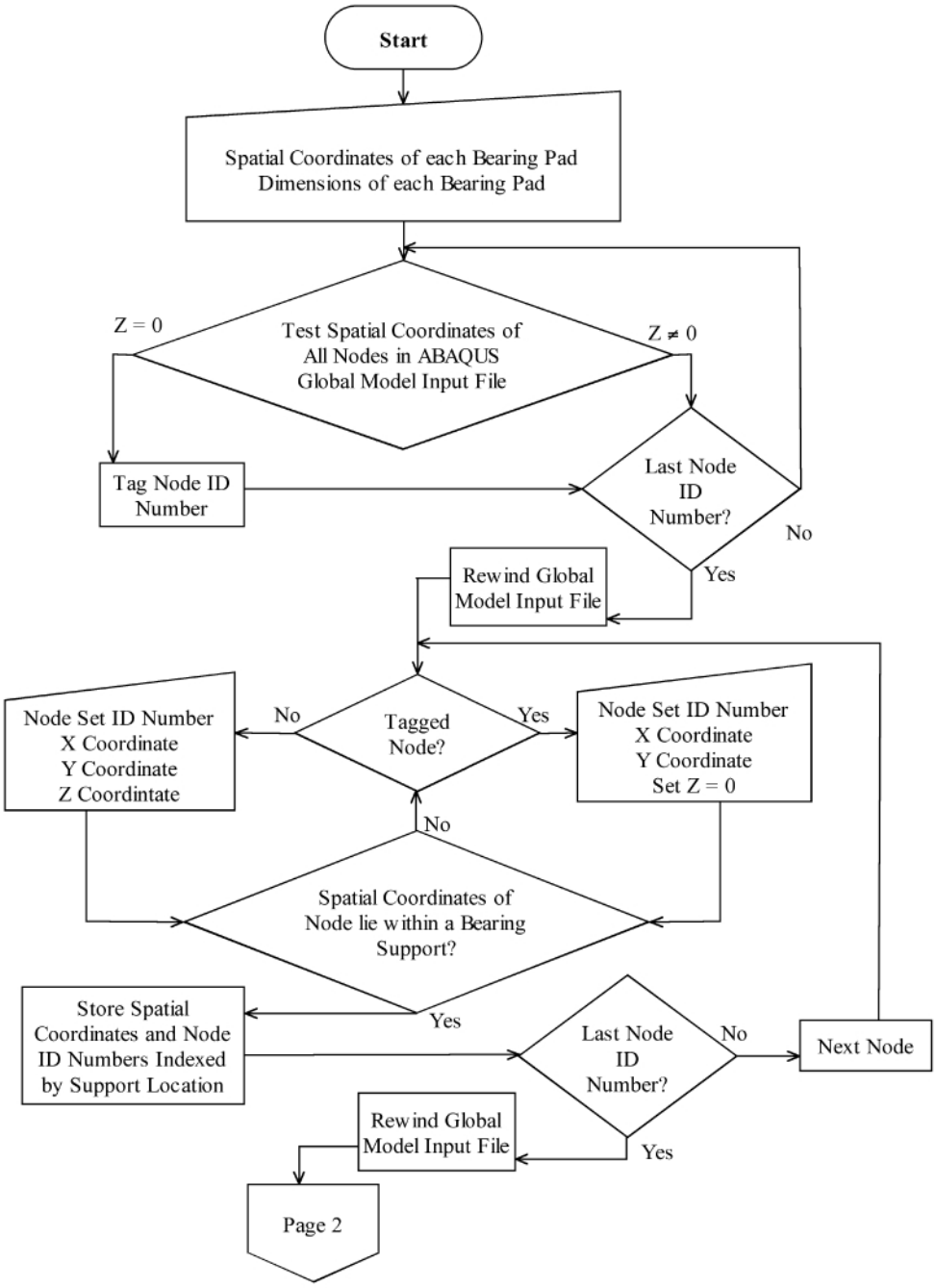

Figure 20. Flowchart for Program to Check Uplift.

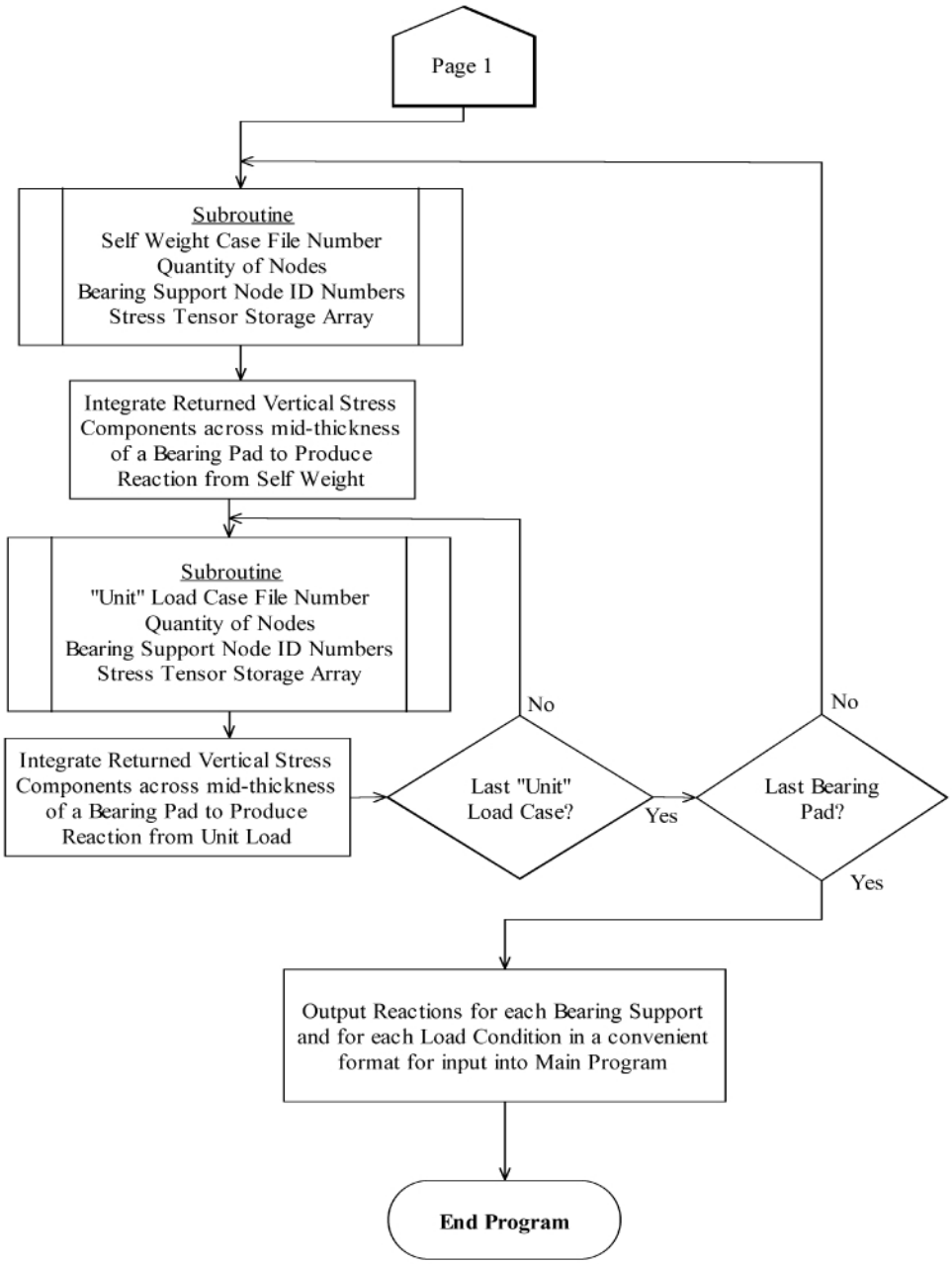

Figure 20. Flowchart for Program to Check Uplift (continued).

Calculation of Structural Response and Component Stress Histories

This section explains how the separate components of this simulation (finite element, WIM data, and CORSIM model output) may be combined to form a coherent picture of traffic

effects on a structural system. Details of the Montgomery County bridge are presented as a reference case.

The functions of programs TRFASSEM.F, ASSEM3.F, and BREACT.F have already been described. Each program creates an output file used in the final Fortran program, MAIN.F. MAIN.F also has access to the WIM database to find representational vehicle wheel loads, as previously described. The main program combines and processes the assembled FEA stress tensors, the assembled CORSIM traffic simulation, the organized WIM data, and the support reaction data. The final output of this program is stress histories for the locations of interest within the local model.

This program has three main functions. First, it generates a pseudo-random vehicle weight for every vehicle in the CORSIM traffic stream using the WIM data (as illustrated in Figure 12). This weight and the vehicle locations provided by CORSIM then allow a linear combination of stress tensors to represent the effects of traffic on the bridge at any given instant in time. Thus, a "snapshot" of the stress state is created at each point in the load time history; this process continues for the entire time period simulated in CORSIM, using deci-second increments calculated by TRFASSEM.F. Finally, the bridge is checked for uplift. A flowchart for the main program is presented in Figure 21.

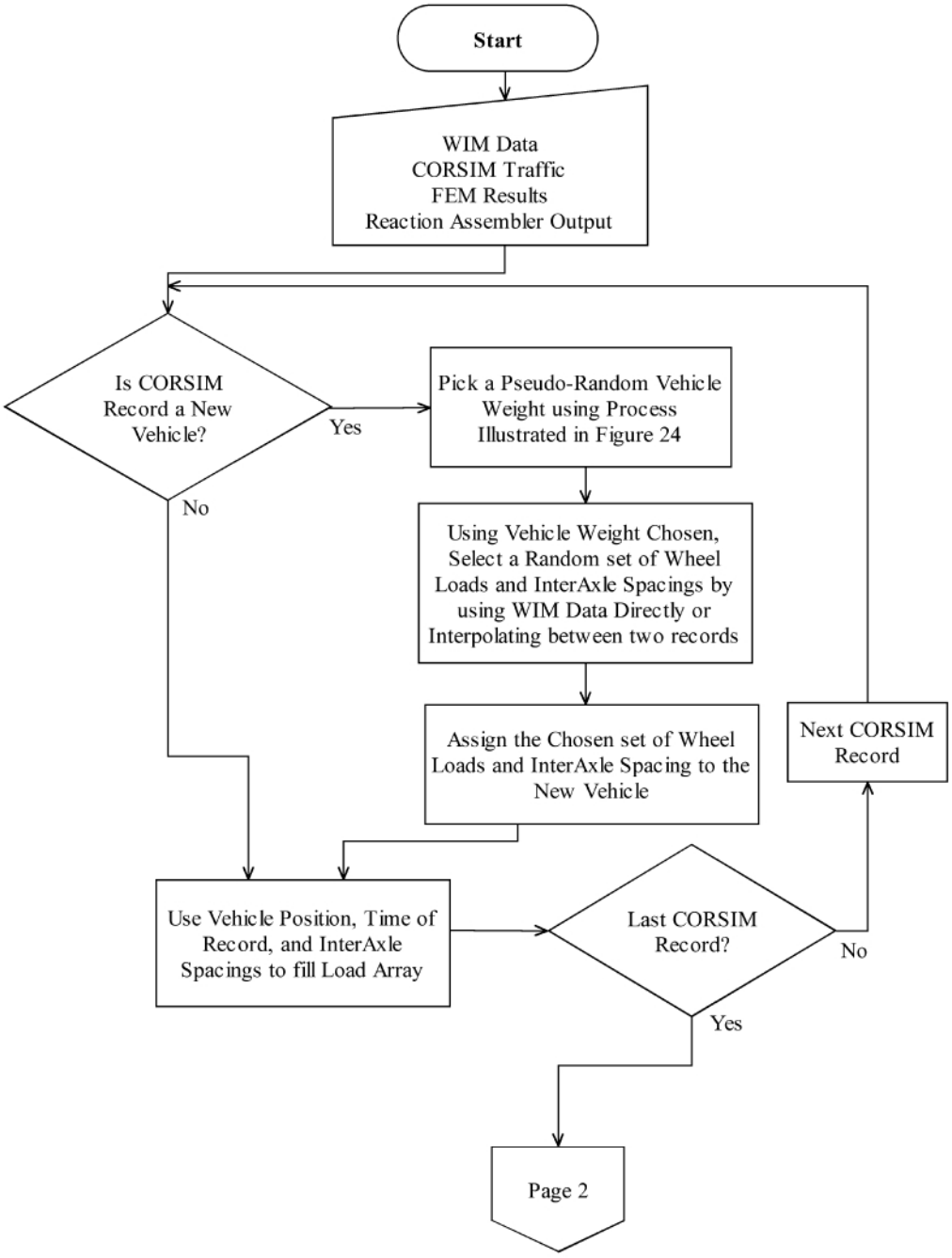

Figure 21. Flowchart for the Main Fortran Program.

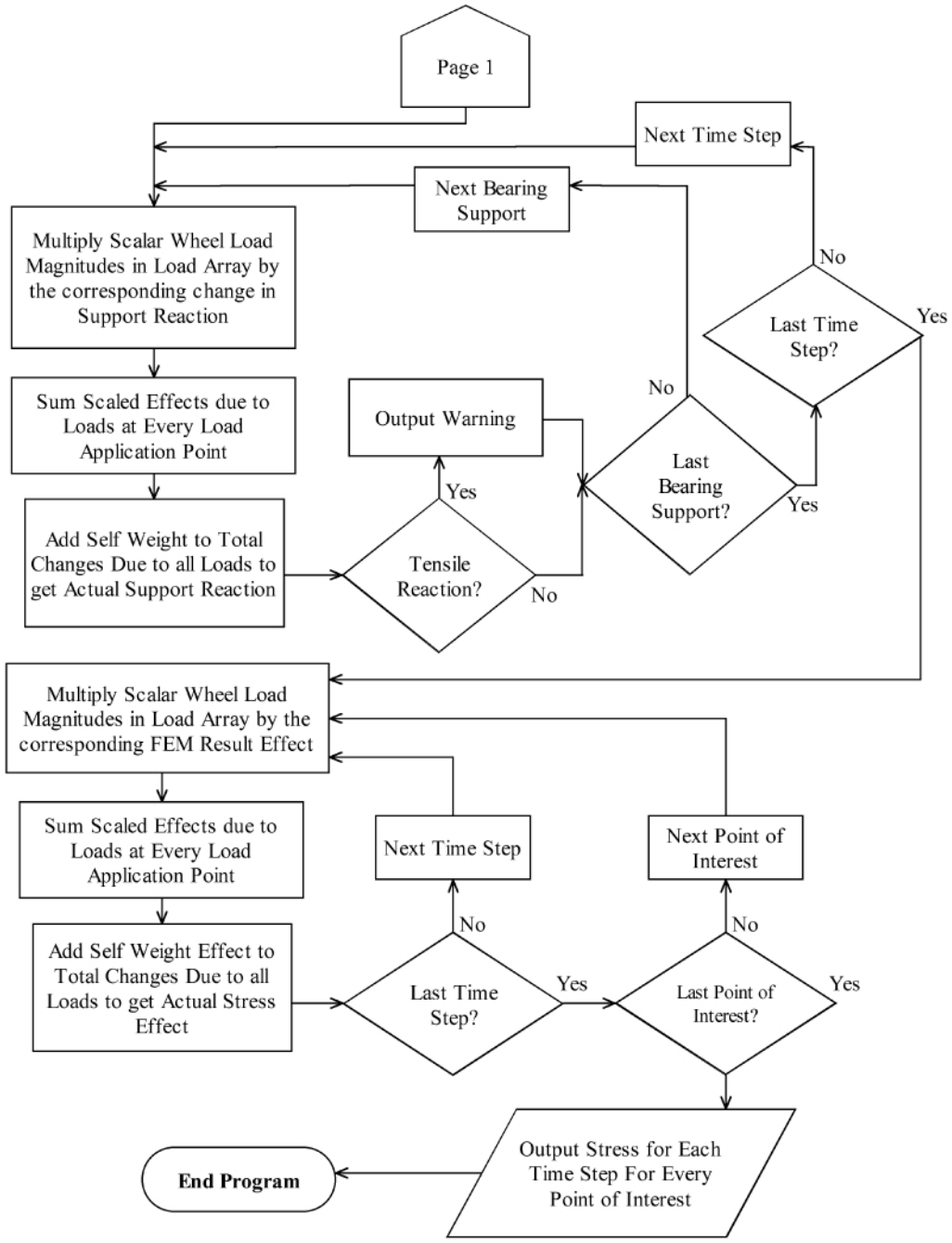

Figure 21. Flowchart for the Main Fortran Program (continued).

At an earlier stage of this analysis, it was assumed that the bridge behavior would remain linear under applied traffic loading; this assumption allowed the use of linear superposition and greatly reduced the required number of FEAs. An ABAQUS analysis with multiple scaled point loads tested the validity of this assumption. The results of this analysis were compared with

results obtained through linear superposition. Table 1 shows numerical values for these two analyses. Table 2 shows the values used for linear superposition.

Table 1. Verification of Analysis Procedure.

Test File - 30 kip Load Placed at L_1, L_2, and L_3

Node	σ_x	σ_y	σ_z	τ_{xy}	τ_{yz}	τ_{xz}
40	3.217E-01	-2.293E-01	2.646E-02	-1.449E+00	1.179E-03	1.152E-04
41	3.362E-01	-2.573E-01	3.084E-02	-1.439E+00	9.756E-04	3.426E-04
42	3.418E-01	-2.281E-01	2.747E-02	-1.423E+00	6.517E-04	1.073E-04
43	3.476E-01	-2.140E-01	3.328E-02	-1.430E+00	7.175E-04	7.164E-05
44	3.483E-01	-2.098E-01	3.393E-02	-1.435E+00	7.835E-04	7.067E-05
45	3.463E-01	-2.130E-01	3.193E-02	-1.440E+00	8.494E-04	7.298E-05

Linear Combination - $30(L_1\text{-SW})+30(L_2\text{-SW})+30(L_3\text{-SW})+SW$

Node	σ_x	σ_y	σ_z	τ_{xy}	τ_{yz}	τ_{xz}
40	3.216E-01	-2.293E-01	2.645E-02	-1.449E+00	1.185E-03	1.164E-04
41	3.359E-01	-2.572E-01	3.083E-02	-1.442E+00	9.818E-04	3.437E-04
42	3.418E-01	-2.283E-01	2.746E-02	-1.423E+00	6.579E-04	1.084E-04
43	3.477E-01	-2.143E-01	3.326E-02	-1.430E+00	7.239E-04	7.264E-05
44	3.481E-01	-2.098E-01	3.391E-02	-1.436E+00	7.899E-04	7.161E-05
45	3.464E-01	-2.132E-01	3.191E-02	-1.441E+00	8.559E-04	7.384E-05

Percent Difference

Node	σ_x	σ_y	σ_z	τ_{xy}	τ_{yz}	τ_{xz}
40	0.0%	0.0%	0.0%	0.0%	0.5%	1.0%
41	-0.1%	0.0%	0.0%	0.2%	0.6%	0.3%
42	0.0%	0.1%	0.0%	0.0%	1.0%	1.0%
43	0.0%	0.1%	0.0%	0.0%	0.9%	1.4%
44	-0.1%	0.0%	0.0%	0.1%	0.8%	1.3%
45	0.0%	0.1%	0.0%	0.1%	0.8%	1.2%

Table 2. Unit Load Results for Analysis Verification.

L_1 - Unit Load Location 1

Node	σ_x	σ_y	σ_z	τ_{xy}	τ_{yz}	τ_{xz}
40	3.251E-01	-2.288E-01	2.737E-02	-1.457E+00	4.583E-04	3.857E-05
41	3.396E-01	-2.569E-01	3.177E-02	-1.447E+00	3.813E-04	1.243E-04
42	3.452E-01	-2.276E-01	2.839E-02	-1.431E+00	2.617E-04	3.571E-05
43	3.511E-01	-2.134E-01	3.423E-02	-1.438E+00	2.876E-04	2.214E-05
44	3.518E-01	-2.092E-01	3.489E-02	-1.444E+00	3.136E-04	2.179E-05
45	3.498E-01	-2.123E-01	3.289E-02	-1.449E+00	3.395E-04	2.319E-05

L_2 - Unit Load Location 2

Node	σ_x	σ_y	σ_z	τ_{xy}	τ_{yz}	τ_{xz}
40	3.283E-01	-2.284E-01	2.823E-02	-1.464E+00	-7.066E-06	-1.264E-06
41	3.429E-01	-2.566E-01	3.265E-02	-1.455E+00	-5.746E-06	-2.761E-06
42	3.485E-01	-2.271E-01	2.927E-02	-1.438E+00	-3.404E-06	-1.202E-06
43	3.544E-01	-2.128E-01	3.514E-02	-1.445E+00	-3.749E-06	-9.781E-07
44	3.551E-01	-2.086E-01	3.581E-02	-1.451E+00	-4.095E-06	-9.710E-07
45	3.531E-01	-2.117E-01	3.381E-02	-1.456E+00	-4.440E-06	-9.422E-07

L_3 - Unit Load Location 3

Node	σ_x	σ_y	σ_z	τ_{xy}	τ_{yz}	τ_{xz}
40	3.290E-01	-2.283E-01	2.844E-02	-1.466E+00	-5.532E-05	2.119E-06
41	3.436E-01	-2.565E-01	3.286E-02	-1.456E+00	-4.780E-05	-5.970E-06
42	3.493E-01	-2.270E-01	2.948E-02	-1.440E+00	-3.920E-05	2.224E-06
43	3.552E-01	-2.127E-01	3.536E-02	-1.447E+00	-4.280E-05	3.613E-06
44	3.558E-01	-2.084E-01	3.603E-02	-1.453E+00	-4.639E-05	3.604E-06
45	3.539E-01	-2.116E-01	3.403E-02	-1.458E+00	-5.000E-05	2.865E-06

SW - Self Weight

Node	σ_x	σ_y	σ_z	τ_{xy}	τ_{yz}	τ_{xz}
40	3.282E-01	-2.284E-01	2.821E-02	-1.464E+00	2.795E-07	2.383E-07
41	3.428E-01	-2.566E-01	3.263E-02	-1.454E+00	1.748E-07	3.669E-07
42	3.484E-01	-2.271E-01	2.924E-02	-1.438E+00	-8.789E-08	2.286E-07
43	3.543E-01	-2.128E-01	3.512E-02	-1.445E+00	-8.655E-08	2.108E-07
44	3.550E-01	-2.086E-01	3.579E-02	-1.451E+00	-8.522E-08	2.076E-07
45	3.530E-01	-2.117E-01	3.378E-02	-1.456E+00	-8.397E-08	1.884E-07

These data show little difference between the linear combination results and those obtained by directly analyzing the bridge with applied loads. ABAQUS analyses provided the stresses for “unit” loads placed at every load application point. Therefore, the effect resulting from any number of loads (of arbitrary magnitude), placed at the load application points, can be found in the dapped region. Thus, the traffic data, with pseudo-randomly chosen wheel loads, can be used to fill a “load” array, which contains the scalar quantity equal to the wheel load divided by the “unit” load used to perform the local model analyses. Each scalar quantity in the load array is indexed by its position on the load application grid and by the time the wheel load occurs during the 1-hour time frame. The data provided by the ABAQUS stress assembler are read into an “effect” array. Using the correct indicial notation in the Fortran program, the stress

effects can be scaled and added to produce a single stress tensor for each node at every instant in time.

This load array is also used to check for uplift; in this case, the effect array is made of support reaction values. The reaction calculator, as described above, assembled the change in support reactions due to a "unit" load at each load application point. Again, using the correct indicial notation, the load and effect arrays produce the change in support reactions due to the load configuration on the bridge at any given instant. This overall change in support reactions, when added to the self-weight reactions, produces the new support reaction at each time. If none of the support reactions change in sign from compressive to tensile, then there is no uplift.

The final output of the main program is stress histories at selected nodes of interest in the local model, as well as reaction histories at the bearing pad. The analysis program can be run with different CORSIM traffic, with different random weights, and on different locations in the dapped region. These stress and reaction histories can then be used in a fatigue life analysis of the dapped region.

EXAMPLE ANALYSIS RESULTS

A brief synopsis of numerical results is presented as Figures 22 through 24 for the notched, rounded, and tapered details, respectively. In these figures the von Mises yield function values, taken from critical local regions of each detail, are plotted against elapsed time from the start of the AM peak traffic flow for 1 hour. It is clear that the most sensitive among the details is the notched detail. The average range of local yield function stress for the notched detail is approximately 8 ksi, while the tapered detail and the 90-degree rounded detail each exhibit a local yield function stress range of approximately 4 ksi.

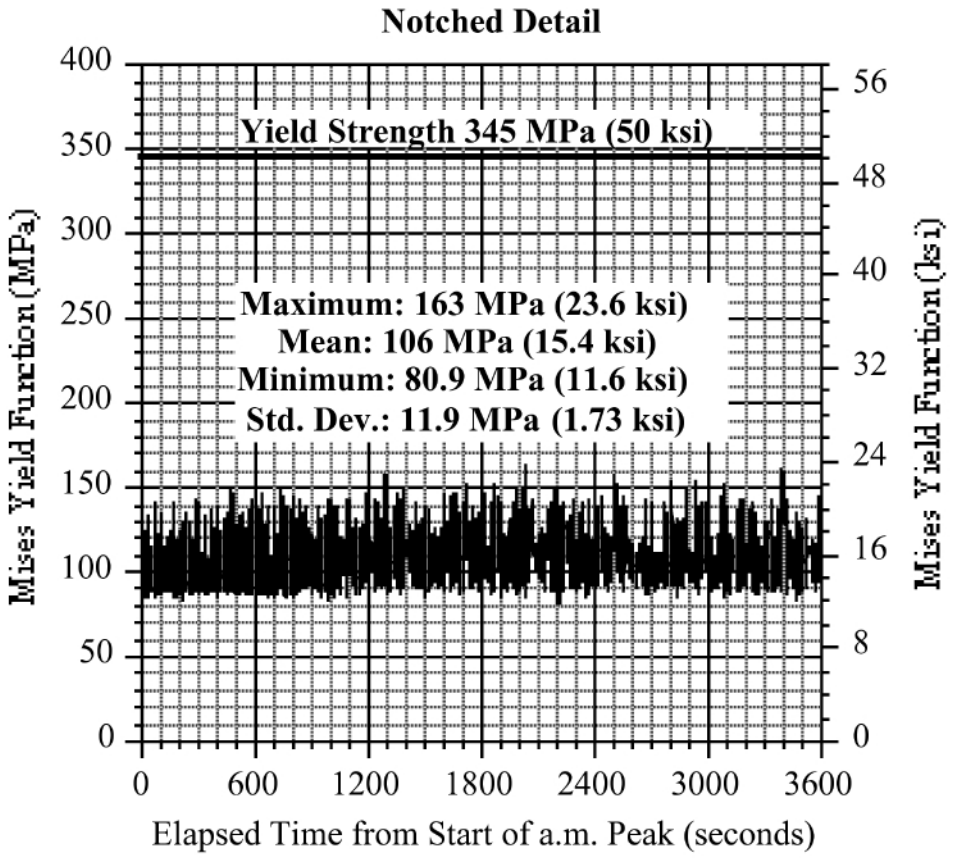

Figure 22. Plot of von Mises Yield Function History for Notched Detail.

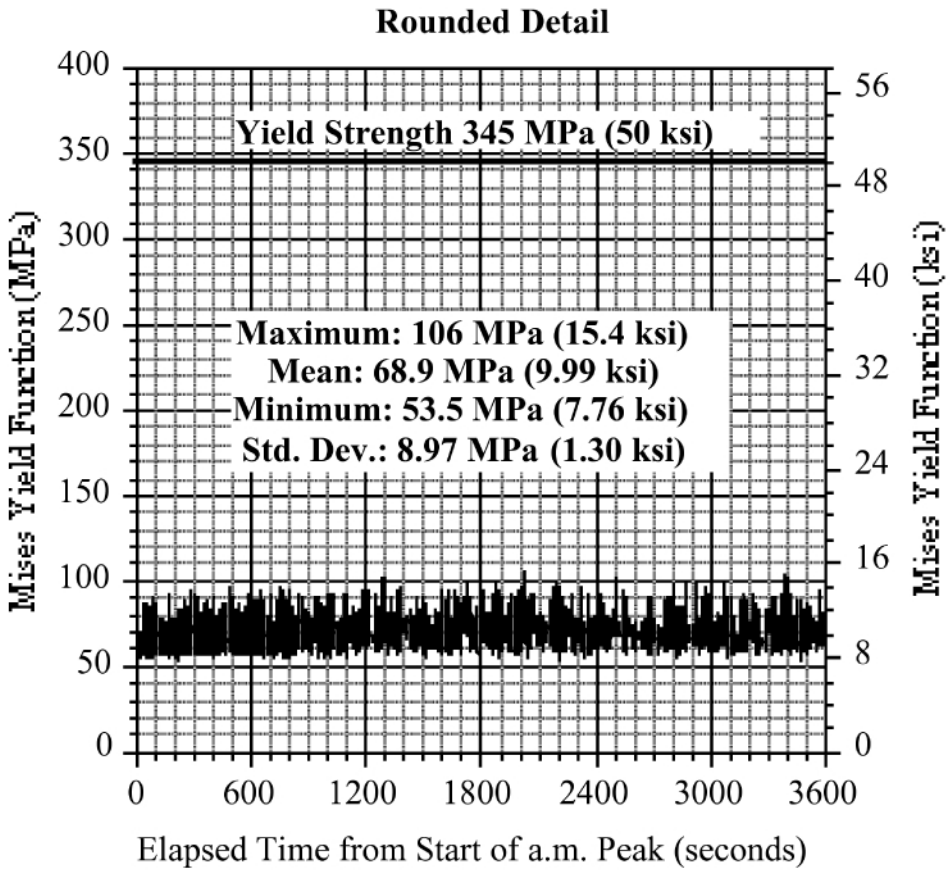

Figure 23. Plot of von Mises Yield Function History for Rounded Detail.

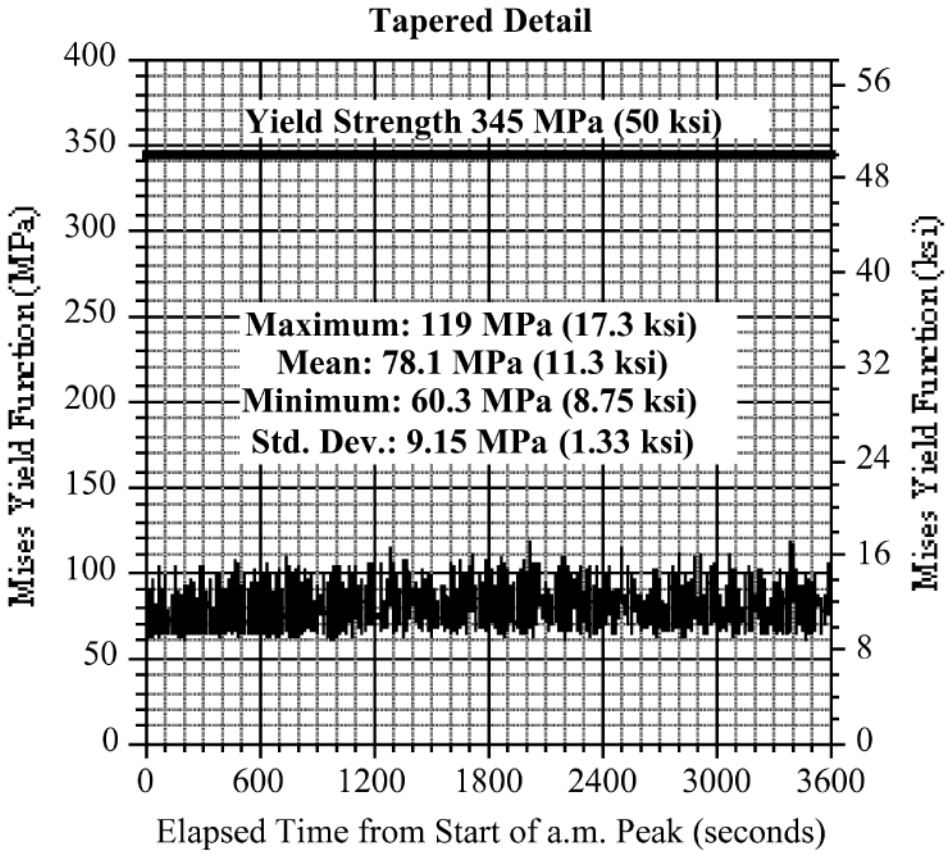

Figure 24. Plot of von Mises Yield Function History for Tapered Detail.

CHAPTER 3:
FATIGUE BEHAVIOR OF DAPPED GIRDER END DETAILS

CHAPTER OVERVIEW

The main objective of the simulation process described in Chapter 2 is to create a realistic representation of the stresses imposed on dapped girder end details under service live-load conditions. In this chapter, that information is used in two ways: (1) as input to a parameter that measures fatigue damage and (2) to determine a variable amplitude block loading history that will be applied directly to large-scale fatigue specimens of each detail in laboratory tests.

FATIGUE ANALYSIS

Analytical Procedures

In general, the stress histories experienced at critical locations in the dapped end details under live load have the following characteristics:

- Variable amplitude – The stress *ranges* to which the details are subjected vary in magnitude within each loading block.
- Multi-axial – At critical locations in the dapped regions, two or more of the stress tensor components are nonnegligible.
- Low amplitude – The maximum stresses experienced are well below the yield point of the steel, leading to long fatigue lives, behavior termed high cycle fatigue.

In the fatigue analysis of dapped girder ends, each of the three case-study details is subjected to simulated traffic live-load conditions using the procedures described in Chapter 2. A fatigue damage parameter, in this study Findley's parameter, will then be used to compare performance among the different details (*13*). Findley's parameter is a critical plane fatigue parameter that requires a stress tensor history to be resolved into components acting within and normal to a selection of material planes that pass through a point of interest. The maximum range of shear stress and the maximum normal stress are combined as shown in Equation 3 below to produce a parameter value for each plane. The plane that accumulates the largest parameter value through a block of loading is denoted the critical plane.

$$f = \frac{\Delta \tau_{max}}{2} + k \sigma_{max}. \qquad \text{(Equation 3)}$$

In some applications, identification of the critical plane is of interest (*14*). In the present study only the maximum parameter values for each dapped detail were used. A Fortran program was written to calculate Findley's parameter for a given stress history. The program calculated Findley's parameter for a representative range of θ and ϕ values given in Equation 4, where θ represents longitudinal angles and ϕ represents latitudinal angles. An ordered pair of these angles specifies a given plane. Normal vectors, denoted ñ, for these planes are determined by using Equation 5. As shown in Equation 6, the stress tensor, [T], can be multiplied by a normal vector to obtain the traction vector for a given plane. This traction vector is the vector sum of the shear and normal stress tractions acting in the given plane. The maximum range of shear stress traction and the maximum normal stress traction magnitude, keeping in mind its sense (tensile or compressive), are combined to produce Findley's parameter using Equation 3.

$$0° \le \theta, \phi < 180°. \qquad \text{(Equation 4)}$$

$$\tilde{n} = (\sin\phi \cos\theta)\tilde{i} + (\sin\phi \sin\theta)\tilde{j} + (\cos\phi)\tilde{k}. \qquad \text{(Equation 5)}$$

$$\tilde{t} = [T]\tilde{n}. \qquad \text{(Equation 6)}$$

An infinite number of planes pass through a given point, and there are an infinite number of points in a component; it would be impossible to sample every one. A small number of points of interest are usually selected by limiting an investigation to concentrations of tensile stress in local zones in a component. Then by selecting a suitably small degree of increment in the angles, a large, yet finite, number of planes may be examined through each point of interest.

In this project, 1-degree angle increments were used to create the set of planes to be investigated. This required the Fortran program to investigate the stress components acting on 32,400 planes at each point of interest. For each detail, the program created a stress history for the five nodes with the highest von Mises stress within zones of tensile principal stress concentration. Two zones of local tensile stress concentration are observed in the tapered detail:

one in the web plate at the apex of the bend nearer the support and the other in the flange plate at the apex of the bend that is farther from the support. In the rounded detail, two zones of local tensile stress concentration are observed, both in the web plate where it joins the curved flange plate. One zone is located between the apex of the bend and the horizontal tangent point, and the other is located between the apex of the bend and the vertical tangent point. At both locations, the maximum principal stress is tensile and nearly perpendicular to the weld joining the web plate to the flange plate. In the notched detail, two zones of local stress concentration were observed: at the reentrant corner of the notch and in the web plate at the end of the extended horizontal flange plate.

Analytical Results

A total of 54 stress histories were produced using the simulation procedure described in Chapter 2. Stress histories are identified by the following four parameters:

- three dapped types (notched, rounded, tapered),
- three traffic periods (AM peak, off-peak, PM peak),
- three different truck traffic percentages (10, 20, and 80 percent trucks), and
- two different CORSIM link locations (link 13 and link 19).

Each stress history contained values for all six independent components of the stress tensor at each deci-second of the simulation. A graph of the entire 1-hour stress history during AM peak traffic is provided for each detail in Figures 22 through 24. Visually, the stress histories are very similar to random acceleration histories, with sudden spikes and sharp decreases occurring when wheel loads traveled over the location of interest. However, in order to reduce, examine, and compare the available data, statistical properties of the stress and reaction histories were determined. Only the statistical properties of the von Mises stress were considered, but the process could be repeated for any stress component. The values calculated for each history were mean, median, mode, standard deviation, coefficient of variation, maximum, minimum, range, skewness, and skewness coefficient. In this way, the relative differences in the stress histories can be characterized. Tables 3, 4, and 5 contain the statistical properties of AM peak traffic, off-peak traffic, and PM peak traffic, respectively.

Table 3. Statistical Properties of the von Mises Stresses Obtained for AM Peak Traffic.

Period	Link	Dapped Type	Truck Traffic Percentages	Average	Median	Mode	Standard Deviation	Coefficient of Variation	Maximum	Minimum	Range	Skewness	Skewness Coefficient
AM Peak Traffic	Link 13	Notched	80%	15.57	15.34	15.37	1.66	0.107	23.52	12.01	11.51	4.040	0.878
			20%	14.50	14.13	13.16	1.44	0.100	25.07	12.19	12.88	4.100	1.364
			10%	13.86	13.51	13.16	1.05	0.076	22.86	12.05	10.81	3.030	2.619
		Rounded	80%	10.16	10.00	9.93	1.10	0.108	15.11	7.85	7.26	1.130	0.848
			20%	9.43	9.19	8.50	0.98	0.104	16.12	7.95	8.17	1.270	1.350
			10%	8.99	8.75	8.50	0.72	0.080	15.68	7.79	7.89	0.990	2.634
		Tapered	80%	11.56	11.40	11.36	1.28	0.111	17.13	8.80	8.33	1.550	0.740
			20%	10.67	10.38	9.58	1.13	0.106	18.30	8.94	9.36	1.830	1.263
			10%	10.14	9.88	9.58	0.82	0.081	17.35	8.77	8.58	1.370	2.518
	Link 19	Notched	80%	15.30	15.04	13.16	1.72	0.113	23.65	11.72	11.93	5.630	1.101
			20%	14.64	14.31	13.16	1.45	0.099	25.37	12.14	13.23	4.080	1.334
			10%	14.52	14.28	13.17	1.25	0.086	21.65	12.44	9.21	2.170	1.121
		Rounded	80%	9.98	9.81	8.50	1.16	0.116	15.40	7.75	7.65	1.570	1.020
			20%	9.52	9.31	8.50	0.99	0.103	16.51	7.88	8.63	1.280	1.337
			10%	9.44	9.29	8.50	0.84	0.089	13.95	8.04	5.91	0.650	1.096
		Tapered	80%	11.32	11.14	9.58	1.33	0.117	17.19	8.75	8.44	2.160	0.923
			20%	10.78	10.53	9.58	1.13	0.105	18.08	8.92	9.16	1.740	1.201
			10%	10.68	10.49	9.59	0.97	0.091	15.47	9.00	6.47	0.960	1.036

Table 4. Statistical Properties of the von Mises Stresses Obtained for Off-Peak Traffic.

Period	Link	Dapped Type	Truck Traffic Percentages	Average	Median	Mode	Standard Deviation	Coefficient of Variation	Maximum	Minimum	Range	Skewness	Skewness Coefficient
Off Peak Traffic	Link 13	Notched	80%	14.43	14.04	13.16	1.55	0.107	22.98	12.09	10.89	4.870	1.312
			20%	13.93	13.39	13.16	1.40	0.101	27.25	11.92	15.33	7.880	2.865
			10%	13.89	13.39	13.16	1.25	0.090	29.09	12.09	17.00	5.060	2.566
		Rounded	80%	9.39	9.12	8.50	1.05	0.112	14.85	7.81	7.04	1.510	1.286
			20%	9.04	8.66	8.50	0.97	0.108	18.96	7.77	11.19	2.650	2.874
			10%	9.02	8.66	8.50	0.87	0.097	19.11	7.87	11.24	1.720	2.580
		Tapered	80%	10.62	10.30	9.58	1.21	0.114	16.56	8.84	7.72	2.160	1.220
			20%	10.20	9.77	9.58	1.10	0.108	21.24	8.66	12.58	3.710	2.781
			10%	10.17	9.77	9.58	0.98	0.097	20.73	8.81	11.92	2.350	2.472
	Link 19	Notched	80%	15.46	15.20	13.16	1.81	0.117	23.73	12.19	11.54	4.930	0.837
			20%	14.04	13.54	13.16	1.31	0.094	26.66	12.05	14.61	5.040	2.231
			10%	13.92	13.46	13.16	1.24	0.089	24.90	11.97	12.93	5.030	2.658
		Rounded	80%	10.10	9.91	8.50	1.21	0.120	15.32	7.95	7.37	1.430	0.802
			20%	9.12	8.77	8.50	0.91	0.100	17.36	7.93	9.43	1.680	2.234
			10%	9.03	8.71	8.50	0.86	0.095	16.17	7.79	8.38	1.660	2.649
		Tapered	80%	11.46	11.26	9.58	1.39	0.122	17.50	8.90	8.60	1.890	0.701
			20%	10.29	9.90	9.58	1.02	0.099	18.86	8.90	9.96	2.280	2.132
			10%	10.19	9.83	9.58	0.97	0.095	17.76	8.74	9.02	2.310	2.561

Table 5. Statistical Properties of the von Mises Stresses Obtained for PM Peak Traffic.

Period	Link	Dapped Type	Truck Traffic Percentages	Average	Median	Mode	Standard Deviation	Coefficient of Variation	Maximum	Minimum	Range	Skewness	Skewness Coefficient
PM Peak Traffic	Link 13	Notched	80%	15.18	14.91	13.16	1.72	0.114	23.77	11.85	11.92	5.380	1.052
			20%	11.22	11.02	9.58	1.33	0.119	17.27	8.67	8.60	2.100	0.891
			10%	9.92	9.73	8.50	1.18	0.119	15.28	7.78	7.50	1.740	1.050
		Rounded	80%	13.81	13.45	13.16	1.06	0.077	23.09	12.08	11.01	3.160	2.662
			20%	10.10	9.82	9.58	0.82	0.081	16.51	8.83	7.68	1.420	2.566
			10%	8.96	8.70	8.50	0.73	0.082	14.93	7.82	7.11	1.030	2.644
		Tapered	80%	13.93	13.48	13.16	1.22	0.087	25.07	12.12	12.95	4.460	2.484
			20%	10.20	9.85	9.58	0.94	0.093	18.30	8.79	9.51	2.000	2.374
			10%	9.04	8.73	8.50	0.84	0.093	16.12	7.85	8.27	1.470	2.470
	Link 19	Notched	80%	15.45	15.18	13.16	1.77	0.115	23.46	12.16	11.30	4.870	0.872
			20%	11.45	11.26	9.58	1.37	0.120	16.82	8.83	7.99	1.840	0.713
			10%	10.09	9.90	8.50	1.21	0.120	15.13	7.87	7.26	1.550	0.872
		Rounded	80%	13.89	13.52	13.16	1.11	0.080	25.37	12.14	13.23	3.680	2.687
			20%	10.17	9.88	9.58	0.86	0.085	18.08	8.92	9.16	1.670	2.593
			10%	9.01	8.75	8.50	0.77	0.085	16.51	7.88	8.63	1.210	2.700
		Tapered	80%	14.04	13.60	13.16	1.25	0.089	26.15	12.15	14.00	4.420	2.262
			20%	10.29	9.95	9.59	0.97	0.095	18.62	8.92	9.70	1.980	2.154
			10%	9.12	8.81	8.50	0.86	0.095	17.01	7.93	9.08	1.470	2.284

Findley's parameter values were calculated from the 54 available stress histories. Without a correlation to experimental fatigue data, the calculated Findley's parameters cannot predict fatigue lives or number of cycles to failure. However, a relative comparison among the magnitudes of the scalar Findley's parameter indicates which stress histories are more damaging. Higher Findley's parameter values mean fewer cycles to initiation of a fatigue crack. The calculated Findley's parameter values for a stress concentration region were averaged and are shown in Figures 25 and 26. As with the stress histories, the Findley's parameters are distinguished by dap type, traffic period, truck traffic percentage, and CORSIM link location. Figure 27 is a color contour plot of the axial stress, σ_{xx}, in the web plate of the notched specimen. The severe local zones of stress concentration are clearly visible at the reentrant corner of the notch and at the end of the extended flange plate.

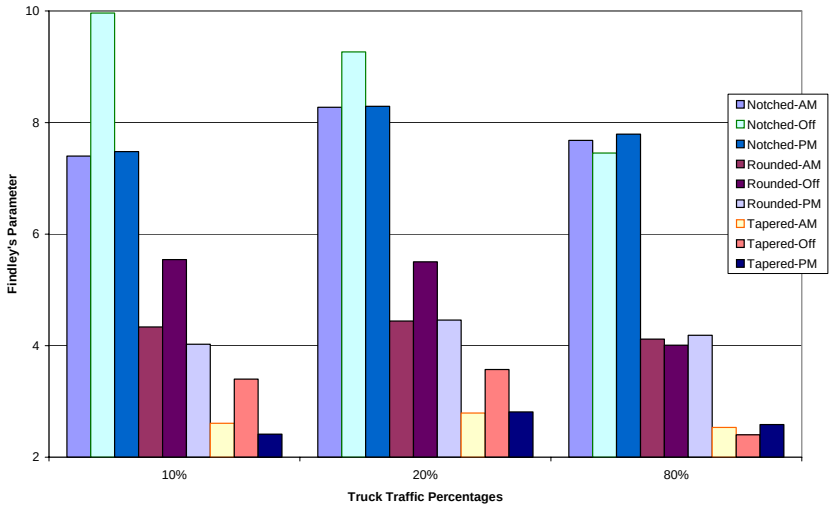

Figure 25. Fatigue Analysis Results for CORSIM Traffic Correlated to Link 13.

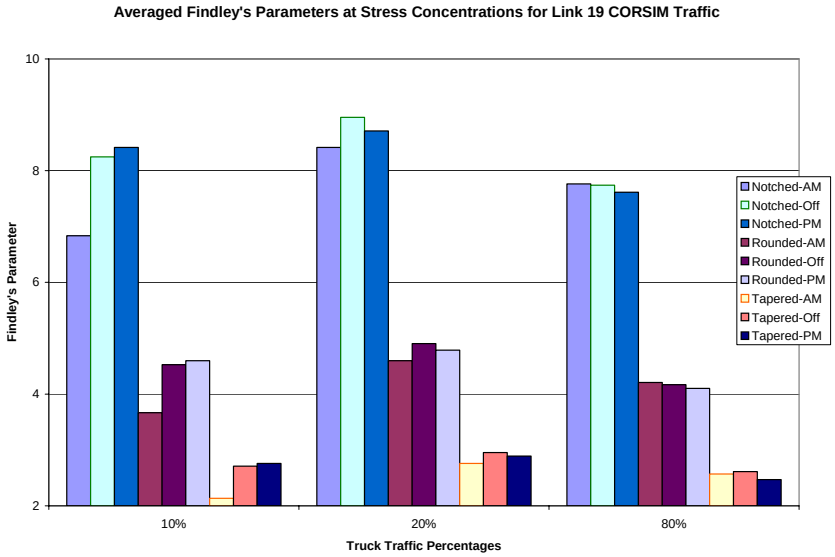

Figure 26. Fatigue Analysis Results for CORSIM Traffic Correlated to Link 19.

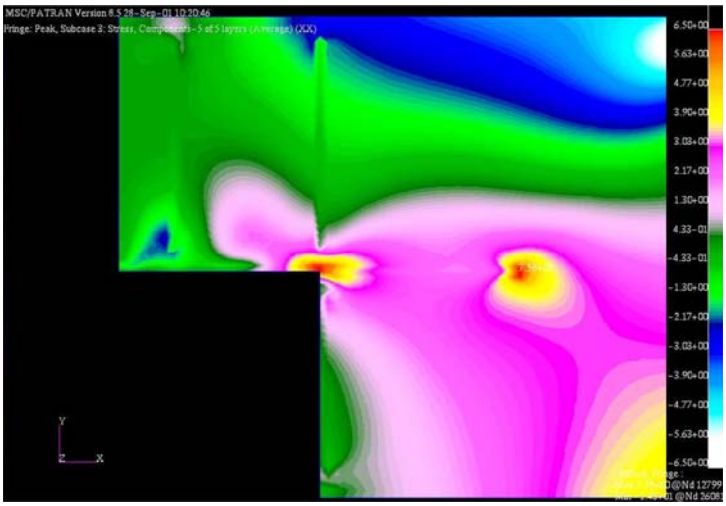

Figure 27. σ_{xx} Stress Contour Plot for Web Plate of Notched Detail.

The first and most obvious result of the stress history statistics shown in Figures 22 to 24 and Tables 3 through 5 is that, for the same traffic conditions, the notched dapped girder has the highest average von Mises stress of the three dapped types. The tapered dapped girder had the next highest, while the rounded dapped girder had the lowest of the three. This is a consequence of the level of stress concentration present in each dapped type. The reentrant corner of the notched dapped girder, coupled with the additional stress of contact with the horizontal forked plate, creates a substantially higher stress concentration. A geometrical stress concentration exists in the tapered dapped girder at both of the "bends" that begin and end the tapered portion. Placing a stiffener directly at the bend produces a larger stress concentration than if the two features occurred at separate locations. The higher average value of von Mises stress in the second bend of the taper may also be the result of higher bending moment at that location than nearer the support.

The stress histories with the highest range of stresses vary depending on which peak traffic period is examined. For AM peak traffic, 20 percent truck traffic produced the highest ranges for all dapped types and both links. For off-peak traffic, 10 percent truck traffic produced the highest ranges for all dapped types and both links. For PM peak traffic, 80 percent truck traffic produced the highest ranges for all dapped types and both links. The stress ranges are obviously controlled by the types of loads applied to the bridge; therefore, the daily variation of traffic composition and volume seem to play the greatest role in affecting the von Mises stress ranges.

All stress histories have a positive skewness and skewness coefficient, indicating that the dispersion of stresses is more above the mean. For AM and off-peak, the 80 percent truck traffic histories have the smallest skewness coefficient. This most likely indicates that when a large number of heavy loads are on the bridge, the stresses do not vary as much from the mean. This situation is analogous to the difference between loading alternate spans and loading all spans in a continuous beam. Often, to get the "worst case" scenario in a continuous beam, it is necessary to load alternate spans and not simply place a uniform load across all spans. The 80 percent truck traffic is similar to a uniform load on all spans, whereas the 10 and 20 percent truck traffic are similar to loading alternate spans. This underscores the need for accurate traffic percentages when determining stress levels. Simply assuming a large, unrealistic, uniform load may not yield the most significant structural effects, especially in terms of fatigue and accurately determining stress ranges. The differences between heavy and light volume traffic links (link 19 and link 13, respectively) were not substantial in the stress histories examined. Variations of less than 1 ksi average stress were seen between the links when all other conditions were the same.

Figures 25 and 26 present results for the Findley's parameters calculated in this study. These charts make it obvious that the notched detail experienced the highest values for Findley's parameter and the tapered detail experienced the smallest values. It is also interesting to note that while the tapered detail had a higher average von Mises stress than the rounded detail, the Findley's parameters for the tapered detail were still lower than those of the rounded detail. This is a consequence of the way in which Findley's parameter is calculated (see Equation 3). A large variation of shear stress on a critical plane causes more fatigue damage than a high mean stress level that does not fluctuate. This fact seems to imply that the round girder would have more fatigue problems than the tapered girder.

For link 13, as shown in Figure 25, with 10 or 20 percent truck traffic, the off-peak period had substantially higher Findley's parameters for all details. This observation acknowledges the more damaging effect of a lighter volume of traffic with its associated larger range of stress. During AM or PM peak periods, heavy traffic volume loads the three-span bridge more or less evenly. This loading has the effect of "balancing" the stresses and creating a lower overall stress condition. Higher loading on one span corresponds to the analogy of loading alternate spans. In a lower volume link, with fewer trucks, and in an off-peak period, the chances of having a large difference in span loading are much greater. This phenomenon seems to be verified by Figure 26.

Link 19 is a higher volume link, and Findley's parameters for the details are very similar regardless of peak period or truck traffic percentages.

FATIGUE TESTS

Experimental Procedures

One of the outcomes from the fatigue analysis procedure was a finding that because of the proximity of the dapped detail to the girder support, it is the reaction force at the support that primarily determines the state of stress at critical locations within the dapped region (*1*). Stated another way, under service loading, critical stresses in the dapped region are proportional to the support reaction. This is true even for the critical zone in the tapered flange bend farther from the support. Consequently, very accurate full-scale fatigue tests of the dapped details are easily accomplished by loading the dapped end of a relatively short girder specimen with a correct history of service load reaction values. Figure 28 shows a free body diagram for the test setup used in this project. The dapped end is located at reaction point number 1, and two actuators load the specimen.

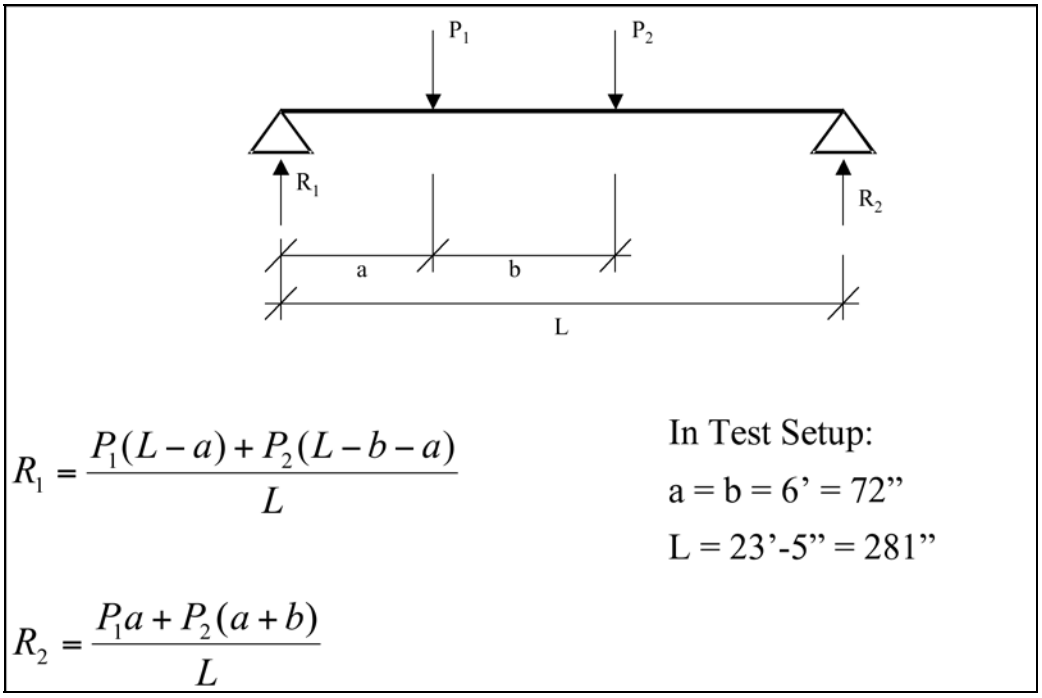

Figure 28. Free Body Diagram for Fatigue Test Setup: Dapped End Located at R_1.

In this project, the reaction histories from the 54 fatigue analysis simulations described above were used to determine the load histories for the fatigue experiments. One must keep in mind, however, that a specimen subjected to the complete simulated reaction history would survive for many years of continuous testing before developing a fatigue crack. In order to accomplish a meaningful program of fatigue tests within the time frame and budget of this project, the reaction histories had to be abbreviated. This was accomplished by removing a certain portion of the small stress range cycles from the simulated histories.

Cycle counting reduces a complex variable amplitude history into a number of constant amplitude events (*15*). A cycle counting method, called rainflow counting, was used in this study to aid in creating the abbreviated loading fatigue tests. Since the reactions at the dapped end controlled the experiments, the rainflow analysis was performed on a reaction history rather than a stress history. However, since both types of histories are available, the Fortran program reorganized the stress histories in exactly the same fashion as their corresponding reactions. In this way, reaction cycles that produce the largest stress ranges can be identified.

Stress and reaction histories used in the experimental fatigue testing were selected from CORSIM link 13 with 20 percent truck traffic. For each hour-long period of AM peak, off-peak, and PM peak traffic, the reaction cycles that produced the four highest von Mises stress ranges were selected and placed in a set. These critical sets of reaction histories from the three simulation periods were combined to define a "worst-of-the-day" reaction loading block for the fatigue tests. The "worst-of-the-day" loading block comprised one set of AM peak cycles, nine sets of off-peak cycles, one set of PM peak cycles, and, finally, 13 sets of off-peak cycles to represent a greatly abbreviated 24-hour day.

Because these stress histories are variable amplitude rather than constant amplitude, over the long term, the phenomenon of a *fatigue limit* (i.e., stress range below which there is infinite fatigue life) is not manifest in this problem. Therefore, the damaged caused by many thousands of small stress range cycles in a real day is not reflected in this testing program. Nevertheless, the loading blocks that are applied represent realistic cycles that dapped details likely encounter in service. Specifically, they reflect the daily worst-case cycles from the case-study bridge under simulated traffic. Hence, the abbreviated-day loading block is less severe than a full actual day in terms of total accumulation of fatigue damage. It is not correct to say, therefore, that the abbreviated-day loading block is equivalent to a real day of traffic.

For each of the case-study details (i.e., tapered, rounded, and notched) I-shaped, bare-steel specimens were fabricated using A709-50W steel, according to drawings approved by TxDOT. The specimens were 281 in. long and 62 in. deep with 1.25-in. by 18-in. flange plates and 0.5-in. web plates. The specimens were fabricated by Trinity Industries of Houston, Texas. Figure 29 shows a photograph of the three specimens on the laboratory floor prior to testing.

Figure 29. Photograph of Tapered, Rounded, and Notched Fatigue Test Specimens.

During fatigue testing, the dapped end of each specimen rested on a bearing pad, and the other end of the specimen was simply supported. As indicated in Figure 28, two actuators loaded the specimen. The actuator controllers were programmed under load control to generate the desired support reaction history at the dapped end as the input fatigue load for the specimen. Figures 30 and 31 show plan and elevation views of the test setup. Figure 32 shows a photograph of the notched specimen as it was being installed in the test setup. The 110- and 220-kip actuators are visible in Figure 32. A 9-ft header beam, connected to two columns, supported the dapped end of the specimen.

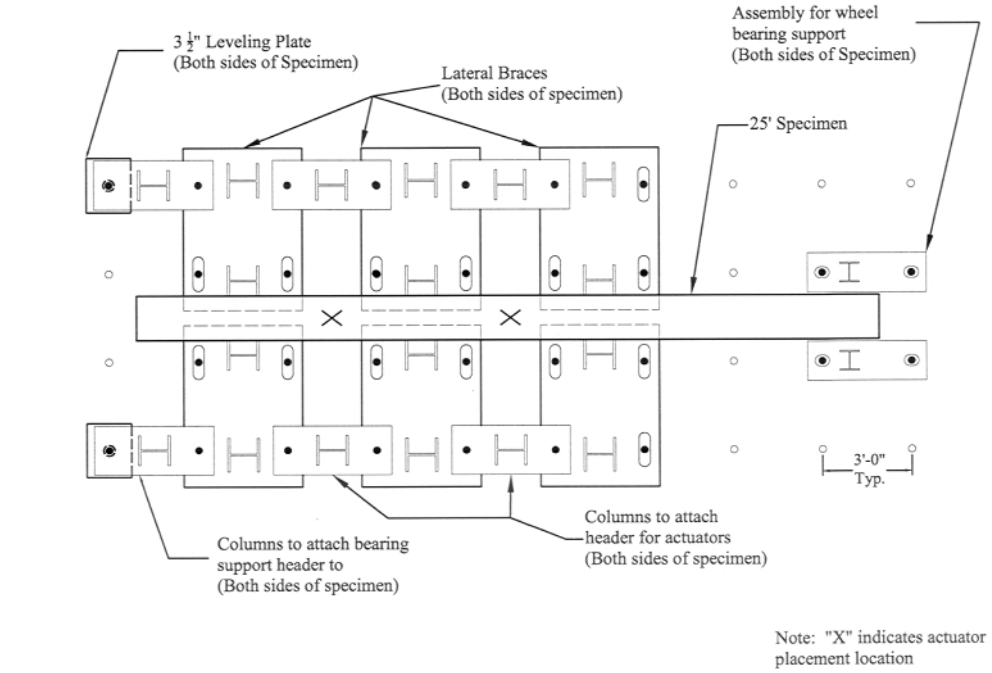

Figure 30. Plan View of the Experimental Setup.

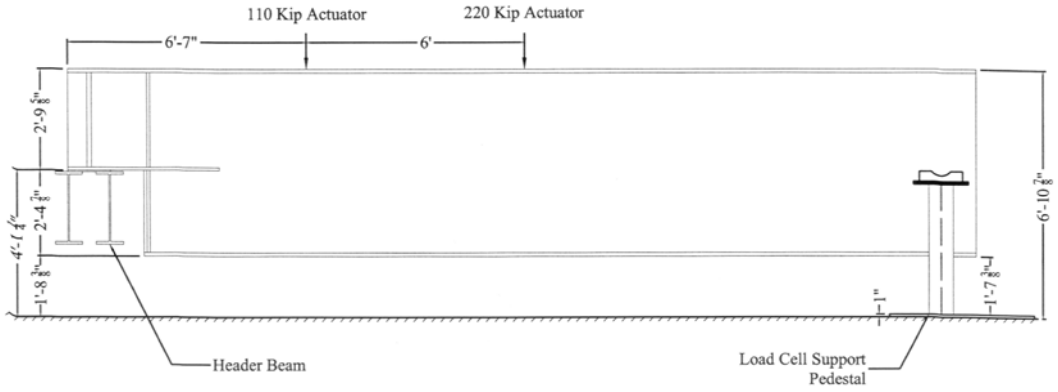

Figure 31. Elevation View of the Experimental Setup.

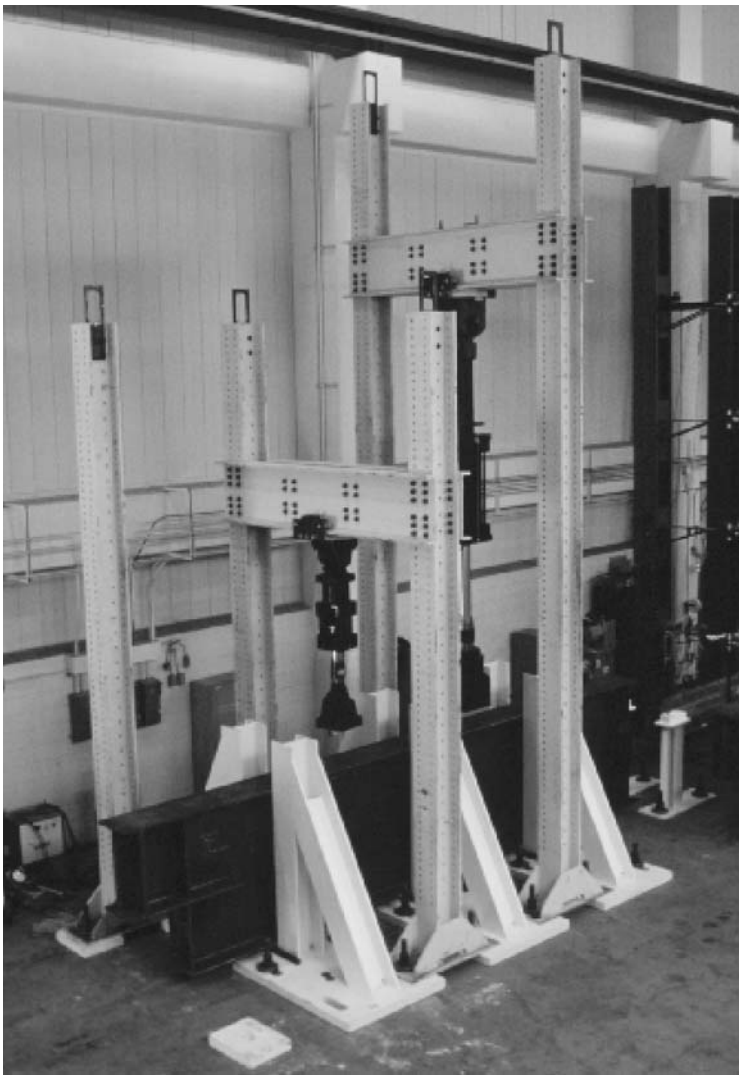

Figure 32. Photograph of Fatigue Test Specimen during Installation.

After each specimen was installed, and prior to fatigue testing, a series of small-load static tests verified the behavior of the test setup. During the static testing, a cylindrical roller-bearing load cell was bolted to the WT shapes that are welded to the stiffeners on the end of each specimen (see Figure 33). A pedestal fabricated from a W shape welded to steel plates on both ends supported the load cell. During fatigue testing, the roller-bearing load cell was removed, and a roller support attached to the laboratory floor (see Figure 34) was used underneath the specimen. This switch was necessary because the roller-bearing load cell was not designed to resist fatigue loading. In addition to the two load cell support pedestals, six lateral braces were fabricated for use in testing. The lateral braces were arranged as shown in Figures 30 and 32 to prevent lateral walking of the specimen during the pulsating load test.

Figure 33. Photograph of WT Shape Welded to Stiffeners at End of Specimens.

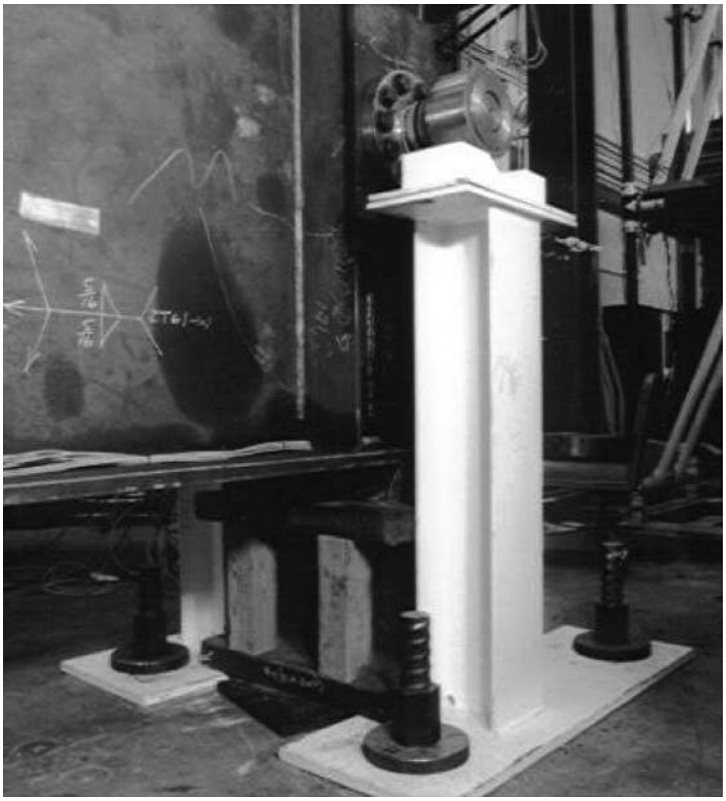

Figure 34. Photograph of Support for Full Height End of Specimen.

The load cell on the support pedestal was used to measure the reaction at the full height end of the specimen. Using this information, along with the known applied actuator loads, the reaction at the dapped end can be calculated. By using the free body diagram and resulting equations with values shown in Figure 28, the expected reaction in the load cells, R_2, can also be calculated based on the loads in the actuators. Table 6 shows the sets of actuator values used in the static tests.

Table 6. Actuator Values Applied during Static Testing.

	Actuators			Actuators	
Reading	100k	200k	Reading	100k	200k
1	10.0	0.0	16	0.0	70.0
2	20.0	0.0	17	0.0	80.0
3	30.0	0.0	18	0.0	90.0
4	40.0	0.0	19	0.0	100.0
5	50.0	0.0	20	0.0	110.0
6	60.0	0.0	21	0.0	120.0
7	70.0	0.0	22	10.0	120.0
8	80.0	0.0	23	20.0	120.0
9	90.0	0.0	24	30.0	120.0
10	0.0	10.0	25	40.0	120.0
11	0.0	20.0	26	50.0	120.0
12	0.0	30.0	27	60.0	120.0
13	0.0	40.0	28	70.0	120.0
14	0.0	50.0	29	80.0	120.0
15	0.0	60.0	30	90.0	120.0

During the fatigue tests, the two actuators were driven by the controllers under load control programming. The reaction histories determined from the rainflow analysis, described previously, were used to define actuator load values necessary to simulate the abbreviated-day fatigue loading block. Refer to Figure 28 for the free body diagram used to determine actuator load values for given required reaction values. To maximize the cycle application rate, the larger and slower 200-kip actuator was held to a constant load, and the smaller, faster 100-kip actuator imposed the load variations. Table 7 shows the values determined in the rainflow analysis procedure and used in the fatigue testing. In Table 7, the off-peak set is shown only once. During testing, however, the full abbreviated-day loading block comprised one AM peak set followed by nine off-peak sets, followed by one PM peak set, and then concluded with 13 off-peak sets. With

this test setup, the full abbreviated-day loading block could be repeated approximately every 45 seconds.

Table 7. Sequence of Total Reaction and Individual Actuator Values for the Load Block Sets.

Period	Reaction	100 Kip	200 Kip
AM Peak	58.0	0.0	119.0
	93.6	47.8	119.0
	76.8	25.2	119.0
	90.3	43.4	119.0
	58.0	0.0	119.0
	91.5	45.0	119.0
	87.0	39.0	119.0
	104.8	62.9	119.0
Off Peak	69.2	15.0	119.0
	128.9	95.3	119.0
	106.4	65.0	119.0
	115.6	77.4	119.0
	94.2	48.7	119.0
	131.7	99.0	119.0
	58.0	0.0	119.0
	90.7	44.0	119.0
PM Peak	58.0	0.0	119.0
	91.5	45.0	119.0
	58.0	0.0	119.0
	85.9	37.5	119.0
	91.9	45.5	119.0
	104.8	62.9	119.0
	66.9	12.0	119.0
	109.1	68.7	119.0

Experimental Results

Summary of Static Test Results

The calibrated load cells on the full height end of the specimen recorded the reaction at that end. By using the equations of Figure 28 for R_2, the expected reaction at the full height end can be calculated and compared to experimental results. Figure 35 and Table 8 show the comparison of expected reaction values to those measured during static testing. The three different series in Figure 35 refer to the readings shown in Tables 6 and 8.

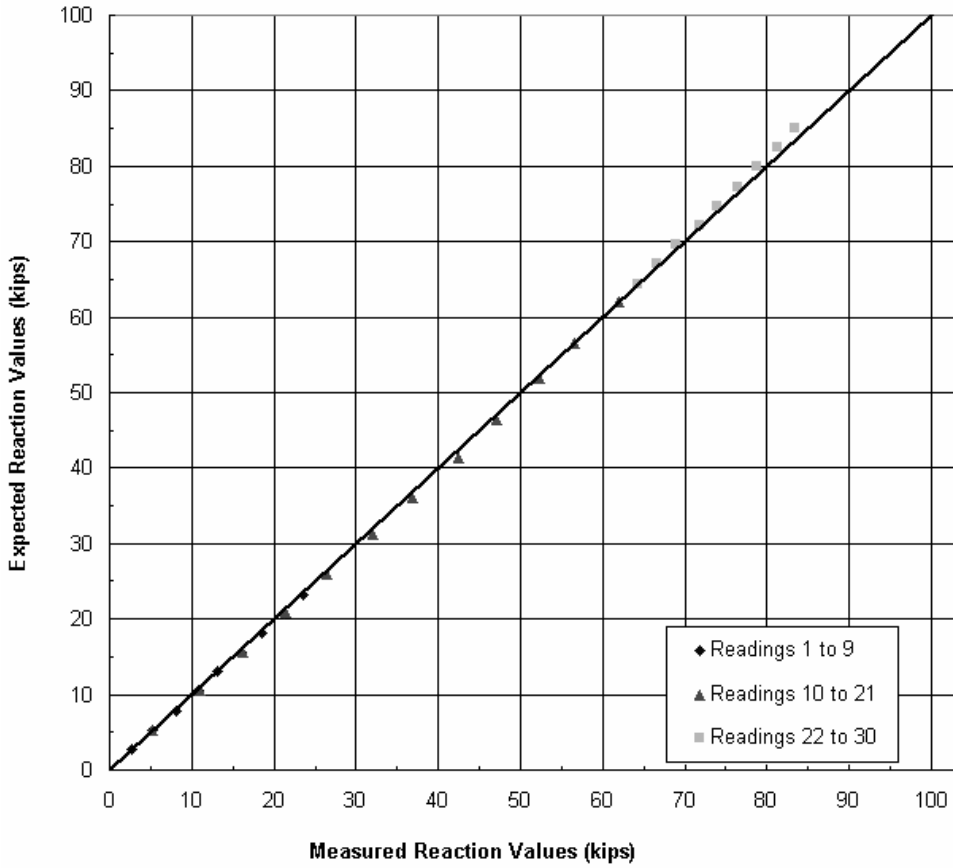

Figure 35. Comparison of Expected and Measured Reaction Values.

Table 8. Comparison of Experimental and Analytical Results.

	Measured			Expected			
	Load Cell 1	Load Cell 2	Load Cell	Full Height End	Dapped End	Actuators	
Reading	(kips)	(kips)	Total (kips)	R_1 (kips)	R_2 (kips)	100k	200k
1	1.32	1.39	2.71	2.82	7.78	10.20	0.40
2	2.53	2.72	5.25	5.34	15.05	19.94	0.45
3	3.91	4.10	8.02	7.88	22.51	30.03	0.36
4	5.14	5.59	10.73	10.49	30.10	40.23	0.36
5	6.26	6.85	13.11	13.01	37.39	50.03	0.37
6	7.59	8.40	15.99	15.56	44.92	60.24	0.25
7	8.87	9.63	18.50	18.18	52.40	70.21	0.36
8	10.17	11.01	21.18	20.73	59.91	80.37	0.27
9	11.32	12.27	23.59	23.30	67.39	90.46	0.24
10	2.46	2.85	5.31	5.18	5.07	0.27	9.98
11	5.13	5.80	10.93	10.65	10.27	0.27	20.65
12	7.65	8.49	16.13	15.69	15.07	0.27	30.49
13	10.03	11.31	21.34	20.91	20.02	0.26	40.67
14	12.44	13.97	26.41	25.91	24.78	0.27	50.42
15	15.05	17.07	32.12	31.32	29.93	0.27	60.98
16	17.29	19.62	36.91	36.12	34.51	0.28	70.36
17	19.67	22.77	42.43	41.45	39.56	0.25	80.76
18	21.69	25.50	47.19	46.37	44.27	0.32	90.33
19	23.94	28.40	52.35	51.82	49.48	0.36	100.95
20	25.79	30.81	56.60	56.57	53.99	0.34	110.22
21	28.08	33.82	61.91	61.93	59.09	0.35	120.67
22	29.19	35.08	64.27	64.44	66.40	10.18	120.66
23	30.23	36.33	66.56	67.01	73.83	20.17	120.67
24	31.32	37.53	68.85	69.53	81.15	29.99	120.69
25	32.62	39.13	71.76	72.22	88.93	40.43	120.72
26	33.68	40.34	74.02	74.70	96.12	50.09	120.72
27	34.81	41.66	76.47	77.31	103.63	60.15	120.79
28	35.84	43.00	78.83	79.88	111.11	70.23	120.77
29	36.88	44.37	81.25	82.43	118.69	80.54	120.58
30	37.83	45.61	83.44	85.00	126.15	90.56	120.59

Summary of Fatigue Test Results

Referring to Figures 25 and 26, it is clear that the notched detail is expected to display the worst fatigue performance among the three considered in this study. In fact, the fatigue sensitivity of the notched detail, as measured by Findley's parameter, appears to be roughly twice that of the rounded detail and triple that of the tapered detail. Similar to the traditional S-N curve for uniaxial stress ranges, a correlation between fatigue life and Findley's parameter involves a power law relationship. For illustrative purposes it is reasonable to assume an exponent value of -3 for structural steel. Such a correlation implies that the expected fatigue life for the rounded detail is 8 times the notched detail. The tapered detail might be expected to survive 27 times as long as the notched detail. The fatigue testing program in this project was

designed with due consideration of this issue. Researchers decided to test the notched specimen first and halt the test at the first appearance of a fatigue crack, followed by testing of the other two specimens until they developed a fatigue crack or until they surpassed the benchmark fatigue life of the notched specimen, whichever came first.

Following this procedure, the fatigue test of the notched specimen commenced first and was halted after application of approximately 126,000 abbreviated-day load blocks. At that time a small fatigue crack was discovered in the web plate of the specimen at the toe of a weld at the end of the extended horizontal flange plate. Referring to Figure 27, this location for a crack is in line with expectations from analysis.

The tapered detail was tested second and did not develop a fatigue crack before reaching the benchmark of approximately 126,000 abbreviated-day load blocks. At that time the test was halted.

The rounded detail was tested last and did not develop a fatigue crack before reaching the benchmark of approximately 126,000 abbreviated-day load blocks. At that time the test was halted.

All three fatigue specimens were retained and are stored at the Texas Transportation Institute proving ground facility at the Texas A&M University Riverside Campus in Bryan, Texas.

CHAPTER 4:
ULTIMATE STRENGTH BEHAVIOR OF DAPPED GIRDER DETAILS

CHAPTER OVERVIEW

As described in this chapter, the static ultimate strength behavior of dapped girder end details was examined utilizing a series of three-dimensional finite-element models. The models accommodated material and geometric nonlinearity so that the behavior of the girders could be assessed analytically under ultimate load conditions. (The details of the initial set of analyses can be found in the master's thesis of a coauthor of this report [*16*].) Based upon the results from the initial set of models, three specimens for laboratory testing were designed. Finite element analyses of the tests were completed so that a set of analytical predictions from this study could be directly compared with experimental results. Based upon the experimental results, further analyses of several variations of the test specimens were conducted under static ultimate load conditions and static service load conditions.

ULTIMATE STRENGTH ANALYSIS PART I: GENERAL BEHAVIOR

Procedures

The first phase of the ultimate strength investigation focused on analytically assessing the shear capacity of dapped ended steel plate girders using the finite element method. Two different dapped details, with dimensions and web geometry most suited for highway applications, were selected for this study: the tapered detail and the 90-degree rounded detail. A model of a tapered web detail is shown in Figure 36, and a model of a 90-degree rounded detail is shown in Figure 37.

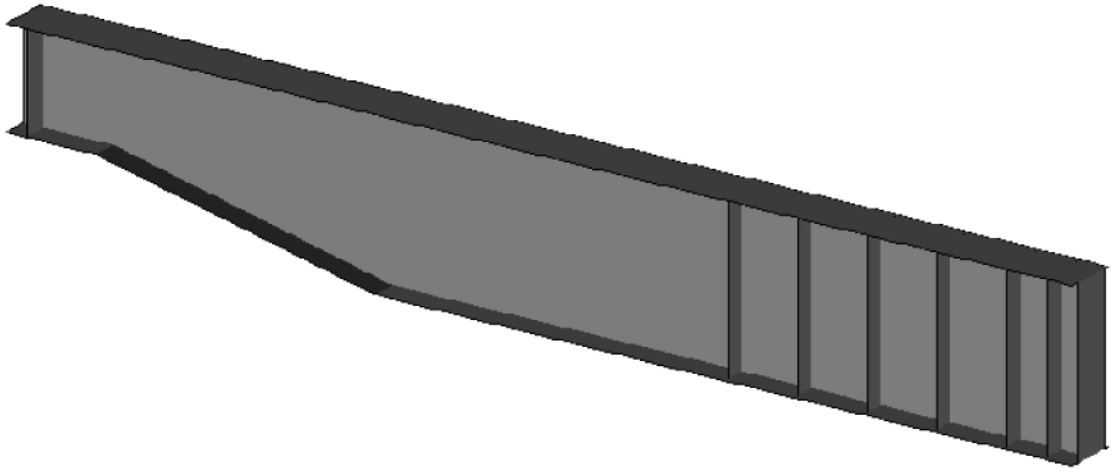

Figure 36. Illustration of the Tapered Web Plate Girder Geometry Used in This Study.

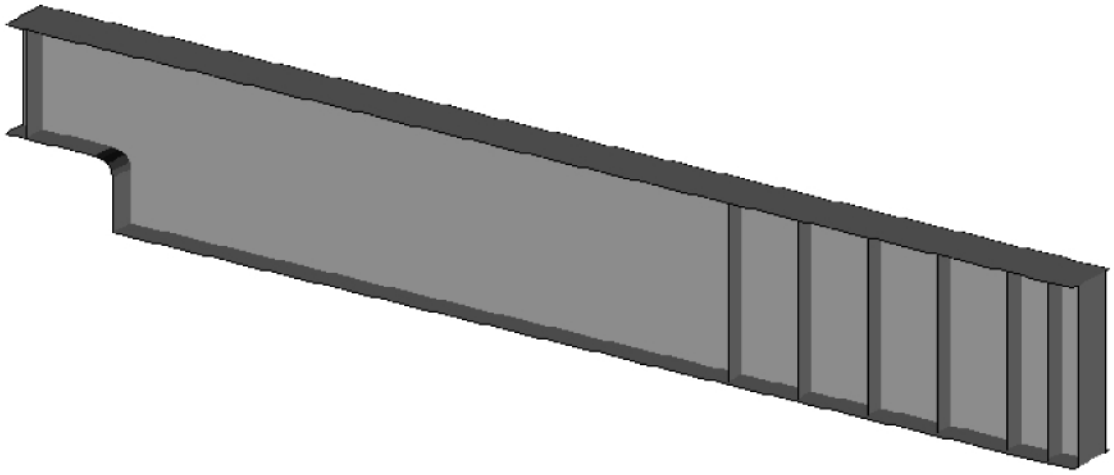

Figure 37. Illustration of the Rounded Girder Geometry Used in This Study.

Dapped girder ends are installed at terminal support locations, usually simple supports, and, consequently, they resist the maximal shear forces and minimal bending moments of the span. Hence, shear force capacity is a primary consideration when designing the dapped region. For that reason the initial set of analyses focuses on investigating the shear capacity of dapped details.

One specific objective of the analyses is to investigate the ability of dapped details to resist shear force as "unstiffened" end panels. The geometry of the finite-element models used in this study is shown in Figures 36 and 37. Each specimen is loaded at the dapped end and supported at the opposite end as a cantilever. As seen in Figures 36 and 37, the models include a bearing stiffener at the dapped end support and then a long open shear panel. The next stiffener

pair is located where the first cross-frame would be installed in a real structure. Beyond the cross-frame stiffener pair, a generous length of beam separates the test panel of the specimen from the artificial cantilever support boundary conditions imposed at the end of the specimen. This so-called "insulator" segment is heavily stiffened so that it will not "fail" in shear before the test panel, which would be a concern because of bending moment-shear force interaction effects.

In selecting girder configurations to be analyzed, realistic dimensions based on field applications were given priority. Figures 38 and 39 show the geometric parameters needed to describe the web plate of a dapped girder end for the tapered and rounded configurations, respectively. The decision was made to examine three different dapped detail geometries; these geometries consisted of two tapered girders and one rounded girder. The parameters described below were held constant for all three geometries except for the values of the parameter θ.

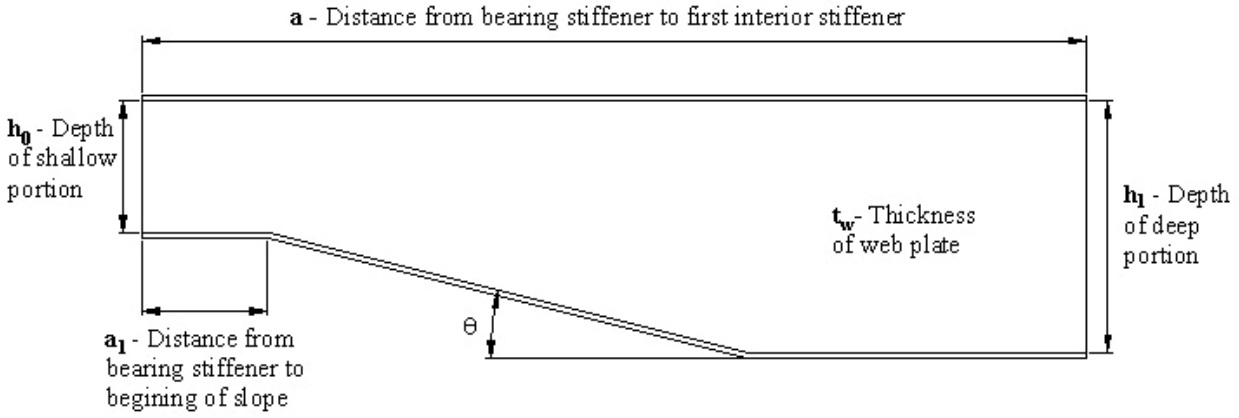

Figure 38. Geometric Parameters for a Tapered Detail.

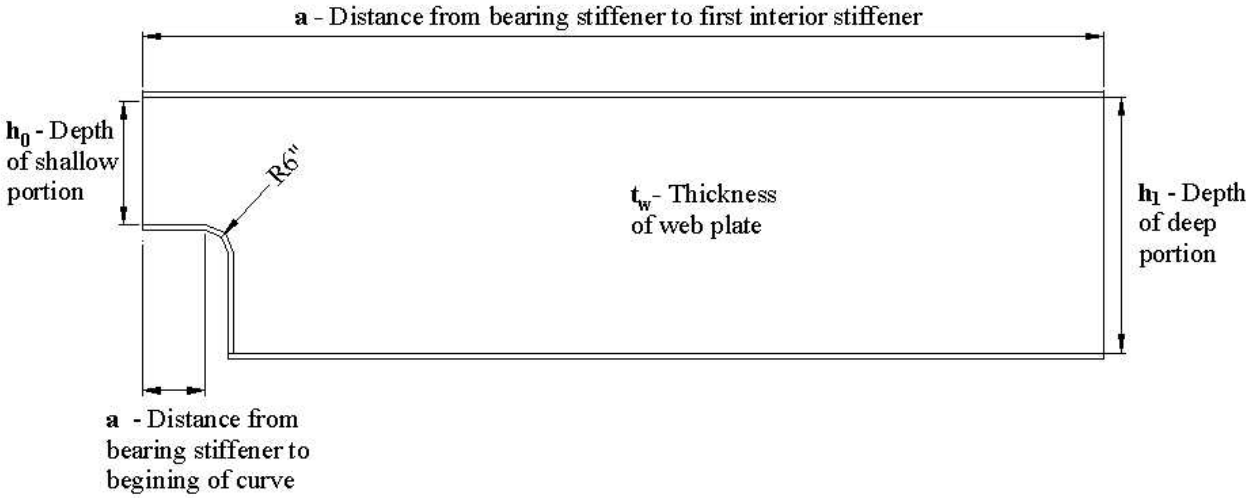

Figure 39. Geometric Parameters for a Rounded Detail.

The parameter values selected for the initial analysis cases are explained in the following:

- Geometric Parameter **a** – This parameter was taken as 20 ft. This magnitude was deemed to be a reasonable estimate of the distance between the bearing stiffener and the first interior diaphragm for many bridges.
- Geometric Parameter $\mathbf{a_1}$ – This parameter is controlled by the dimensions of the bent cap on which the girder rests. The value of this parameter does not vary significantly among bridge structures. Accordingly, a value of 24 in. was maintained for all cases.
- Geometric Parameter $\mathbf{t_w}$ – A web thickness of 0.25 in. was selected to provide a thin web. The thin web was selected to ensure that the test panel would "fail" in shear.
- Geometric Parameter $\mathbf{h_0}$ – This parameter is often controlled by the depth of an adjacent precast concrete girder. Accordingly, the value chosen was 36 in. to match the depth of the AASHTO type IV standard I-girder.
- Geometric Parameter $\mathbf{h_1}$ – This parameter can vary from approximately 4 ft to 10 ft. A value of 5 ft was chosen for this project.
- Geometric Parameter $\boldsymbol{\theta}$ – This parameter was given values for three common cases: a 1:1 slope and a 1:4 slope for the tapered detail and a 6-in. radius for the 90-degree rounded detail.

Once these parameters were set, the analysis could begin. The Texas A&M University Supercomputer Facility was used to complete all of the analyses. The supercomputers run many jobs simultaneously and provide the memory and storage necessary to accommodate the large

files that were created. Patran 8.5 and ABAQUS 5.8 generated and solved the finite-element models in this study (*2*, *3*).

The loads and boundary conditions for the models are shown in Figure 40. The reaction force was represented by loads applied to the nodes on the bottom flange directly below the bearing stiffeners. Lateral support was provided where diaphragms frame into the transverse stiffeners. In an actual structure, the composite concrete slab would provide continuous lateral support of the top flange. It is easy to "over-restrain" analytical models such as these, which is a mistake that can lead to unconservative conclusions. By the same token, under-restraint can lead to uneconomical conclusions. To address the issue of lateral restraint, two baseline cases were analyzed: a fully supported compression flange case and a case with support provided at discreet points. The load for these two cases differed by less than 1 percent (*16*). Therefore, all subsequent cases were run with lateral support provided only at locations where diaphragms would normally be installed.

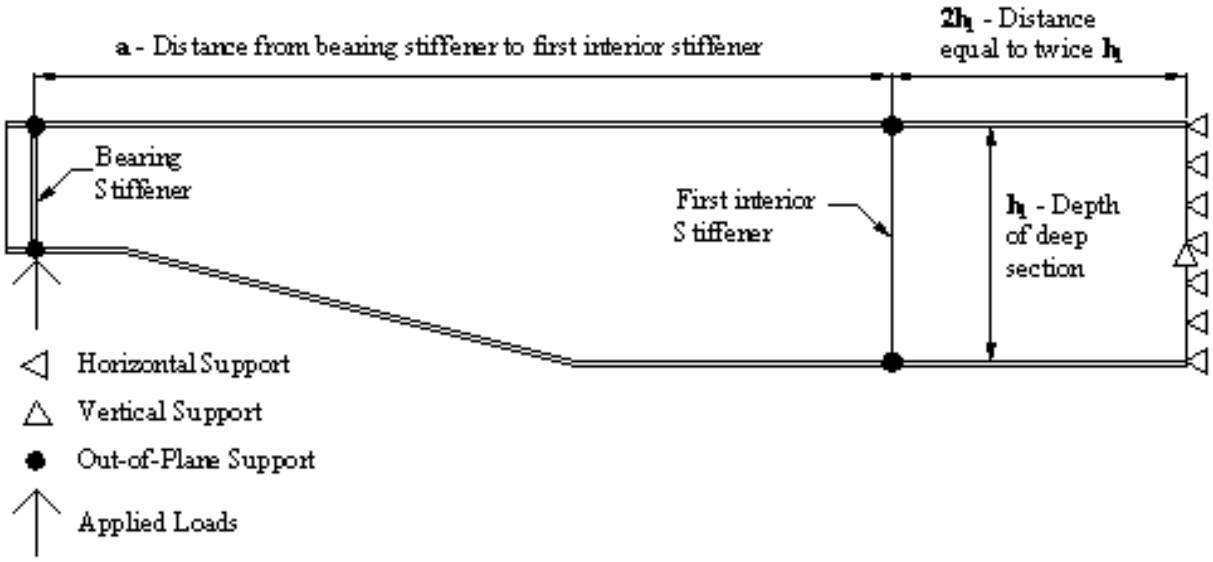

Figure 40. Load and Boundary Conditions Applied to the Girders.

The baseline case was helpful in selecting the type of finite element to use in the models. These analyses showed that linear solid elements give unpredictable results; therefore, quadratic elements were needed. Researchers chose quadratic shell elements over quadratic solid elements because they have the advantage of dramatically reducing computational effort. Another consideration is that the thickness of the web plate of a plate girder is very small in comparison

to the largest dimension of the model which would necessitate an exceedingly poor aspect ratio with solid elements. Therefore, even though shell elements ignore through-thickness shear stresses, which are available to solid elements, quadratic shell elements were the most logical choice for use in these models. A convergence study using the baseline case showed that quadratic shell elements with a characteristic element length of 4 in. provided a model that converged to a solution.

Information about a specific model is contained within a Patran database. Databases have an associated journal file that contains every command necessary to create the database. This configuration allowed creation of Fortran programs to manipulate journal files. Patran can then build a new database by going through an altered journal file and executing each command.

Two template databases were created using the normal graphical interface available in Patran. One journal file corresponded to the web tapered style of dapped detail and the other to the rounded style of dapped detail. The journal files associated with these databases were used as templates to create journal files for all other cases.

A Fortran program called Journal.f was created to modify the web tapered template journal file for the creation of all web tapered cases. This program receives the name of the template journal file as well as geometric parameters $\mathbf{H_0}$, $\mathbf{H_1}$, θ, $\mathbf{a}$, and $\mathbf{t_w}$ as input and outputs a journal file with modified geometry. An analogous program called Rjournal.f was written to create all rounded cases. The parameter θ is omitted from Rjournal.f inputs, but the programs are otherwise identical.

Patran used modified journal files created in this manner to create new databases and ABAQUS input files for each geometry of interest. However, the modified journal files did not contain information about the applied loads or the support in the vertical direction. This omission occurs because geometric variations within the cases cause the number of related nodes to change as well. Each model had different dimensions and a different number of elements and nodes. The modified node numbering made it impossible to include the applied loads and vertical supports in the new journal file. Therefore, it was necessary to add these loads and boundary conditions to the ABAQUS input files. This addition was accomplished using another Fortran program, Lobocop.f, which uses geometric parameters $\mathbf{H_0}$ and $\mathbf{H_1}$ and panel width $\mathbf{A}$ as inputs and outputs the revised ABAQUS input file.

The program proceeds as follows. First, Lobocop.f searches the ABAQUS input file for all nodal coordinates. The program then determines which node, on the far end of the model, is nearest to the mid-depth of the girder and applies vertical support to this node. Lobocop.f then queries the node coordinates in order to find the nodes that lie under the bearing stiffener and applies the loads comprising the reaction to these nodes. Finally, Lobocop.f rewrites the ABAQUS input file with the new loads and boundary conditions.

At this point, it is possible to begin the finite element analyses. These analyses consist of a two-step process for each geometry of interest. First, a linear eigenvalue analysis is run; this analysis corresponds to an estimate of the critical buckling load for a perfect, bifurcating system. The results generated by ABAQUS are an eigenvalue and a mode shape. The eigenvalue corresponds to the linear estimate of the magnitude that the applied loads would have to be scaled in order to reach the critical buckling load. The mode shape is an estimate of the buckled shape, with a maximum displacement of unity.

However, in practice, a girder may experience relatively large displacements or yielding of the material prior to encountering a loss of stiffness. This case, known as inelastic buckling, deviates from our assumptions in the linear eigenvalue analysis. To account for inelastic buckling, as well as any post-buckling behavior, a nonlinear Riks analysis must also be performed.

A Riks analysis obtains nonlinear static equilibrium solutions for unstable problems. In a traditional nonlinear analysis, the load must always increase from increment to increment. This is not the case with the nonlinear Riks analysis. A Riks analysis treats both loads and displacements as unknowns, and these quantities may increase or decrease during the analysis. Since load is unknown, the arc length along the static equilibrium path is used to measure the progress of the solution. For a detailed discussion of Riks analysis as implemented in the ABAQUS program, see section 2.3.2 of the *ABAQUS Theory Manual* (*17*).

To perform the nonlinear Riks analysis, the mesh used for the eigenvalue analysis must be seeded with an imperfection. If no imperfection is present in the mesh, the system may never buckle under reasonable loads. The estimated buckled shape from the eigenvalue analysis is used to introduce a physically meaningful imperfection. The maximum allowable imperfection in plate girder webs is specified in the *AWS Bridge Welding Code* (*18*). These maximum values of

web imperfection were used in running the analyses. Additionally, analyses were performed using a small imperfection of just 10 percent of the web thickness.

A Fortran program called Nonlinear.f was written in order to create an ABAQUS input file for the nonlinear Riks analysis. The input for Nonlinear.f is described in the following:

- ABAQUS input file for linear eigenvalue analysis – This file is a template from which the input file for the nonlinear load displacement analysis was written.
- Initial, total, and maximum load proportionality factors – These factors increase the magnitude of the applied loads. The Riks analysis scales the applied loads up from unity to the maximum load proportionality factor over the course of the analysis. An exception to this occurs if ABAQUS runs out of analysis increments before reaching the maximum load. Nonlinear.f generates a file that allows the analysis to have 20 increments before the analysis ends.
- Magnitude of imperfection – This factor scales the buckled shaped from a value of unity to a maximum magnitude of the value entered.
- Mode shape for which displacements should be scaled – The analysis used the first mode shape that gave a positive eigenvalue. A negative eigenvalue corresponded to the case of buckling of the girder with a negative reaction. Since this case is nonphysical, all mode shapes with negative eigenvalues were ignored.

The input file for the linear eigenvalue buckling analysis is used as a template to create the input for the nonlinear Riks analysis. The template input was rewritten with all of the information necessary to complete the load displacement analysis. This system allows node and element numbering to remain constant between the linear eigenvalue and nonlinear Riks analyses, and the original Patran databases may be used for post-processing. In addition to adding the necessary information to perform a Riks analysis, the linear input file must also be altered to include nonlinear material properties. An elastic-perfectly plastic stress-strain relationship was used, with a yield stress of 50 ksi.

The Riks analysis produces large output files since output for each solution increment is written to the same file. A fourth Fortran program, called Output.f, was created to extract results from the output file. The names of the Riks analysis output file and the node of interest are input into Output.f, and load and displacement values for that node at each analysis increment are output.

Nodes that give insight into how the girder behaves were chosen. Load-displacement output was found for the node that lies at the juncture of the bottom flange, the web, and the bearing stiffeners. Additionally, displacements for the node in the web with the largest out-of-plane displacement from the buckled mode shape were found.

Results

The results of the linear eigenvalue analysis are the buckling mode shape and the linear estimate of the critical load. Figures 41 through 43 show the mode shapes for the 4:1 tapered girder, the 1:1 tapered girder, and the 90-degree rounded girder, respectively. These mode shapes are indicative of shear buckling. When a plate buckles in shear, it should take the shape of a half-sine wave in the tensile direction and at least one full sine wave in the compressive direction (*19*). The buckled webs of each of the three girders demonstrate this kind of behavior.

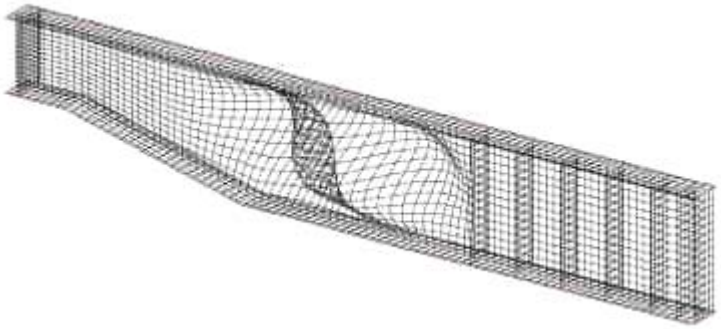

Figure 41. Buckling Mode Shape for the Tapered Girder with 4:1 Slope.

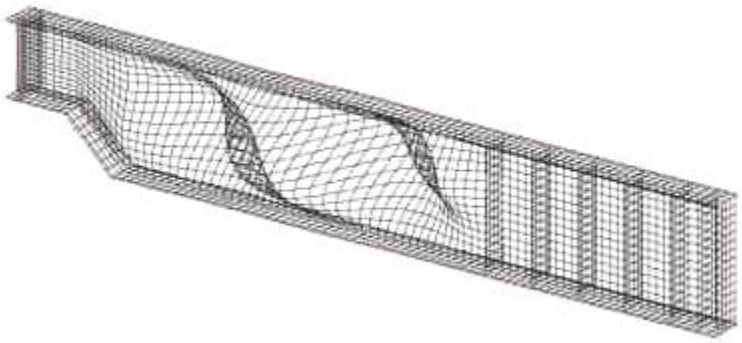

Figure 42. Buckling Mode Shape for the Tapered Girder with 1:1 Slope.

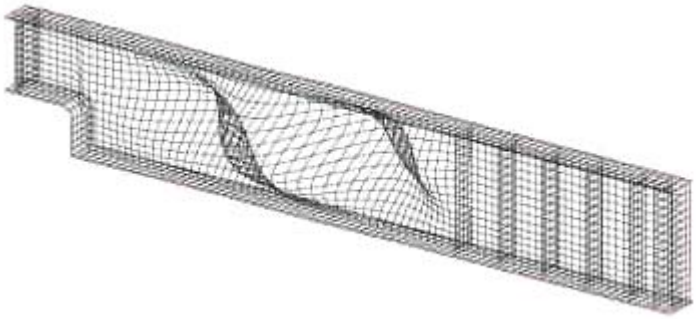

Figure 43. Buckling Mode Shape for the Round Girder.

Plots of load versus displacement were used to determine the ultimate capacity of the girders. Figures 44 and 45 show applied load versus displacement plots for the 4:1 tapered detail. Figure 44 includes an analysis for the girder using the maximum allowed imperfection, a small imperfection (10 percent of the web thickness), and no imperfection. Figure 45 shows only the portion of the plot for the analyses that included an imperfection.

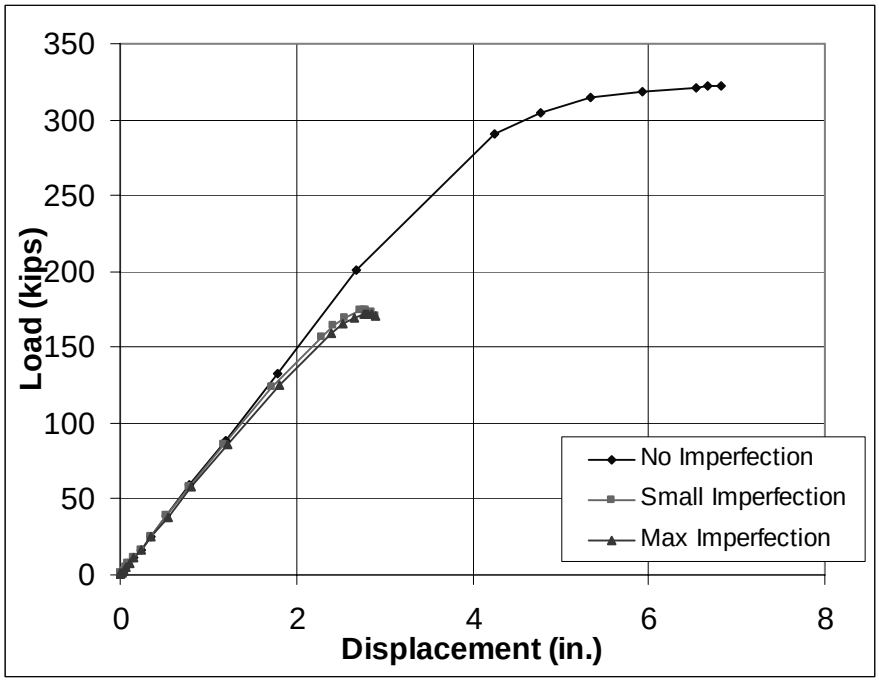

Figure 44. Load Displacement Curves for the 4:1 Tapered Girder.

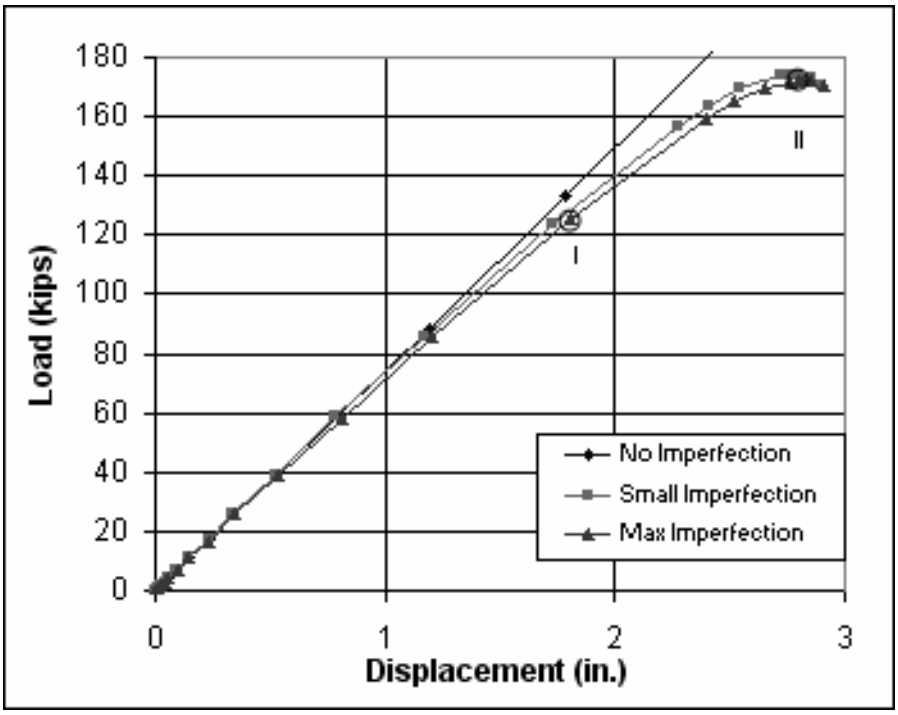

Figure 45. Enhanceed View of Load Displacement Curves for the 4:1 Tapered Girder.

The displacement used in Figures 44 and 45 is the total displacement of the node that lies at the juncture of the flange, bearing stiffener, and web. A portion of the reaction load was applied at this node. The area under the load displacement plot is a measure of the energy absorbed by the girder before failure. Failure of the girder is the point at which the girder can carry no additional load; at this point, the load displacement plot has a slope of zero. The stiffness of the system is defined as the slope of the load displacement plot. When the nonlinear Riks analyses were not seeded with an imperfection, the girders' webs did not buckle; rather, the girders failed in flexure. The failure load corresponded to the plastic moment capacity of the girder. Girders with imperfections all experienced shear failures.

Two increments from each analysis of the girders using the maximum imperfection were chosen for further study. These increments are labeled I and II and are shown on Figure 45; similar increments were chosen for the 1:1 tapered girder and the bent flange girder. The increments labeled I are in the linear portion of the load displacement plot. The increments labeled II are at the failure point.

The out-of-plane web displacements for the 4:1 tapered girder are shown in Figure 46 both in the linear region and at failure. This figure shows that the web deforms into a series of folds. As the load increases, the number and size of the folds also increases. Figure 46 shows that

the folds in the web panel begin in the deep portion of the girder; at failure, however, the folds have reached the shallow portion of the girder as well.

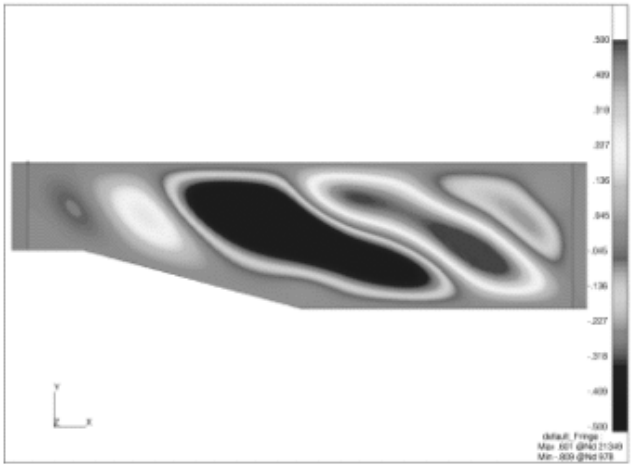

(a) Onset of Buckling

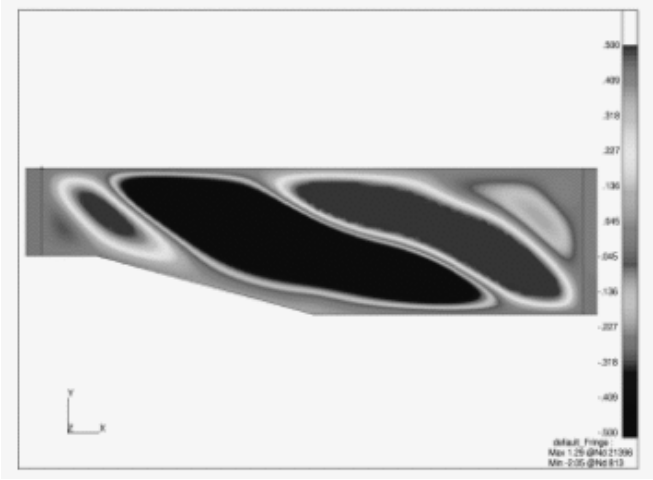

(b) Ultimate Load Condition

Figure 46. Contour Plots of Out-of-Plane Web Displacement for 4:1 Tapered Girders.

Tension diagonals form along these web folds. These tension diagonals can be visualized by investigating the principal stresses in the web panel. As the plate is bent, one side is placed in tension and the other side in compression. The stress distributions are very different depending on which side of the web is observed (*20*). The maximum principal stresses for each girder considered in this study are higher in magnitude than the minimum principal stresses in the deep portion of the web. This is true for both the linear region and at failure. It was also noted that for the analysis in the linear region, the maximum and minimum principal stresses take on similar magnitudes in the shallow portion of the web. As the folds in the web propagate through the

shallow portion, the maximum principal stress magnitudes increase and become larger than the minimum principal stress magnitudes in the shallow portion.

Despite substantial out-of-plane deformation of the web plate at relatively small loads, the stiffness of the system as a whole does not deteriorate. This observation indicates that the girders develop post-buckling strength. Despite the fact that the panels examined were end panels, with dapped geometry and stiffener spacing greater than 1.5 times the depth, the panels still developed post-buckling strength.

Post-buckling strength also explains why the ultimate strength of the girder with the maximum imperfection is nearly the same as the ultimate strength of the girder with the small imperfection. This behavior is due to the fact that the ultimate strength of the girder is not reached at initial buckling of the web. Instead, most of the capacity is developed through post-buckling strength. Whether the initial imperfection is small or large, ultimately the girder will conform to the lowest energy mode shape.

As shown in Figure 46, the folds in the web plate initiate in the deeper portion of the girders but propagate to the shallow portion as the load increases. The maximum principal stresses in the deep portion of the girders form tension diagonals along the folds in the web. Additionally, the maximum and minimum principal stresses are approximately equal in the shallow portion of the girder for loads in the linear load displacement region. Finally, at failure, the maximum principal stresses become much larger than the minimum principal stresses in the shallow region.

The behavior of the girders is consistent with a progressive buckling of the web plate. The web plate initially buckles in the deep portion of the girder, and this is where the tension field initiates. The shallow portion of the girder, which initially behaves as a beam, stabilizes this tension field. This beam action in the shallow portion accounts for the maximum and minimum principal stresses being approximately equal in the linear region. As the girder nears failure, the shallow portion of the web moves out of plane, and the tension field extends from the deep portion into the shallow portion. When the shallow portion no longer acts as a beam, the girder fails.

Tension field action is a way of visualizing the membrane stresses in a plate as a Pratt truss. Instead of showing the tension diagonal as a distribution of maximum principal stress, it was desirable to show it as an equivalent force acting on the web panel. To accomplish this goal,

free-body diagrams (FBDs) were created for the girder. A girder's FBD is generated by dividing the beam into sections and representing the internal forces. The girders with a tapered dapped detail were sectioned at the shallow, tapered, and deep portions of the web. The bent flange dapped detail had two sections, one for the shallow and one for the deep portion.

In order to calculate the internal forces acting in the beam, the bending and shear stresses were integrated over the depth of the girder using the trapezoidal method. This process was used to create FBDs of the girder during linear loading and at failure. The procedure may be summarized as follows:

- Integrate the shear stress to find the shear force. Additionally, integrate the bending stress to find equivalent compressive and tensile forces in the web.
- Calculate the net force and bending moment in the web due to the bending stress.
- Replace the compressive and tensile forces due to bending stress with the net force acting at the location which would produce the equivalent moment in the section.
- Find the resultant of the net force due to bending and the shear force. Also, find the angle at which this resultant acts.
- Produce an FBD showing a force acting at the top flange, bottom flange, and web.

FBDs were first created for the load case that lay within the linear load displacement region. The bending and shear stress distributions and FBDs for the linear behavior region are summarized for each dapped detail in Figures 47 through 52.

(a)

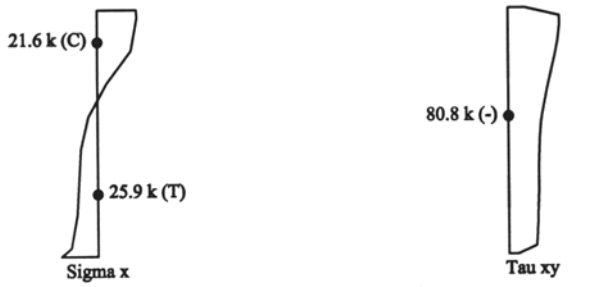

(b)

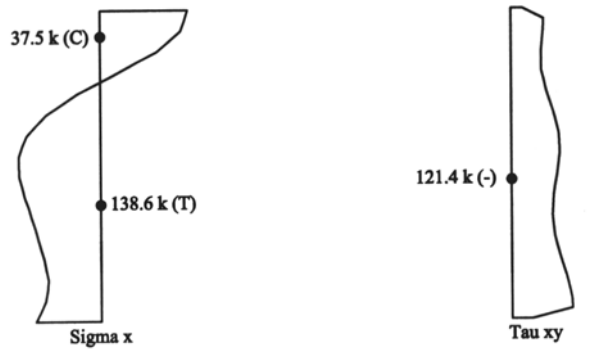

(c)

Figure 47. Bending and Shear Stress Distributions while Load Displacement Behavior Is Linear for 4:1 Tapered Detail. (a) Shallow End, (b) Tapered Portion, (c) Deep End.

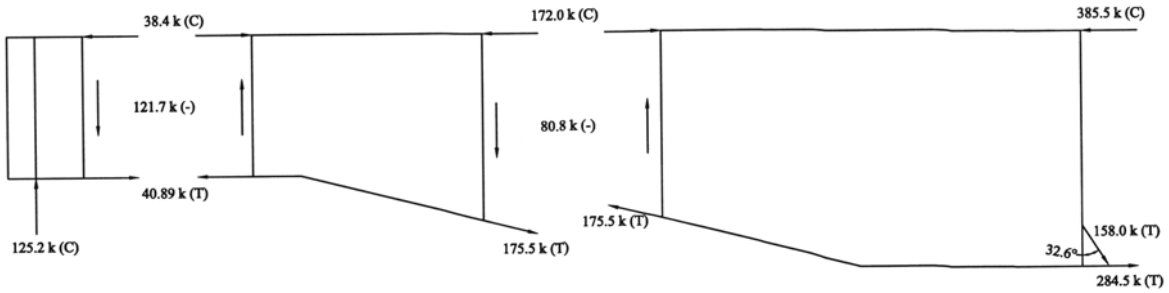

Figure 48. FBD for 4:1 Tapered Detail while Load Displacement Behavior Is Linear.

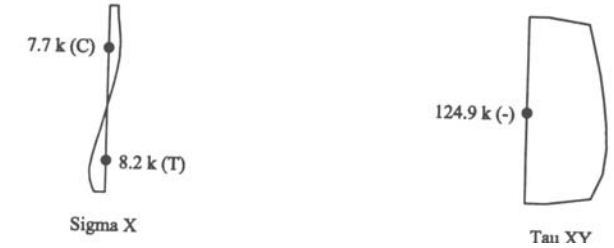

(a)

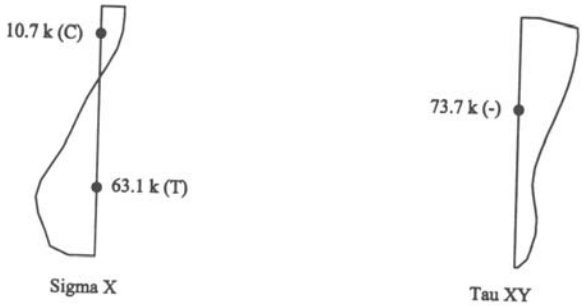

(b)

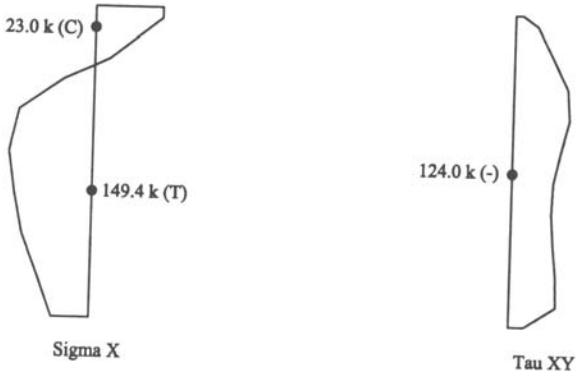

(c)

Figure 49. Bending and Shear Stress Distributions while Load Displacement Behavior Is Linear for 1:1 Tapered Detail. (a) Shallow End, (b) Tapered Portion, (c) Deep End.

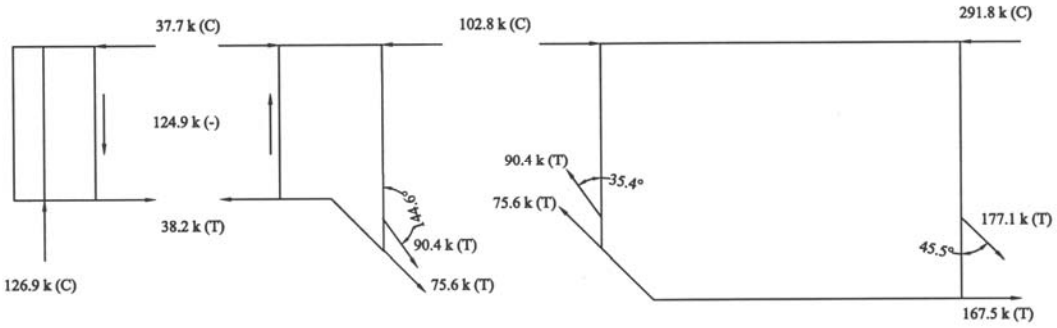

Figure 50. FBD for 1:1 Tapered Detail while Load Displacement Behavior Is Linear.

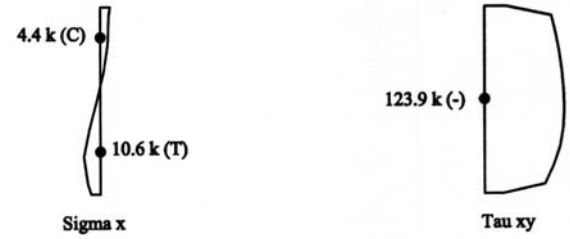

(a)

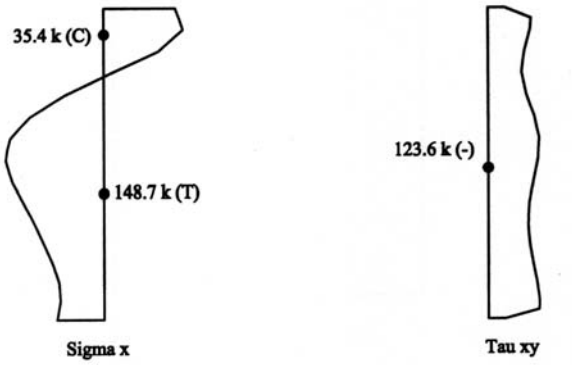

(b)

Figure 51. Bending and Shear Stress Distributions while Load Displacement Behavior Is Linear for Rounded Detail. (a) Shallow End, (b) Deep End.

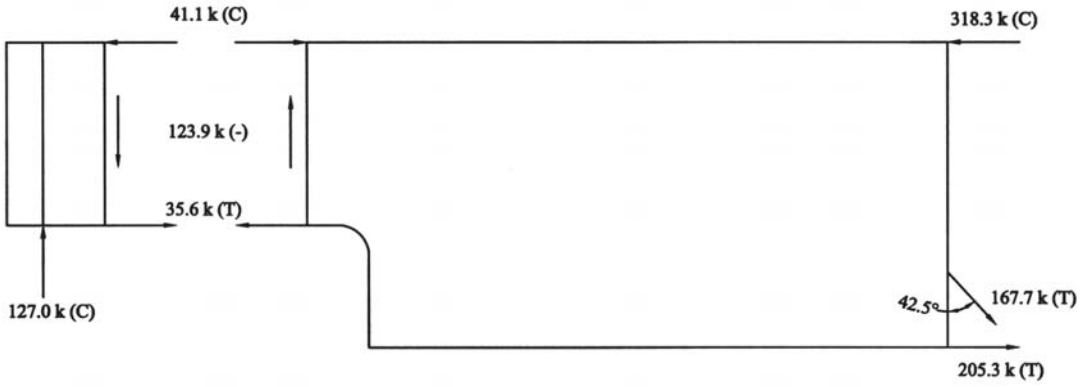

Figure 52. FBD for Rounded Detail while Load Displacement Behavior Is Linear.

The FBDs satisfy equilibrium within 5 percent. Error arises in the calculation for three reasons. First, the trapezoidal method, used to integrate the stresses, is only an approximate method. Second, since the models were composed of shell elements, some nodes lay at the juncture of the web plate and the flange plate. These nodes were required to account for shear stresses in both the plane of the web and the plane of the flange. Finally, large out-of-plane deformations decreased the accuracy of the calculation.

Figures 47, 49, and 51 show that the bending and shear stresses in the shallow portion of the girder are consistent with typical beam action. The shear stress is parabolic. The bending stresses in the web are small, and the neutral axis is approximately at the mid-height of the shallow portion. The resulting forces from these stresses are shown on the FBDs of Figures 48, 50, and 52. For the shallow region, the net force is almost entirely due to the shear stress; therefore, the effect from the bending stresses was neglected, and only shear force is shown.

Figures 47, 49, and 51 also show that the bending and shear stresses in the deep portion of the girder are consistent with tension field action. There is a large bending stress generated in the bottom of the web panel in the deep portion of the beam. The FBDs of Figures 48, 50, and 52 show the equivalent web force and the angle at which it acts. This is the tension diagonal formed by the maximum principal stresses.

Free-body diagrams were next created for the failure load case. The bending and shear stress distributions and FBDs for the linear behavior region are summarized for each dapped detail in Figures 53 through 58.

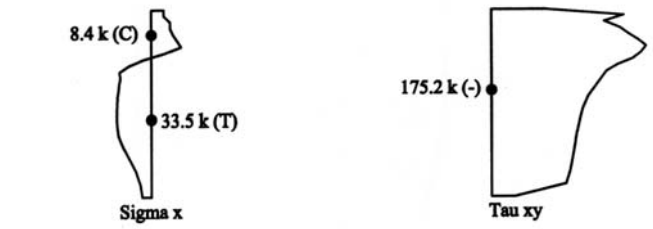

(a)

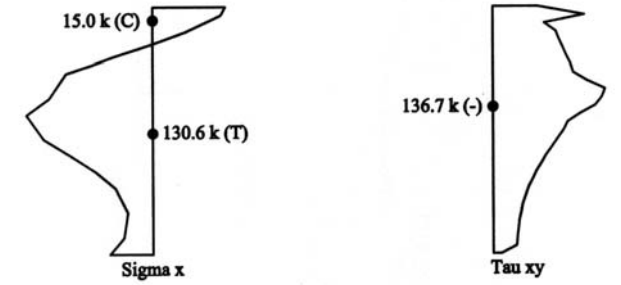

(b)

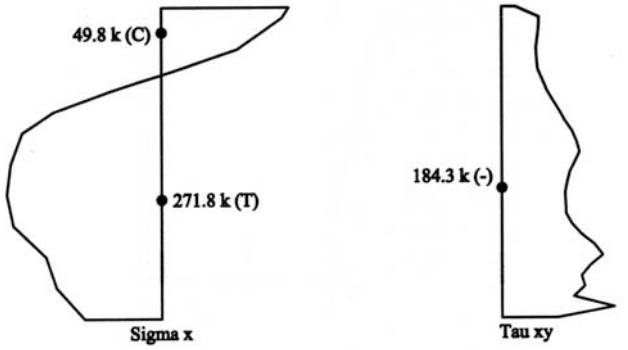

(c)

Figure 53. Bending and Shear Stress Distributions at Failure Load for 4:1 Tapered Detail. (a) Shallow End, (b) Tapered Portion, (c) Deep End.

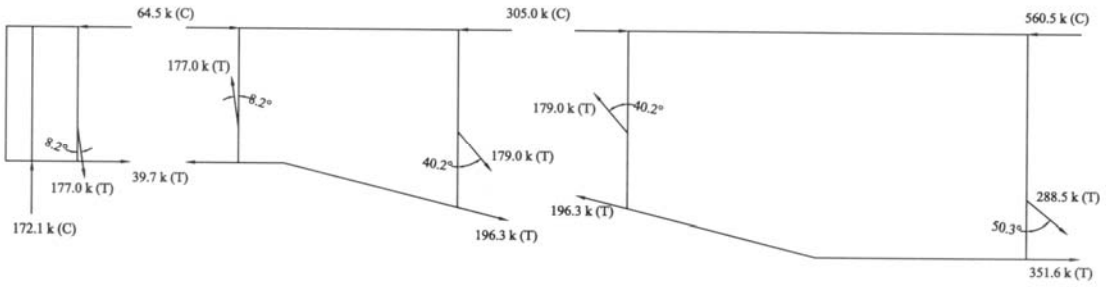

Figure 54. FBD for 4:1 Tapered Detail at Failure.

(a)

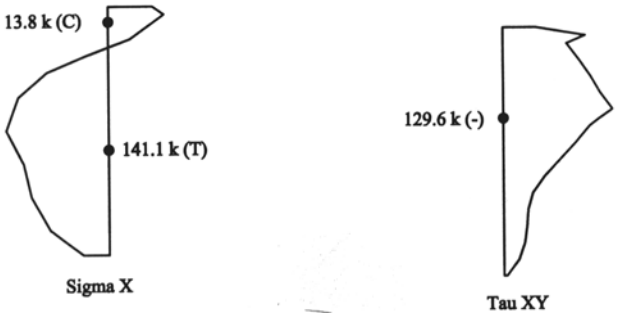

(b)

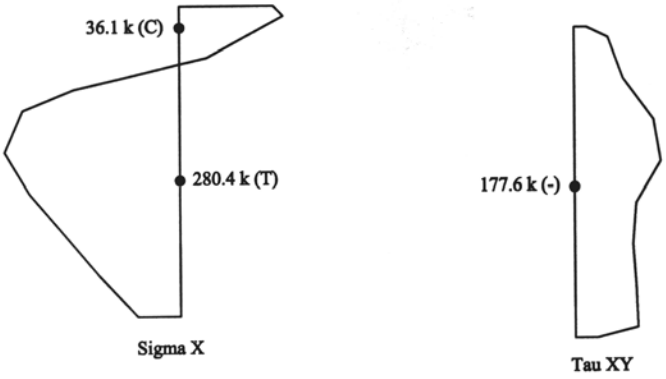

(c)

Figure 55. Bending and Shear Stress Distributions at Failure Load for 1:1 Tapered Detail. (a) Shallow End, (b) Tapered Portion, (c) Deep End.

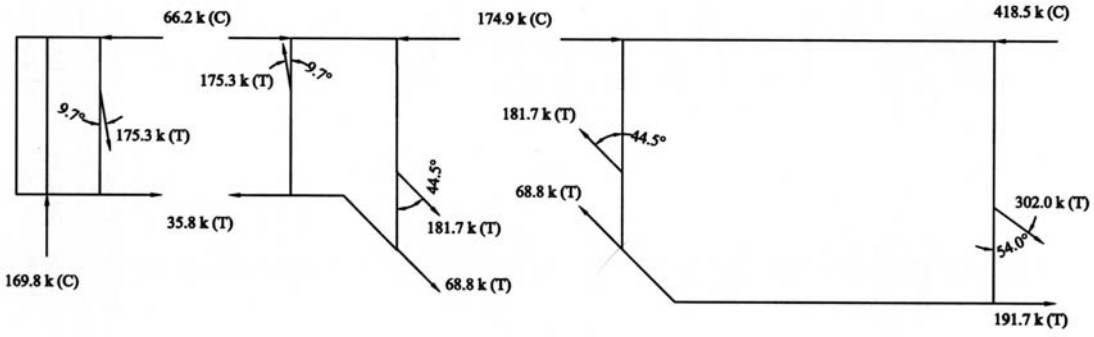

Figure 56. FBD for 1:1 Tapered Detail at Failure.

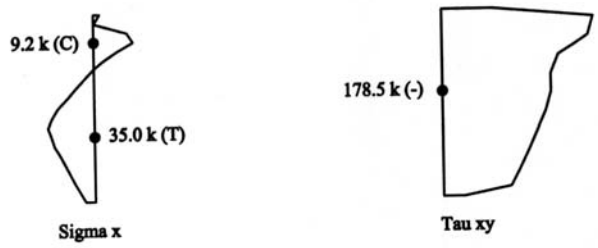

(a)

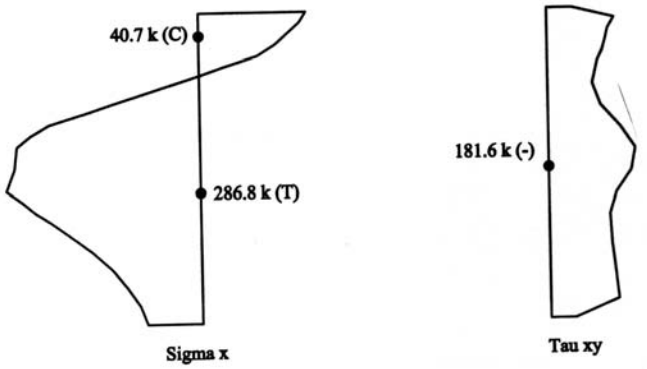

(b)

Figure 57. Bending and Shear stress Distributions at Failure Load for Rounded Detail. (a) Shallow End, (b) Deep End.

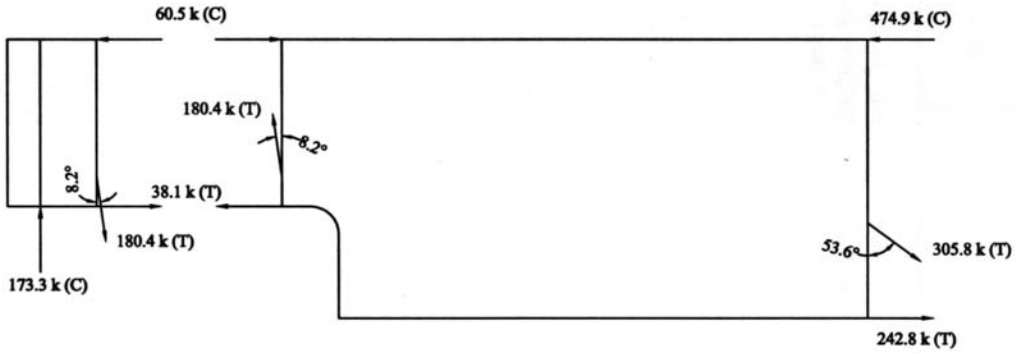

Figure 58. FBD for Rounded Detail at Failure.

Figures 53, 55, and 57 show that the stresses in the shallow portion are no longer consistent with beam action. The shallow portion of the girder begins to form a tension field. The FBDs in Figures 54, 56, and 58 show the beginnings of a tension field in the shallow portion of the web. The behavior in the deep portion of the girder is still a tension field, but the magnitude is larger. The girder fails when there is no remaining portion of the web behaving in beam action because there is nothing left to stabilize or anchor the tension field.

From the "General Behavior" numerical analyses above, it is apparent that the shallow end segment of the dapped end can behave as an independent shear panel, even without the presence of transverse stiffeners. In fact, for the specific geometries considered in these analyses, (i.e., $h_0/h_1 = 0.6$ and $a_1/h_0 = 0.67$; see Figures 38 and 39), the strength of this unstiffened end panel is sufficient to anchor a tension field from the adjacent panel. There is significant design advantage possible from this effect. Clearly, however, as either h_0/h_1 approaches unity *or* a_1/h_0 approaches zero, the dapped end panel cannot be considered separately from the adjacent panel without the addition of transverse stiffeners. The following conclusions are suggested by the results of this analysis:

- Dapped end panels studied develop significant post-buckling strength. The deep portion of the girder develops tension field action. Initially, the shallow portion of the girder remains as a beam and anchors the tension field. Failure occurs when the web in the shallow portion buckles inelastically and can no longer anchor the tension field.
- Dapped end panels without intermediate stiffeners between the first interior diaphragm and the bearing stiffener generate substantial shear capacities.
- Eliminating stiffeners would ease fabrication, lower cost, and decrease possible fatigue sensitivity.
- At ultimate loading conditions, the compression flange force is roughly twice the tension flange force in the tension field panel near the support.

ULTIMATE STRENGTH TESTS

Procedures

Based on the results from the analytical study of ultimate strength behavior of the dapped girder end details, a program of ultimate strength testing was designed. Three large-scale, bare-steel, I-shaped dapped girder end specimens were designed using A709-50W steel. The specimens are 62.5 in. deep at full section and 34 in. deep at the dapped end. They incorporate 0.25-in. by 60-in. web plates and 1.25-in. by 18-in. flange plates. The dimension "a_1" (see Figures 38 and 39) is 17 in. for the specimens. The maximum height-to-thickness ratio for the web plate is 240. The specimens were fabricated by Trinity Industries of Denton, Texas.

The critical dap ratios for the test specimens are $h_0/h_1 = 31.5/60.0 = 0.52$ and $a_1/h_0 = 17/31.5 = 0.54$ (see Figures 38 and 39). As compared to the ratios used in the "General Behavior" analyses above, the former ratio is more favorable and the latter less favorable in terms of promoting independent behavior of the end panel without using stiffeners.

Figure 59 shows a schematic drawing of each specimen and the idealized test setup. Note that the specimens were tested "upside down" compared to their normal installation in a bridge. This simplified laboratory procedures. In photographs that follow it is important to recognize that, in these tests, the tension flange is the top flange and the compression flange is the bottom flange. Each specimen was tested as a cantilever beam over a 288-in. span with load applied at its tip (dapped end). As seen in Figure 59, a 216-in. backspan was used to react the cantilever span. To ensure adequate strength, the backspan was fabricated using a heavily stiffened, 0.5-in. web plate. Two specimens incorporated a 4:1 tapered detail. One of these included intermediate welded transverse stiffeners at each of the two bends in the flange plate in addition to bearing stiffeners at support locations. The other tapered specimen used bearing stiffeners at support locations only; no other stiffeners were present in the test panel. The third specimen incorporated a 90-degree rounded detail. Similar to the second tapered specimen, the rounded specimen used bearing stiffeners at support locations only; no other stiffeners were present in the test panel. For all three specimens, a_1 was 17 in. For the stiffened tapered specimen that means that the first interior stiffener was 17 in. from the support and the second was 114.5 in. from the first. The goal of the tests was to examine nominal shear force resistance and, specifically, the post-buckling capacity of the test panels. Figure 59 also indicates with a circled "x" that lateral restraint was provided at each of the three load points.

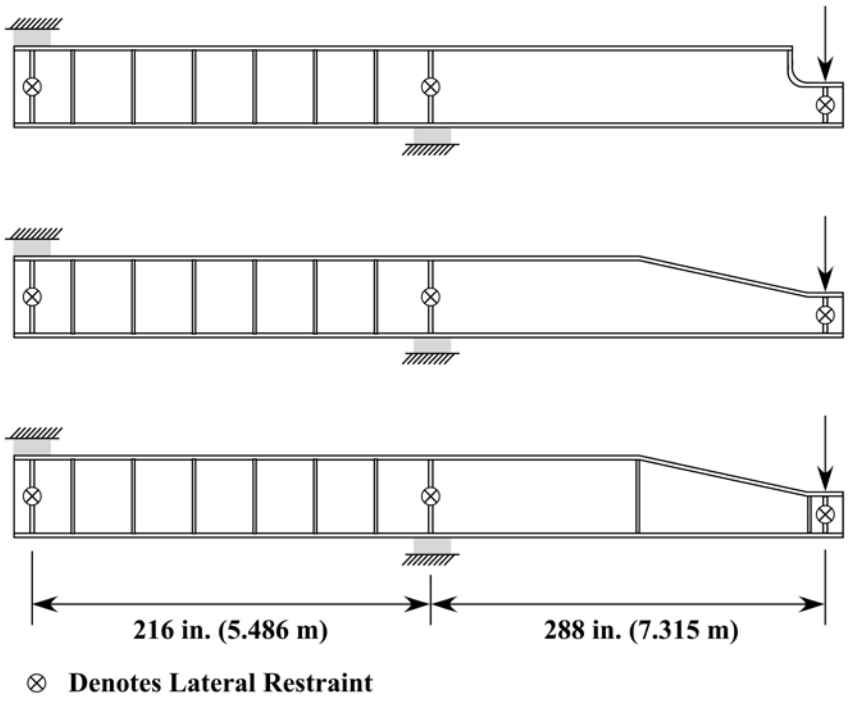

Figure 59. Schematic Drawing of Three Specimens and Idealized Test Setup.

Figure 60 is a photograph of the overall test setup with the 90-degree rounded specimen installed. A displacement transducer at the end of the specimen measured the displacement of the tip relative to the laboratory floor. Figure 61 is a photograph of the backspan and interior support during testing of the 90-degree rounded specimen. Figure 62 is a photograph of the backspan end-support configuration. Note that a displacement transducer was placed at the end of the specimen between the laboratory floor and the flange of the specimen. This transducer measured "uplift" of the backspan caused by the flexibility of the reaction frame. Using this measurement and the tip measurement described above, the tip displacement of the specimen can be determined very accurately. Figures 63 through 65 are pretest photographs of the rounded specimen, unstiffened tapered specimen, and stiffened tapered specimen, respectively. The test was conducted by increasing the actuator load slowly (approximately 1 in./minute) until the tip of the specimen displaced approximately 22 in. (i.e., L/13) and came into contact with the laboratory floor, at which time the test ended.

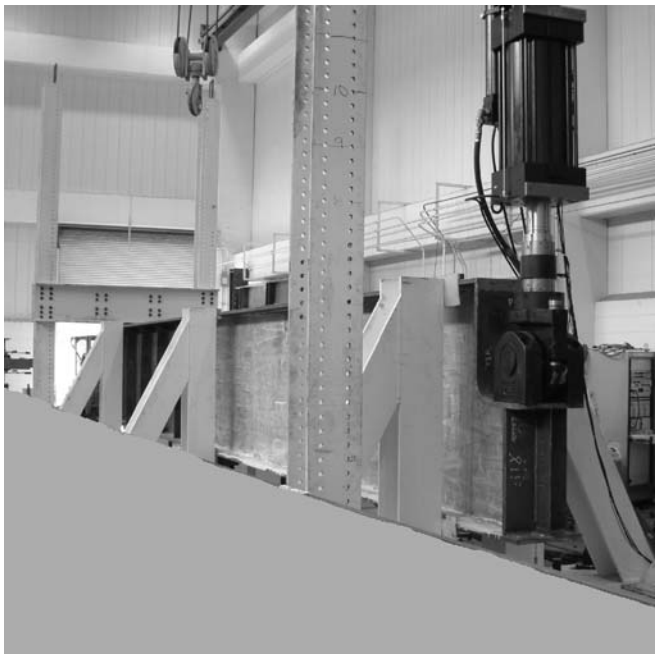

Figure 60. Photograph of Overall Test Setup.

Figure 61. Photograph of Heavily Stiffened Backspan and Interior Rocker Support.

Figure 62. Photograph of Backspan End-Support Configuration.

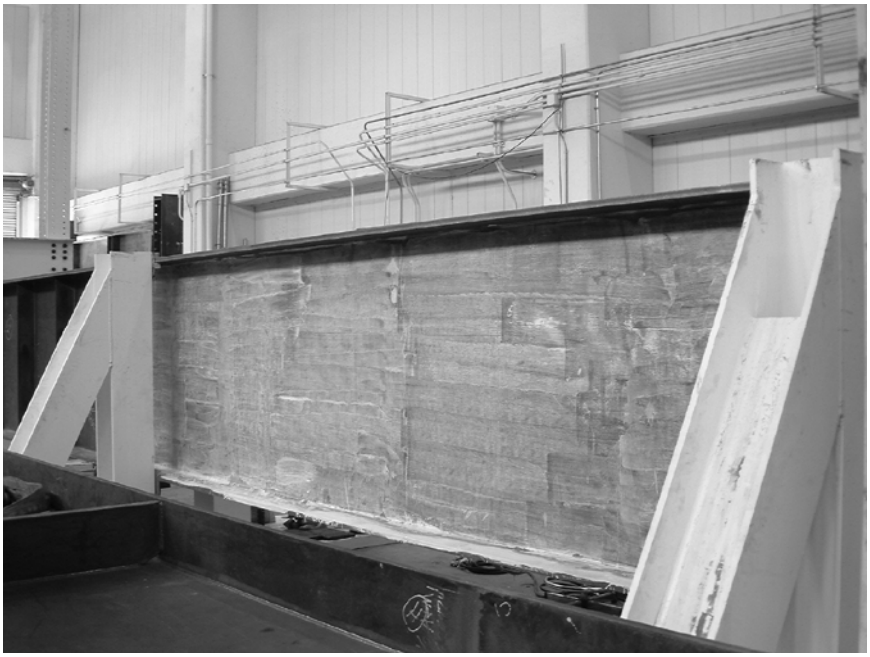

Figure 63. Pretest Photograph of 90-Degree Rounded Specimen.

Figure 64. Pretest Photograph of Unstiffened Tapered Specimen.

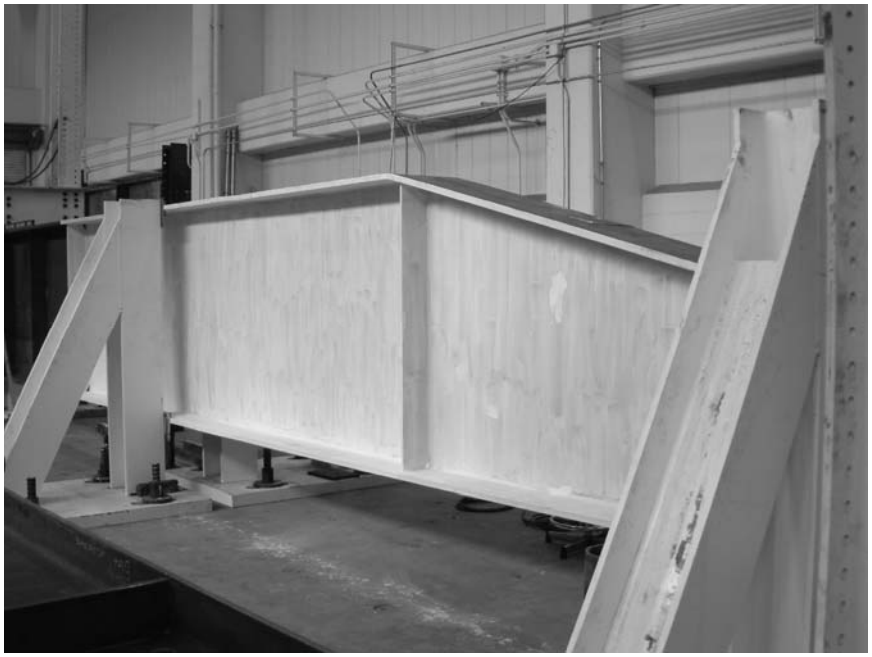

Figure 65. Pretest Photograph of Stiffened Tapered Specimen.

Design Calculations

Shear Force Capacity

The *AASHTO LRFD Bridge Design Specifications* (hereafter referred to as "the specifications") are used here to investigate the design shear force capacity of each of the three

test specimens (*21*). With web slenderness ratios equal to 240, it is immediately apparent that none of the test specimens conform to the web proportions requirements in section 6.10.2.1 of the specifications. For webs without longitudinal stiffeners, the web slenderness ratio is limited to 150; for webs with longitudinal stiffeners, the ratio is limited to 300. An intermediate value was selected for these specimens to ensure a shear-buckling failure mode and to allow observations of other aspects of behavior unique to a critically slender web. The use of 0.25-in. web plates in practice is discouraged strongly. Such slender plates are difficult to handle in a fabrication shop and often cause needlessly expensive weld-distortion problems during fabrication. In fact, these test specimens required heat straightening to remove excessive out-of-plane web-plate distortions caused by welding. The test specimens do conform to the flange proportions requirements of section 6.10.2.2 of the specifications.

For reference purposes, the yield moment and plastic moment for these specimens are 6230 ft-kips and 6680 ft-kips, respectively. Dividing these values by the cantilever span length yields the load required to produce flexural yielding and plastic hinging; these are 260 kips and 278 kips, respectively.

Stiffened Tapered Specimen

Ignoring its excessive slenderness, the web of the stiffened tapered specimen qualifies as a stiffened web under the provisions of section 6.10.9.1 from the specifications. Three shear panels exist in the test section: a rectangular end panel, a tapered interior panel, and a rectangular interior panel.

Rectangular End Panel

The provisions of section 6.10.9.3.3 from the specifications apply as follows.

(6.10.9.3.3-2) $$V_p = 0.58 \times 50 \times 31.5 \times 0.25 = 228.4 \text{, kips.}$$ (Equation 7)

(6.10.9.3.2-7) $$k = 5 + \frac{5}{\left(\frac{17}{31.5}\right)^2} = 22.17.$$ (Equation 8)

(6.10.9.3.2-4) $$1.12\sqrt{\frac{Ek}{F_{yw}}}=1.12\sqrt{\frac{29{,}000\times 22.17}{50}}=127.0. \qquad \text{(Equation 9)}$$

(6.10.9.3.2-4) $$\frac{D}{t_w}=\frac{31.5}{0.25}=126.0\le 127.0. \qquad \text{(Equation 10)}$$

Therefore,

(6.10.9.3.2-4) $$C=1.0, \qquad \text{(Equation 11)}$$

and

(6.10.9.3.3-1) $$V_n=1.0\times 228.4\cong \underline{228}\text{, kips.} \qquad \text{(Equation 12)}$$

Tapered Interior Panel

The calculation of the shear capacity of the tapered interior panel is completed here with two assumptions. First, the panel buckles at sections toward its deeper end; accordingly the full depth of the girder can be used to compute the initial buckling capacity of the panel. Second, the tapered geometry can be regarded simply as an absence of otherwise non-participatory material, and, therefore, the panel develops a normal tension field. The provisions of section 6.10.9.3.2 from the specifications apply as follows.

(6.10.9.3.2-1) $$\frac{2Dt_w}{\left(b_{fc}t_{fc}+b_{ft}t_{ft}\right)}=\frac{2\times 60\times 0.25}{\left(18\times 1.25+18\times 1.25\right)}=0.6667\le 2.5. \qquad \text{(Equation 13)}$$

(6.10.9.3.2-3) $$V_p=0.58\times 50\times 60\times 0.25=435.0\text{, kips.} \qquad \text{(Equation 14)}$$

(6.10.9.3.2-7) $$k=5+\frac{5}{\left(\frac{114.5}{60}\right)^2}=6.373. \qquad \text{(Equation 15)}$$

(6.10.9.3.2-6) $$1.40\sqrt{\frac{Ek}{F_{yw}}}=1.40\sqrt{\frac{29{,}000\times 6.373}{50}}=85.12. \qquad \text{(Equation 16)}$$

(6.10.9.3.2-6) $$\frac{D}{t_w}=\frac{60}{0.25}=240.0>85.12.$$ (Equation 17)

Therefore,

(6.10.9.3.2-6) $$C=\frac{1.57}{\left(\frac{60}{0.25}\right)^2}\left(\frac{29{,}000\times 6.373}{50}\right)=0.1007,$$ (Equation 18)

and

(6.10.9.3.2-2) $$V_n=435.0\left(0.1007+\frac{0.87(1-0.1007)}{\sqrt{1+\left(\frac{114.5}{60}\right)^2}}\right)\cong \underline{202}\text{, kips.}$$ (Equation 19)

Rectangular Interior Panel

The provisions of section 6.10.9.3.2 from the specifications apply as follows.

(6.10.9.3.2-1) $$\frac{2Dt_w}{\left(b_{fc}t_{fc}+b_{ft}t_{ft}\right)}=\frac{2\times 60\times 0.25}{(18\times 1.25+18\times 1.25)}=0.6667\le 2.5.$$ (Equation 20)

(6.10.9.3.2-3) $$V_p=0.58\times 50\times 60\times 0.25=435.0\text{, kips.}$$ (Equation 21)

(6.10.9.3.2-7) $$k=5+\frac{5}{\left(\frac{156.5}{60}\right)^2}=5.735.$$ (Equation 22)

(6.10.9.3.2-6) $$1.40\sqrt{\frac{Ek}{F_{yw}}}=1.40\sqrt{\frac{29{,}000\times 5.735}{50}}=80.74.$$ (Equation 23)

(6.10.9.3.2-6) $$\frac{D}{t_w} = \frac{60}{0.25} = 240.0 > 80.74.$$ (Equation 24)

Therefore,

(6.10.9.3.2-6) $$C = \frac{1.57}{\left(\frac{60}{0.25}\right)^2}\left(\frac{29{,}000 \times 5.735}{50}\right) = 0.0907,$$ (Equation 25)

and

(6.10.9.3.2-2) $$V_n = 435.0\left(0.0907 + \frac{0.87(1-0.0907)}{\sqrt{1+\left(\frac{156.5}{60}\right)^2}}\right) \cong \underline{163}, \text{ kips.}$$ (Equation 26)

Calculation Result

The rectangular interior panel is the controlling panel and is expected to develop a tension field. The expected shear capacity during the test is more than 163 kips. This number will be referred to later as the "AASHTO 2004 Capacity" for this specimen. The expected mode of failure for the specimen is excessive post-buckling shear deformation in the rectangular interior panel, with associated vertical buckling of the compression flange.

Unstiffened Tapered Specimen

Full Unstiffened Web Panel

The web of the unstiffened tapered specimen is considered unstiffened under the provisions of section 6.10.9.1 from the specifications. The specifications do not permit consideration of tension field action in an unstiffened web. Ignoring the excessive slenderness of the web, the provisions of section 6.10.9.2 from the specifications apply as follows.

(6.10.9.2-2) $$V_p = 0.58 \times 50 \times 60 \times 0.25 = 435.0, \text{ kips.}$$ (Equation 27)

$$k = 5.0.$$ (Equation 28)

(6.10.9.3.2-6) $$1.40\sqrt{\frac{Ek}{F_{yw}}} = 1.40\sqrt{\frac{29{,}000 \times 5.0}{50}} = 75.39.$$ (Equation 29)

(6.10.9.3.2-6) $$\frac{D}{t_w} = \frac{60}{0.25} = 240.0 > 75.39.$$ (Equation 30)

Therefore,

(6.10.9.3.2-6) $$C = \frac{1.57}{\left(\frac{60}{0.25}\right)^2}\left(\frac{29{,}000 \times 5.0}{50}\right) = 0.0790,$$ (Equation 31)

and

(6.10.9.2-1) $$V_n = 0.0790 \times 435.0 \cong \underline{34.4}, \text{ kips.}$$ (Equation 32)

Calculation Result

The specifications limit the design capacity of this specimen to the initial buckling capacity, 34.4 kips. This number will be referred to later as the "AASHTO 2004 Capacity" for this specimen.

90-Degree Rounded Specimen

Full Unstiffened Web Panel

The web of the 90-degree rounded specimen is considered unstiffened under the provisions of section 6.10.9.1 from the specifications. The specifications do not permit consideration of tension field action in an unstiffened web. Ignoring the excessive slenderness of the web, the provisions of section 6.10.9.2 from the specifications apply as follows.

(6.10.9.2-2) $$V_p = 0.58 \times 50 \times 60 \times 0.25 = 435.0, \text{ kips.}$$ (Equation 33)

$$k = 5.0.$$ (Equation 34)

(6.10.9.3.2-6) $$1.40\sqrt{\frac{Ek}{F_{yw}}} = 1.40\sqrt{\frac{29{,}000 \times 5.0}{50}} = 75.39.$$ (Equation 35)

(6.10.9.3.2-6) $$\frac{D}{t_w} = \frac{60}{0.25} = 240.0 > 75.39.$$ (Equation 36)

Therefore,

(6.10.9.3.2-6) $$C = \frac{1.57}{\left(\frac{60}{0.25}\right)^2}\left(\frac{29{,}000 \times 5.0}{50}\right) = 0.0790, \quad \text{(Equation 37)}$$

and

(6.10.9.2-1) $$V_n = 0.0790 \times 435.0 \cong \underline{34.4}, \text{ kips.} \quad \text{(Equation 38)}$$

Initial Elastic Deflections

The webs of the test specimens are very slender, $D/t_w = 240$, and the specimens are deep compared to their spans, $L_{max}/D = 4.6$. Considering these two factors in combination, shear deformations are expected to constitute an appreciable portion of the total tip deflection of each specimen, even during the initial elastic loading range. The calculations below use approximate estimates of internal work to determine an effective elastic stiffness, K_{eff}, for the load versus tip deflection behavior of the specimens. In the calculations that follow, the variables, W_{intV} and W_{intF}, refer to the internal work associated with shear deformation and flexural deformation, respectively. Figure 66 shows a schematic diagram of the situation for these beams.

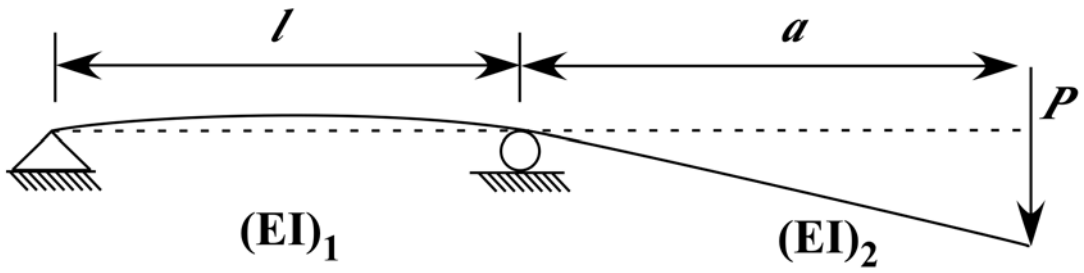

Figure 66. Schematic Drawing of Test Specimen Deflection.

Shear Deformation Energy

The shear deformation energy calculations below are based on the assumption that an average shear stress is distributed uniformly within the web plate. For the given test setup and specimen design, two shear spans must be considered separately: the backspan and the cantilever span. This is because the two spans have a different thickness web plate and a different length. The total energy is simply the sum of the contributions from each span. The calculation for this test setup is relatively straightforward, since each of the spans is subjected to a constant shear force over its entire length. In the calculations below, the variable, *P*, is the applied load at the tip

of the specimen, the variable, l, is the length of a given shear span, and the variable, Vol_{WEB}, is the total volume of the web plate in a given shear span. The other variables should be familiar.

For a given span:

$$\tau_{avg} = \frac{V}{A_w} = \frac{V}{Dt_w}. \quad \text{(Equation 39)}$$

$$W_{\text{int}_V} = \frac{1}{2}\tau\gamma \times Vol_{WEB}, \gamma = \frac{\tau}{G}. \quad \text{(Equation 40)}$$

$$W_{\text{int}_V} = \frac{1}{2}\frac{V}{Dt_w}\frac{V}{GDt_w}(Dt_w\, l) = \frac{V^2 l}{2GDt_w}. \quad \text{(Equation 41)}$$

With reference to Figure 66, here is the result for the back span:

$$W_{\text{int}_V} = \frac{\left(\frac{lP}{a}\right)^2 l}{2GDt_w}. \quad \text{(Equation 42)}$$

With reference to Figure 66, here is the result for the cantilever span:

$$\frac{P^2 a}{2GDt_w}. \quad \text{(Equation 43)}$$

The total estimated elastic shear deformation energy for each specimen is given here as a function of tip load:

$$W_{\text{int}_V}^{Total} \approx \frac{1}{2\times 11{,}200\times 60}\left(\frac{\left(\frac{288P}{216}\right)^2 216}{0.5} + \frac{P^2 288}{0.25}\right) \cong 0.001429\times P^2, \text{ kip-in.} \quad \text{(Equation 44)}$$

Flexural Deformation Energy

The flexural deformation energy calculations below are based on traditional beam theory. Referring to Figure 66, the following is an expression for the deflection at the tip of the beam.

$$\delta = \frac{P\,a^2 l}{3(E\,I)_1} + \frac{P\,a^3}{3(E\,I)_2}. \qquad \text{(Equation 45)}$$

Using Equation 44, the internal energy due to flexure can be written down simply.

$$W_{\text{int}_F} = \frac{1}{2} P\,\delta. \qquad \text{(Equation 46)}$$

The total estimated elastic flexural deformation energy for each specimen is given here as a function of tip load:

$$W_{\text{int}_F}^{Total} \approx \frac{1}{2} \times P \times \left(\frac{P \times 288^2 \times 216}{3 \times 29{,}000 \times 51{,}211} + \frac{P \times 288^3}{3 \times 29{,}000 \times 46{,}711} \right) \cong 0.004950 \times P^2, \text{ kip-in.} \qquad \text{(Equation 47)}$$

Design Estimate of Effective Structural Stiffness

Here is an expression for the total internal energy of the test specimens in the elastic loading range considering flexural and shear deformation in both spans.

$$W_{\text{int}}^{Total} = W_{\text{int}}^{Total} + W_{\text{int}}^{Total} = 0.006379 \times P^2, \text{ kip-in.} \qquad \text{(Equation 48)}$$

Here is the expression for the total external work of the applied tip load.

$$W_{ext}^{Total} = \frac{1}{2} P\,\delta, \text{ where } \delta = \frac{P}{K_{eff}}. \qquad \text{(Equation 49)}$$

Therefore we have,

$$W_{ext}^{Total} = \frac{P^2}{2K_{eff}}. \quad \text{(Equation 50)}$$

Equating total internal work and total external work, we can solve for K_{eff}.

$$\frac{P^2}{2K_{eff}} = 0.006379 \times P^2. \quad \text{(Equation 51)}$$

$$K_{eff} \cong 78.4, \text{ kips/in.} \quad \text{(Equation 52)}$$

Summary of Deflection Calculations

Equations 44, 47, and 48 can be used to estimate the contributions from each mode of deformation to total tip deflection. In the expressions below, δ_V represents the tip deflection caused by shear force, δ_F represents the tip displacement caused by bending moment, or flexure, and δ_T represents the total tip deflection.

$$\delta_V = \frac{0.001429}{0.006379} \times \delta_T \cong 0.224 \times \delta_T, \text{ in.} \quad \text{(Equation 53)}$$

$$\delta_F = \frac{0.004950}{0.006379} \times \delta_T \cong 0.776 \times \delta_T, \text{ in.} \quad \text{(Equation 54)}$$

Elastic shear deformation in the web plates is expected to constitute more than 20 percent of the total expected tip deflection of each specimen during the initial elastic loading range. Using Equation 45, a calculation of initial elastic stiffness excluding shear distortion of the beam would give 101 kips/in. as compared to the 78 kips/in. obtained by including shear distortion.

Overview of Experimental Results

Each of the three specimens developed a tension field during the tests and subsequently displayed substantial post-buckling capacity. The ultimate failure mode of each specimen was excessive shear deformation of the web and associated vertical buckling of the compression flange. Figure 67 shows a plot of tip load (panel shear force) versus tip deflection for the 90-

degree rounded specimen. The shear capacity as determined using AASHTO provisions is also indicated on the figure. Figure 68 shows a plot of tip load (panel shear force) versus tip deflection for the unstiffened tapered specimen. The shear capacity as determined using AASHTO provisions is also indicated on the figure. Figure 69 shows a plot of tip load (panel shear force) versus tip deflection for the stiffened tapered specimen. (The stiffened tapered specimen was unloaded after reaching its peak resistance to make an adjustment to the hydraulic system and controller. The specimen was then reloaded and taken to maximum displacement to complete the test.) The shear capacity as determined using AASHTO provisions is also indicated on the figure. As seen in Figures 67 through 69, the stiffened tapered specimen attained the largest capacity: 230 kips. It is especially interesting to observe that the capacities of the 90-degree rounded specimen and the unstiffened tapered specimen were nearly the same: 191 kips and 195 kips, respectively. At a displacement of approximately 22 in., a slight increase in load for each specimen indicates contact between the specimen tip and the laboratory floor, which marked the end of the test. Figures 70 through 75 show schematic drawings and photographs of the inelastic folds that formed along the tension field in each specimen.

Figure 76 shows a plot of tip load versus tip deflection that includes all of the specimen results simultaneously. As evidenced in Figure 76, the initial elastic stiffnesses among the specimens was nearly identical: approximately 67 kips/in. Based upon the deflection calculations above, 78 kips/in. was expected when a simple calculation of shear distortion was included. The relative error of that estimate is approximately 16 percent, which is quite good, especially given the simplistic nature of the calculations used. Neglecting shear distortion of the beam, one would have expected initial elastic stiffness of 101 kips/in., which is in error by slightly more than 50 percent of the actual value. Clearly, shear distortion plays a significant role in the deformation behavior of these test specimens.

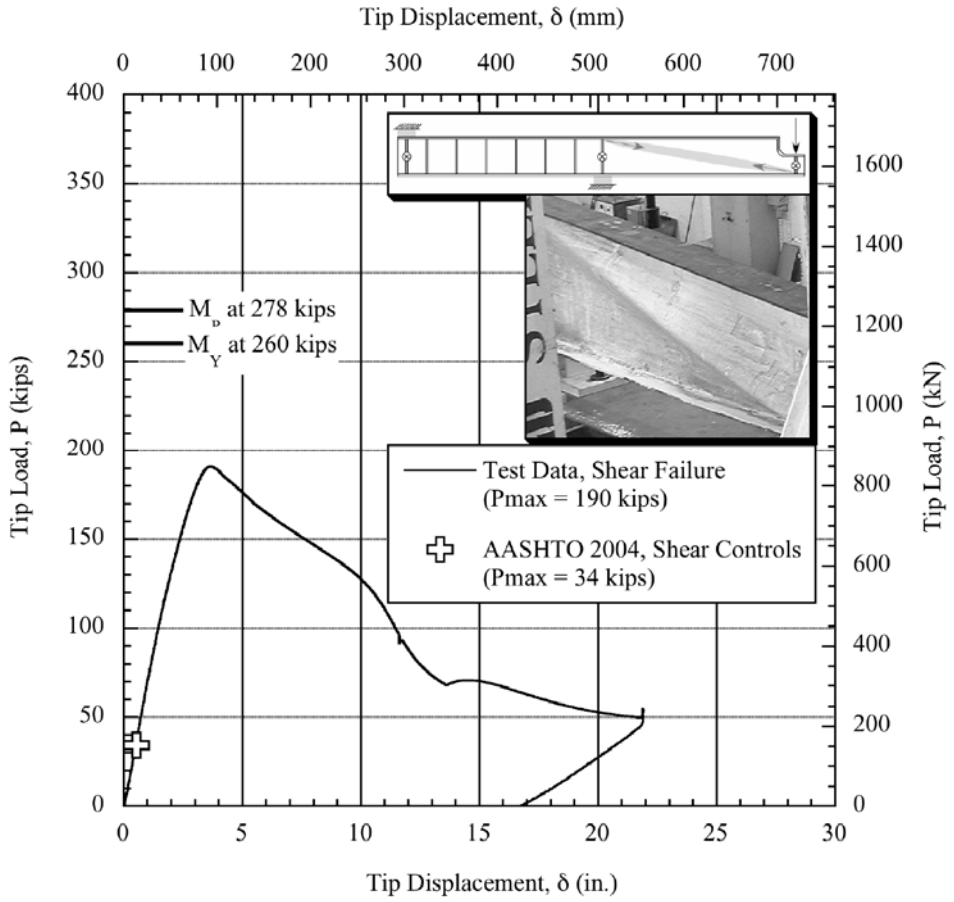

Figure 67. Plot of Tip Load versus Tip Deflection for the 90-Degree Rounded Specimen.

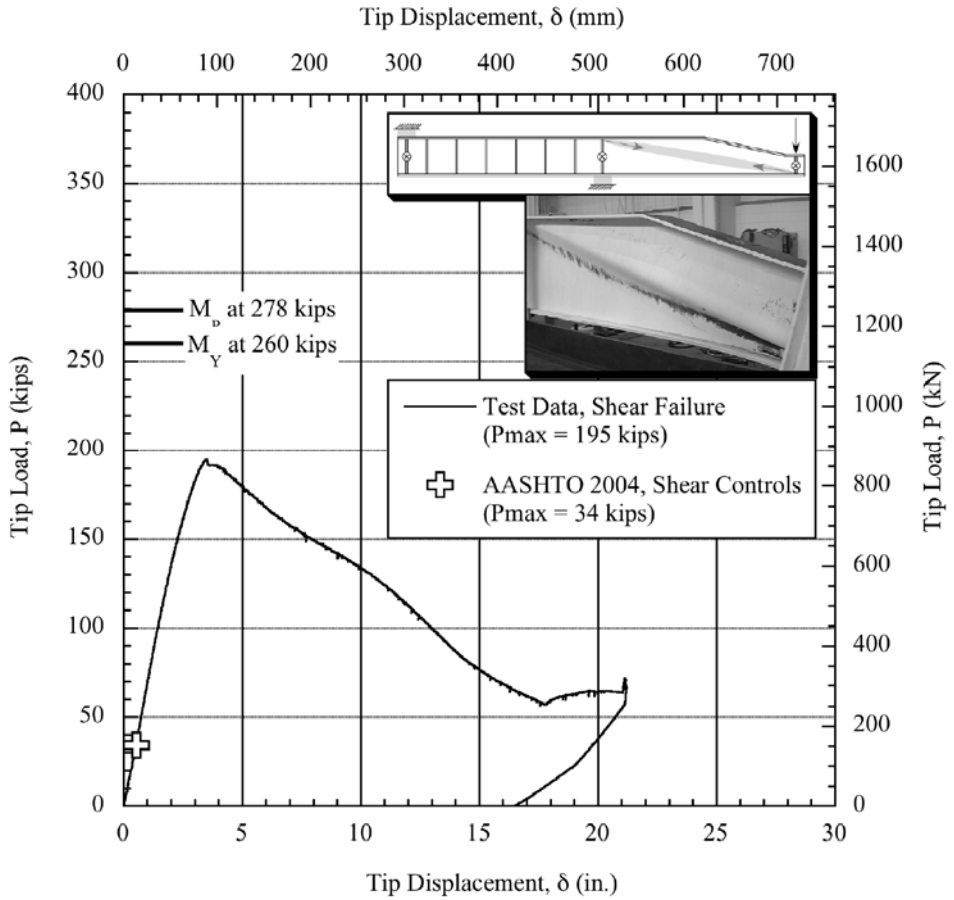

Figure 68. Plot of Tip Load versus Tip Deflection for the Unstiffened Tapered Specimen.

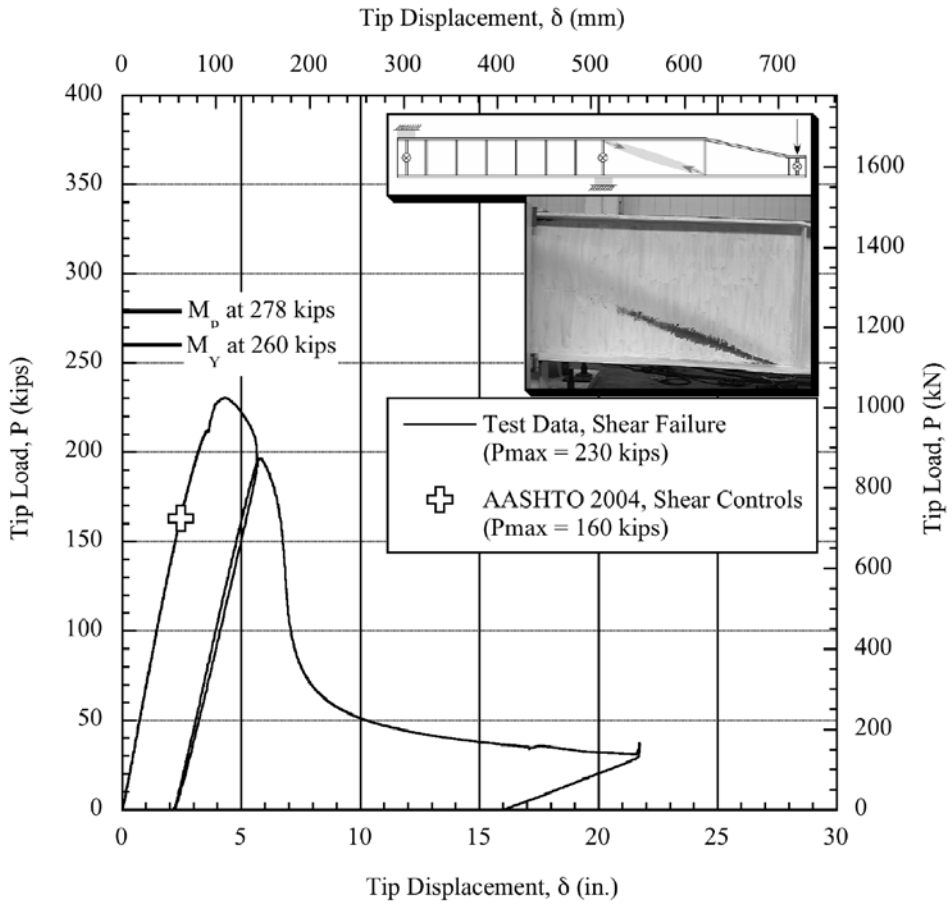

Figure 69. Plot of Tip Load versus Tip Deflection for the Stiffened Tapered Specimen.

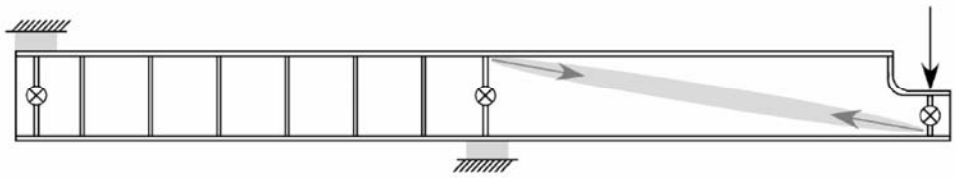

Figure 70. Schematic Drawing of Tension Field in the 90-Degree Rounded Specimen.

Figure 71. Photograph of Tension Field in the 90-Degree Rounded Specimen.

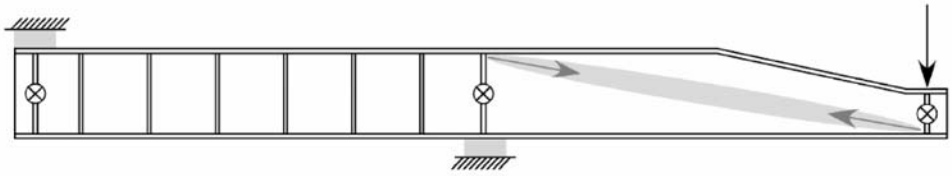

Figure 72. Schematic Drawing of Tension Field in the Unstiffened Tapered Specimen.

Figure 73. Photograph of Tension Field in the Unstiffened Tapered Specimen.

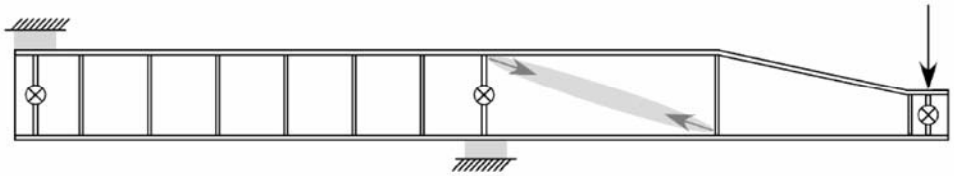

Figure 74. Schematic Drawing of Tension Field in the Stiffened Tapered Specimen.

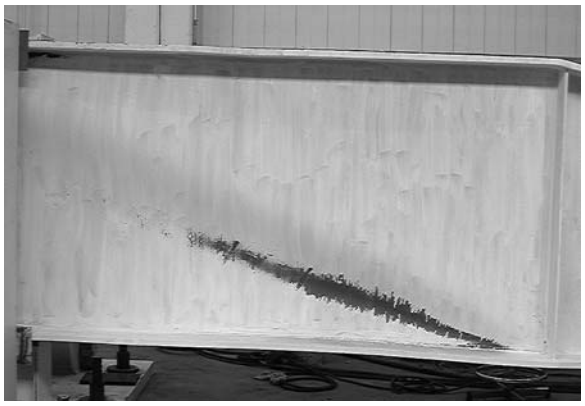

Figure 75. Photograph of Tension Field in the Stiffened Tapered Specimen.

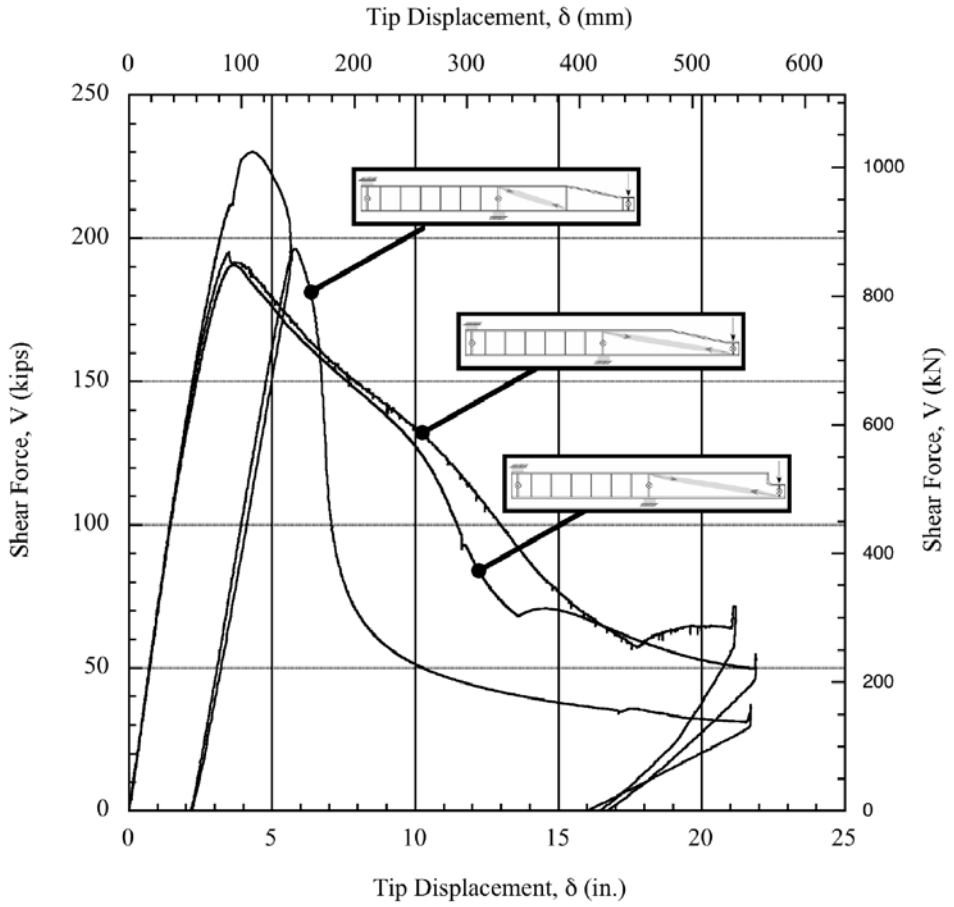

Figure 76. Plot of Load versus Deflection Showing All Three Specimens.

Table 9 summarizes the failure mode and strength calculations based on the AASHTO specifications and compares these results with the test data. Recall that the specifications employ load and resistance factor design algorithms. The "factor of safety" label on the last column, therefore, is perhaps a bit of a misnomer. The reliability index for designs completed using the specifications depends also upon the nature of the loading considered on the structure and associated load factors. Nevertheless the term factor of safety is used here in its classical meaning as the ratio of observed capacity to estimated capacity. For the stiffened specimen, the specifications seem to provide a very good basis for both anticipating the ultimate behavior of the specimen and for determining an appropriate design strength value for the specimen. For the unstiffened specimens, the specifications do not offer good quantitative insight.

Table 9. Comparison of Nominal Capacity Calculations and Test Results.

	AASHTO 2004		Test Results		
Specimen	Controlling Limit State	Tip Capacity (kips)	Mode of Failure	Maximum Load (kips)	Factor of Safety
90-Degree Rounded	Shear	34	Shear	190	5.59
Unstiffened Taper	Shear	34	Shear	195	5.73
Stiffened Taper	Shear	160	Shear	230	1.44

ULTIMATE STRENGTH ANALYSIS PART II: ANALYSIS OF TEST SPECIMENS

Procedures

The three 0.25-in. web test specimens were subjected to further analytical study. For each of the specimens, a finite-element model was created and a Riks analysis, as described previously, was executed. Each model was 44.25 ft (531 in.) long. The flanges were 18 in. wide and 1.25 in. thick in all cases. The webs were 60 in. tall at full height. The shallow web height at the beginning of the dapped end was approximately 31.5 in. For the 4:1 tapered specimens, the inclined region continued over a length of 114.5 in.

Load and boundary conditions for the models were selected to recreate the experimental conditions. Figure 77 illustrates these conditions schematically. A girder with a tapered dap is shown, as are the three bearing stiffeners common to all dapped geometries. In the finite element analyses, the specimen was not inverted as it had been for the tests. Therefore, in the models, the compression flange is the top flange, and the tension flange is the bottom flange in the test panel. A load, designated P, was placed at the left bearing stiffener (at x = 7 in.), near the dapped end. Pin restraints were used at the mid-bearing stiffener (at x = 295 in.) and end-bearing stiffener (x = 511 in.); these restraints were distributed across the girder flanges. All three bearing stiffeners were also restrained from movement out of plane to simulate the restraint conditions imposed during testing. In the backspan, intermediate bearing stiffeners were placed approximately 25 in. apart between the central support and the end-bearing stiffeners to prevent the backspan from failing in advance of the test panel.

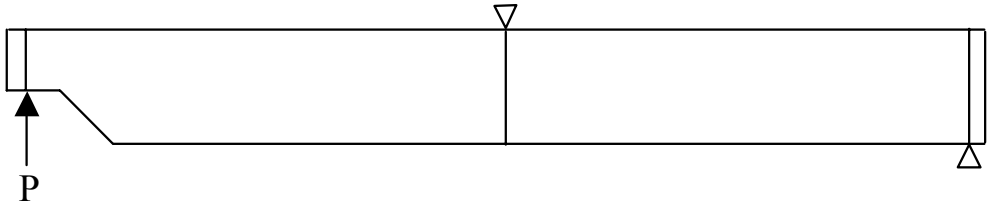

Figure 77. Load and Boundary Conditions Applied to Model.

The girders were modeled in Patran, version 2004, and ABAQUS 6.3 was used for the analysis portion. As in the previously conducted parametric study, a linear eigenvalue analysis was conducted to determine the girders' buckling behavior. The first mode shape generated from this analysis was then used to seed a geometric imperfection in the Riks analysis. This imperfection is necessary to examine post-buckling behavior. Without it, the Riks analysis would tend to duplicate the bifurcation behavior seen during the eigenvalue analysis.

Aside from the introduction of a geometric imperfection, an additional nonlinearity was incorporated into the Riks analyses. The girder was modeled as structural steel with a yield point of 50 ksi and a modulus of elasticity of 30,000 ksi. Since it is unlikely that a girder would reach its ultimate strength without using some or all of its plastic capacity, it was necessary to include a nonlinear material definition in these analyses. In order to compare the effects of different material properties on the simulation, two different stress-strain curves were used for the Riks analyses. The first material was elastic-perfectly plastic. The second material included the effects of strain hardening with a yield plateau. The stress-strain curves used to define these materials are shown below in Figure 78.

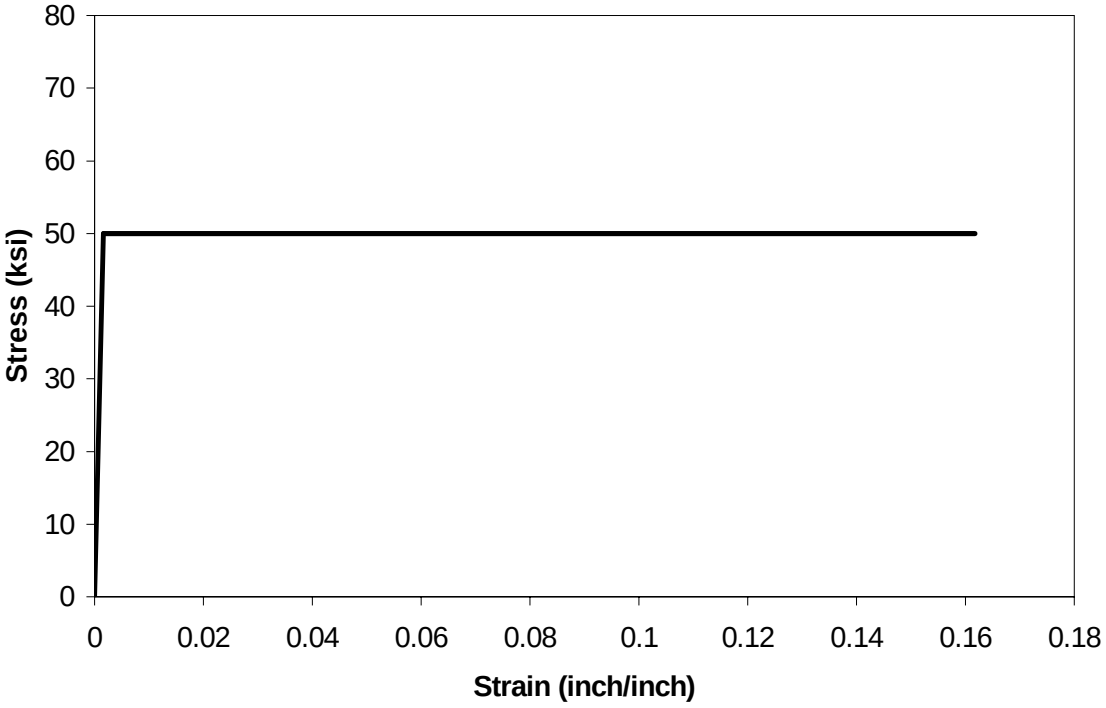

(a)

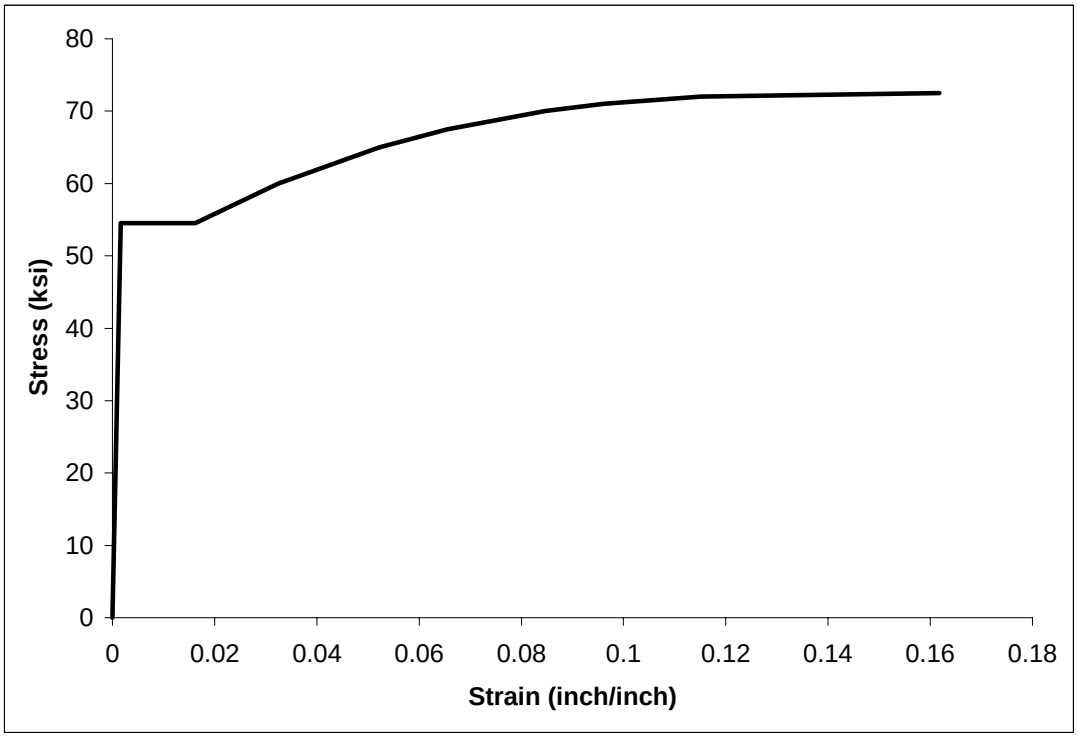

(b)

Figure 78. Stress-Strain Curves Used to Conduct Riks Analyses: (a) Elastic-Perfectly Plastic Material Definition, (b) Strain Hardening Material Definition That Includes a Yield Plateau.

The girders were modeled by shell elements with six degrees of freedom (three displacements and three rotations). The shell elements were located at the midpoints of the structural elements (web or flange) that they represented. This configuration meant that the web height was extended to the midpoint of each flange. The rounded dapped detail girders contained between 193,000 and 198,000 nodes and 63,900 to 65,400 elements. The tapered dapped detail girders realized 180,000 to 183,000 nodes and 59,600 to 60,700 elements. The addition or removal of stiffeners accounts for the variation in finite-element model size.

Details of the Riks analysis were model dependent. The load, P, was applied at the left bearing stiffener, as shown in Figure 77. This load was distributed along the nodes defining the bottom edge of the stiffener; 40 nodes were used in the round analyses and 41 for the tapered girders. The magnitude of the distributed load thus applied was determined iteratively and varied between 0.10 and 0.50 kips per node. This variation was necessary because some models were more sensitive to load incrementation than others; if the load steps taken were too large, full nonlinear behavior would not be reached. However, smaller time steps were much more computationally expensive and ran the risk of the analysis ending before the girder had reached its peak load.

As explained previously, a Riks analysis gradually increases the load applied to a model, solving for the appropriate load parameter as well as the model response. The analysis ends when a predetermined value of the load parameter is reached, a maximum number of steps is exceeded, or the load parameter increments become too small. This last condition generally indicates that a load plateau has been reached.

Table 10 provides a brief summary of the results from the finite element analyses. It is interesting to note that regardless of the specific geometry of the specimen (i.e., tapered, stiffened, or neither), the initial buckling load is nearly identical for all the cases: 59 kips on average with a standard deviation of ±0.85 kips. Contour plots of the von Mises yield function stresses and renderings of the deformed shape of each specimen at ultimate load for these models appear in Figures 79, 80, and 81. Pronounced evidence of a tension field is apparent in each of these figures. In all plots the units of stress indicated are ksi (1 ksi = 6.89 Mpa).

Table 10. Finite Element Shear Capacities for the Girders with 0.25-in. Thick Webs.

Dapped Detail	Ultimate Shear, Elastic-Perfectly Plastic (kips)	Ultimate Shear with Strain Hardening (kips)	Buckling Load (kips)
Round, no stiffeners	167.6	176.1	58.6
Tapered, no stiffeners	173.6	182.3	57.9
Tapered, two stiffeners	194.0	207.3	59.6

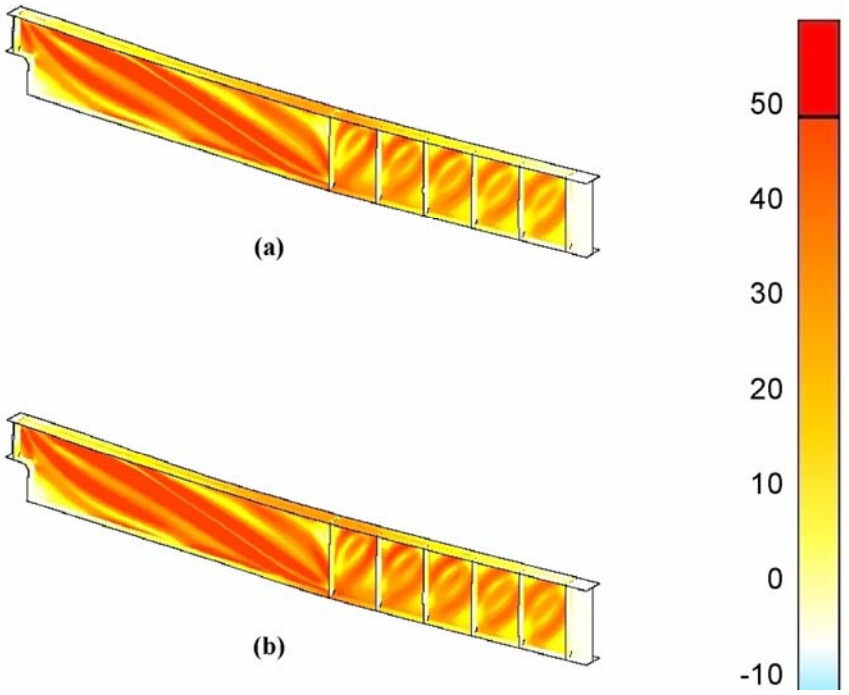

Figure 79. Von Mises Stresses Superimposed over the Deformed Shape of the Unstiffened 90-Degree Rounded Girder with 0.25-in. Thick Web. Stresses Are Plotted at the Ultimate Load Step for (a) Elastic-Perfectly Plastic and (b) Strain Hardening Materials.

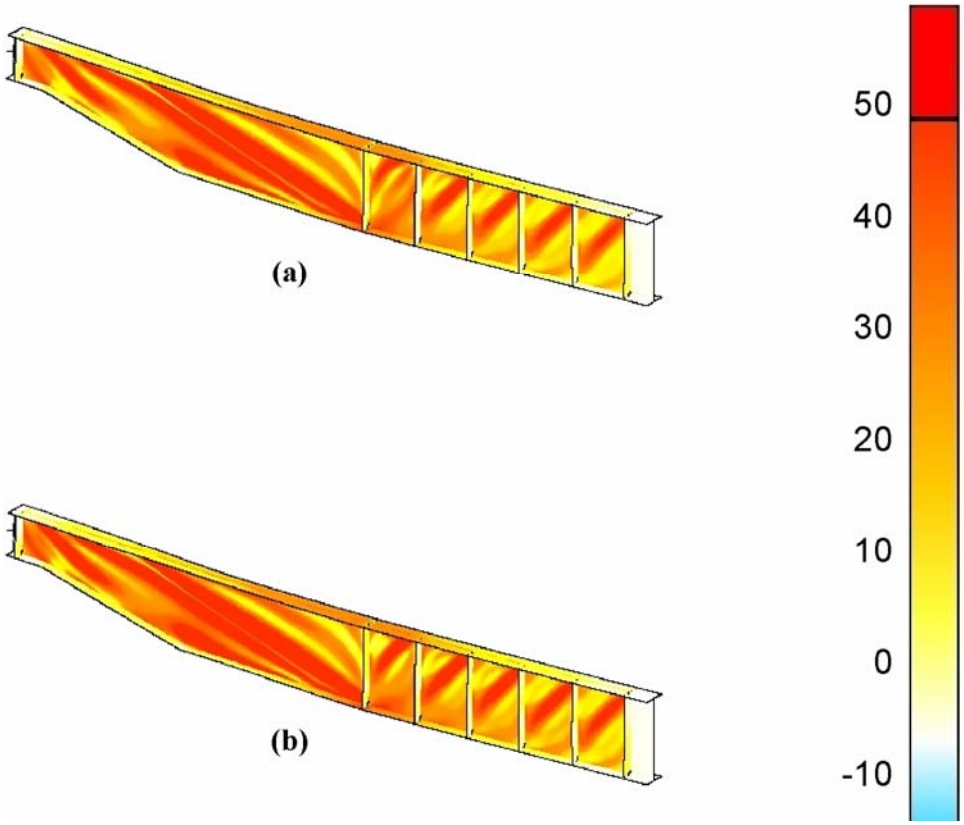

Figure 80. Von Mises Stresses Superimposed over the Deformed Shape of the Unstiffened Tapered Girder with 0.25-in. Thick Web. Stresses Are Plotted at the Ultimate Load Step for (a) Elastic-Perfectly Plastic and (b) Strain Hardening Materials.

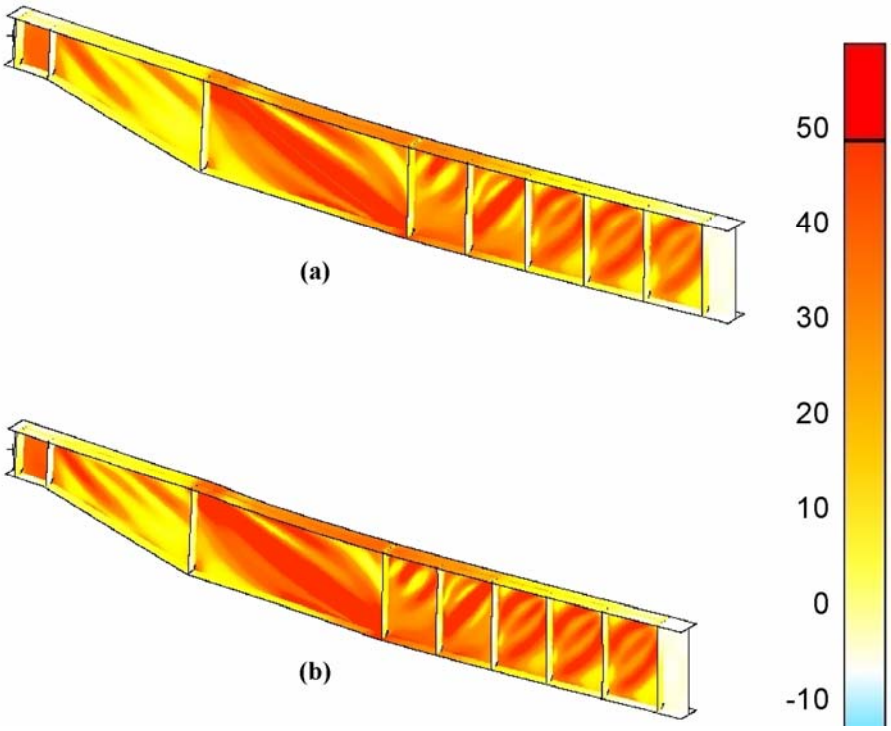

Figure 81. Von Mises Stresses Superimposed over the Deformed Shape of the Stiffened Tapered Girder with 0.25-in. Thick Web. Stresses Are Plotted at the Ultimate Load Step for (a) Elastic-Perfectly Plastic and (b) Strain Hardening Materials.

Hypothetical Design Calculations for Shear Force Capacity

The following set of design calculations is hypothetical in nature and requires some explanation before proceeding. As discussed previously, analysis results suggest that for dapped details geometrically similar to those of these test specimens (i.e., $h_0/h_1 = 31.5/60.0 = 0.52$ and $a_1/h_0 = 17/31.5 = 0.54$; see Figures 38 and 39), the supported end of the dap behaves as an independent shear panel capable of anchoring a tension field. In addition, the results suggest that the adjacent unstiffened web plate develops a full tension field and associated post-buckling capacity.

The set of calculations below is an attempt to apply simple design equations to quantify the shear capacity observed in the detailed, fully nonlinear finite-element models and in laboratory tests. In the calculations below, the supported end of the dap is considered a proper end panel, and the remainder of the web plate is considered a proper interior panel. (Note that in reality there are only two sets of bearing stiffeners on the web, and they are separated by a distance of 24 ft, i.e., 4.8D.)

Hypothetical Calculations: Unstiffened Tapered Specimen Including Tension Field

Hypothetical Rectangular End Panel

The provisions of section 6.10.9.3.3 from the specifications are applied as follows.

(6.10.9.3.3-2) $$V_p = 0.58 \times 50 \times 31.5 \times 0.25 = 228.4 \text{, kips.}$$ (Equation 55)

(6.10.9.3.2-7) $$k = 5 + \frac{5}{\left(\frac{17}{31.5}\right)^2} = 22.17.$$ (Equation 56)

(6.10.9.3.2-4) $$1.12\sqrt{\frac{E\,k}{F_{yw}}} = 1.12\sqrt{\frac{29{,}000 \times 22.17}{50}} = 127.0.$$ (Equation 57)

(6.10.9.3.2-4) $$\frac{D}{t_w} = \frac{31.5}{0.25} = 126.0 \le 127.0.$$ (Equation 58)

Therefore,

(6.10.9.3.2-4) $$C = 1.0,$$ (Equation 59)

and

(6.10.9.3.3-1) $$V_n = 1.0 \times 228.4 \cong \underline{228} \text{, kips.}$$ (Equation 60)

Hypothetical Tapered Interior Panel

As before, the calculation of the shear capacity of this hypothetical tapered interior panel is completed with two assumptions. First, the panel buckles at sections toward its deeper end; accordingly the full depth of the girder can be used to compute the initial buckling capacity of the panel. Second, the tapered geometry can be regarded simply as an absence of otherwise non-participatory material and, therefore, the panel develops a normal tension field. The provisions of section 6.10.9.3.2 from the specifications are applied as follows.

(6.10.9.3.2-1) $$\frac{2Dt_w}{\left(b_{fc}t_{fc} + b_{ft}t_{ft}\right)} = \frac{2 \times 60 \times 0.25}{\left(18 \times 1.25 + 18 \times 1.25\right)} = 0.6667 \le 2.5.$$ (Equation 61)

(6.10.9.3.2-3) $$V_p = 0.58 \times 50 \times 60 \times 0.25 = 435.0 \text{, kips.}$$ (Equation 62)

(6.10.9.3.2-7) $$k = 5 + \frac{5}{\left(\frac{271}{60}\right)^2} = 5.245.$$ (Equation 63)

(6.10.9.3.2-6) $$1.40\sqrt{\frac{E\,k}{F_{yw}}} = 1.40\sqrt{\frac{29{,}000 \times 5.245}{50}} = 77.22.$$ (Equation 64)

(6.10.9.3.2-6) $$\frac{D}{t_w} = \frac{60}{0.25} = 240.0 > 77.22.$$ (Equation 65)

Therefore,

(6.10.9.3.2-6) $$C = \frac{1.57}{\left(\frac{60}{0.25}\right)^2}\left(\frac{29{,}000 \times 5.245}{50}\right) = 0.0829,$$ (Equation 66)

and

(6.10.9.3.2-2) $$V_n = 435.0\left(0.0829 + \frac{0.87(1 - 0.0829)}{\sqrt{1 + \left(\frac{271}{60}\right)^2}}\right) \cong \underline{111} \text{, kips.}$$ (Equation 67)

Calculation Result

By this set of calculations, the expected failure load is more than 111 kips. The specimen is expected to fail by excessive shear deformation in the open panel after developing appreciable post-buckling capacity. This number will be referred to later as "0-2102 TFA" for this specimen.

Hypothetical Calculations: Unstiffened 90-Degree Rounded Specimen Including Tension Field

Hypothetical Rectangular End Panel

The provisions of section 6.10.9.3.3 from the specifications are applied as follows.

(6.10.9.3.3-2) $$V_p = 0.58 \times 50 \times 31.5 \times 0.25 = 228.4 \text{, kips.}$$ (Equation 68)

(6.10.9.3.2-7) $$k = 5 + \frac{5}{\left(\frac{17}{31.5}\right)^2} = 22.17.$$ (Equation 69)

(6.10.9.3.2-4) $$1.12\sqrt{\frac{E\,k}{F_{yw}}} = 1.12\sqrt{\frac{29{,}000 \times 22.17}{50}} = 127.0.$$ (Equation 70)

(6.10.9.3.2-4) $$\frac{D}{t_w} = \frac{31.5}{0.25} = 126.0 \le 127.0.$$ (Equation 71)

Therefore,

(6.10.9.3.2-4) $$C = 1.0,$$ (Equation 72)

and

(6.10.9.3.3-1) $$V_n = 1.0 \times 228.4 \cong \underline{228}, \text{ kips.}$$ (Equation 73)

Hypothetical Rectangular Interior Panel

As before, the calculation of the shear capacity of this hypothetical tapered interior panel makes two assumptions. First, the panel buckles at sections toward its deeper end; accordingly the full depth of the girder can be used to compute the initial buckling capacity of the panel. Second, the tapered geometry can be regarded simply as an absence of otherwise non-participatory material and, therefore, the panel develops a normal tension field. The provisions of section 6.10.9.3.2 from the specifications are applied as follows.

(6.10.9.3.2-1) $$\frac{2Dt_w}{\left(b_{fc}t_{fc} + b_{ft}t_{ft}\right)} = \frac{2 \times 60 \times 0.25}{\left(18 \times 1.25 + 18 \times 1.25\right)} = 0.6667 \le 2.5.$$ (Equation 74)

(6.10.9.3.2-3) $$V_p = 0.58 \times 50 \times 60 \times 0.25 = 435.0, \text{ kips.}$$ (Equation 75)

(6.10.9.3.2-7) $$k = 5 + \frac{5}{\left(\frac{271}{60}\right)^2} = 5.245.$$ (Equation 76)

(6.10.9.3.2-6) $$1.40\sqrt{\frac{Ek}{F_{yw}}} = 1.40\sqrt{\frac{29{,}000 \times 5.245}{50}} = 77.22. \quad \text{(Equation 77)}$$

(6.10.9.3.2-6) $$\frac{D}{t_w} = \frac{60}{0.25} = 240.0 > 77.22. \quad \text{(Equation 78)}$$

Therefore,

(6.10.9.3.2-6) $$C = \frac{1.57}{\left(\frac{60}{0.25}\right)^2}\left(\frac{29{,}000 \times 5.245}{50}\right) = 0.0829, \quad \text{(Equation 79)}$$

and

(6.10.9.3.2-2) $$V_n = 435.0\left(0.0829 + \frac{0.87(1-0.0829)}{\sqrt{1+\left(\frac{271}{60}\right)^2}}\right) \cong \underline{111}, \text{ kips.} \quad \text{(Equation 80)}$$

Calculation Result

By this set of calculations, the expected failure load is more than 111 kips. The specimen is expected to fail by excessive shear deformation in the open panel after developing appreciable post-buckling capacity. This number will be referred to later as "0-2102 TFA" for this specimen.

Comparison of Experimental and Analytical Results

Figures 82, 83, and 84 show tip load versus tip deflection plots for the three test specimens. On each plot, the original test data are included as well as the results from the two different finite element analyses of each specimen: the elastic-perfectly plastic material model and the elastic-strain hardening material model. In addition, the results of the hypothetical capacity calculations are shown along with the current AASHTO 2004 specifications capacities. In general, they show excellent agreement between the test data and the finite element analyses. Both sets of analyses slightly underpredict the ultimate strength. In the case of the elastic-perfectly plastic analyses, the underprediction is caused by two effects. The real yield strength of the steel in the specimens is expected to be more than 50 ksi, and the real steel will exhibit strain-hardening behavior. In the case of the strain-hardening model, the underprediction probably results from the real yield strength of the steel being greater than 50 ksi. The conclusion is,

however, that these types of finite element analyses are quite successful at modeling the complex inelastic shear buckling behavior of steel plate girders that are nonprismatic. When minimum specified values of yield strength are used, the models give conservative results. The estimated initial elastic stiffness obtained from the finite element analyses is 72 kips/in. The relative error of this estimate compared to the value from the tests, 67 kips/in., is approximately 7 percent. During these tests, the peak reaction at the middle support was 536 kips. Among other sources of error, it is possible that the middle support of the test setup actually contributed some flexibility that was not measured during the tests. The project supervisor observed on occasion that movement of the laboratory floor during a test can contribute a small amount of measurement error.

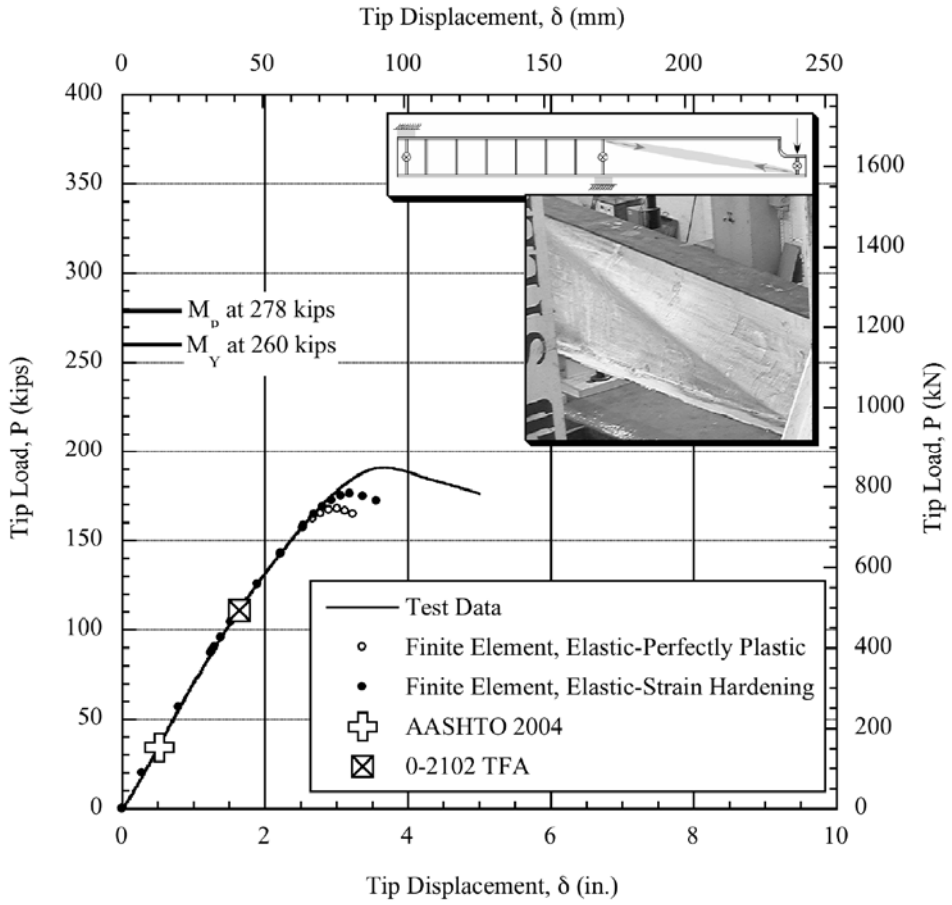

Figure 82. Plot of Tip Load versus Tip Deflection for the 90-Degree Rounded Specimen.

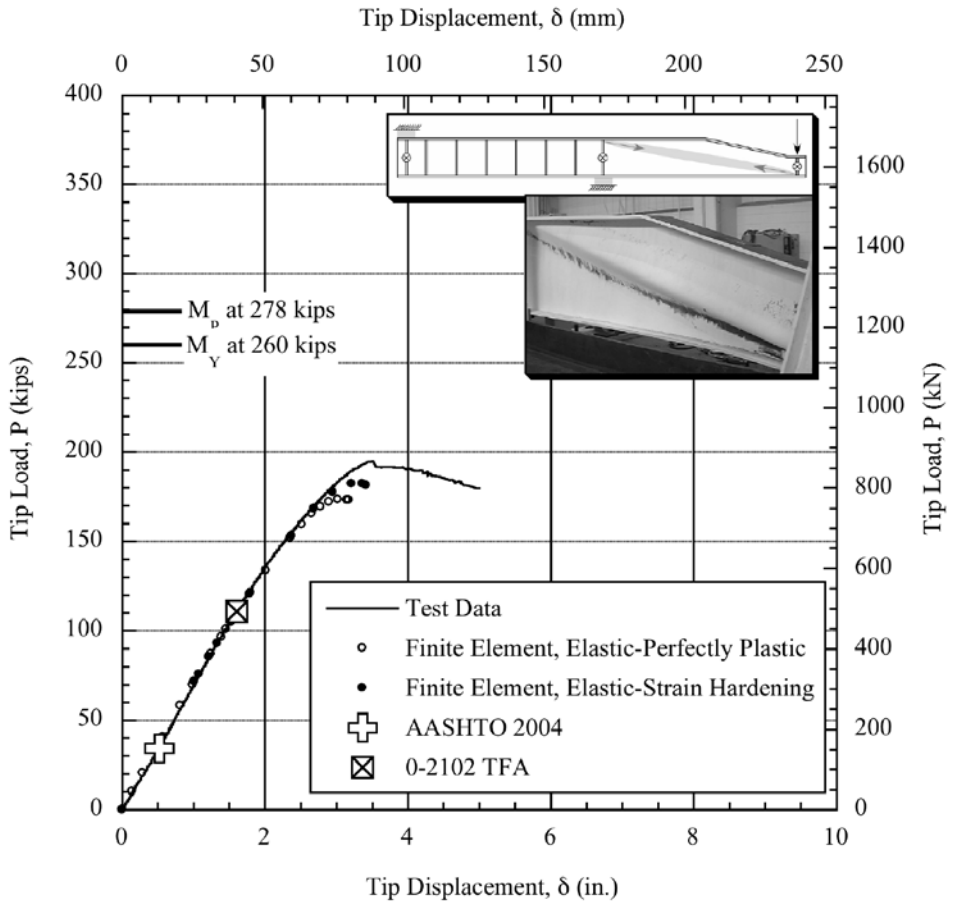

Figure 83. Plot of Tip Load versus Tip Deflection for the Unstiffened Tapered Specimen.

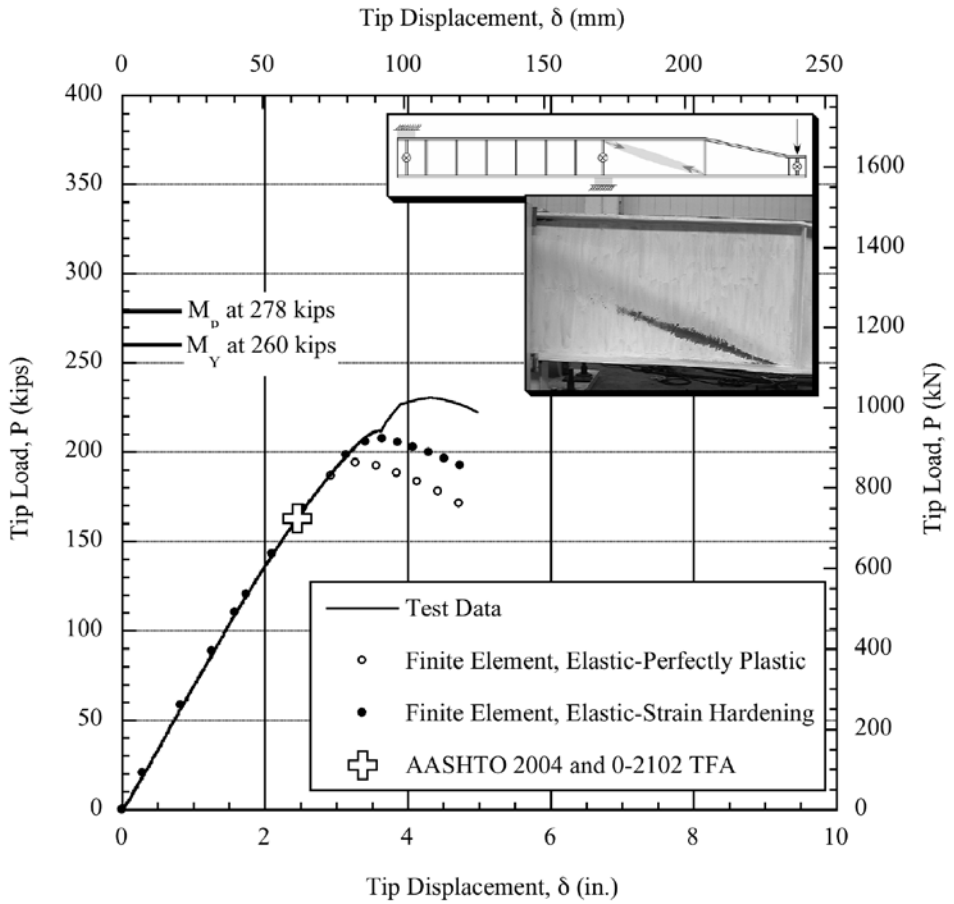

Figure 84. Plot of Tip Load versus Tip Deflection for the Stiffened Tapered Specimen.

Tables 11, 12, and 13 summarize the failure mode and strength calculations from the finite-element models and the hypothetical calculations and compare these results with the test data. Referring to Table 11, the hypothetical calculations for determining the design shear strength of unstiffened dapped details are quite acceptable, giving a factor of safety somewhat more conservative than observed with the stiffened tapered specimen. The calculations seem to reflect the behavior observed in the analyses and test.

Table 11. Comparison of Proposed Capacity Calculations and Test Results

	0-2102 Proposed		Test Results		
Specimen	Controlling Limit State	Tip Capacity (kips)	Mode of Failure	Maximum Load (kips)	Factor of Safety
90-Degree Rounded	Shear	111	Shear	190	1.71
Unstiffened Taper	Shear	111	Shear	195	1.76
Stiffened Taper	Shear	160	Shear	230	1.44

Table 12. Comparison of Elastic-Perfectly Plastic Finite Element Results and Test Results.

	Finite Element Analysis		Test Results		
Specimen	Mode of Failure	Tip Capacity (kips)	Mode of Failure	Maximum Load (kips)	Factor of Safety
90-Degree Rounded	Shear	167	Shear	190	1.14
Unstiffened Taper	Shear	174	Shear	195	1.12
Stiffened Taper	Shear	194	Shear	230	1.19

Table 13. Comparison of Elastic-Strain Hardening Finite Element Results and Test Results.

	Finite Element Analysis		Test Results		
Specimen	Mode of Failure	Tip Capacity (kips)	Mode of Failure	Maximum Load (kips)	Factor of Safety
90-Degree Rounded	Shear	176	Shear	190	1.08
Unstiffened Taper	Shear	182	Shear	195	1.07
Stiffened Taper	Shear	207	Shear	230	1.11

SUPPLEMENTAL ANALYSIS OF ALTERNATIVE SPECIMENS WITH 0.5-IN. WEBS

Procedures

Another set of finite element analyses was executed to examine the behavior of the test specimens if they had contained 0.5-in. webs. Such specimens were not tested as part of the project. The details of the analyses are identical to those described for the 0.25-in. webs. In addition, AASHTO design calculations and "hypothetical" design calculations were performed as described before. For reference purposes, the yield moment and plastic moment capacities for these specimens are 6830 and 7620 ft-kips, respectively. Therefore, the load that will cause flexural yielding is approximately 285 kips, and, ignoring the effects of strain hardening, the load that will cause plastic hinging is approximately 320 kips.

Results

Table 14 provides a summary of the results of the analyses. Contour plots of the von Mises yield function stresses and renderings of the deformed shape of each specimen at ultimate load appear in Figures 85, 86, and 87. Referring to the deformed shape plots, at ultimate loading conditions, there is no evidence of excessive web plate buckling as was observed with the thin 0.25-in. web plate. In fact, the stress contour patterns indicate that a plastic hinge has formed

over the interior support. The numbers reported in Table 14 support that conclusion. For each of the three specimens with a 0.5-in. web plate, whether stiffened or not, the finite element results indicate that the ultimate failure mode was plastic collapse in flexure over the interior support. Observing from the previous analyses for the 0.25-in web specimens, researchers assumed that the elastic-strain hardening models would give a good approximation to the qualitative and quantitative behavior of hypothetical test specimens. In the following discussions, therefore, the results of the strain-hardening models are presumed to be representative of test data had they been obtained.

Table 14. Summary of Finite Element Results for Girders with 0.5-in. Thick Webs.

Dapped Detail	Elastic-Perfectly Plastic Ultimate Load (kips)	Strain Hardening Ultimate Load (kips)
Unstiffened 90-Degree Rounded	316.9	343.9
Unstiffened Tapered	318.5	344.0
Stiffened Tapered	316.1	343.7

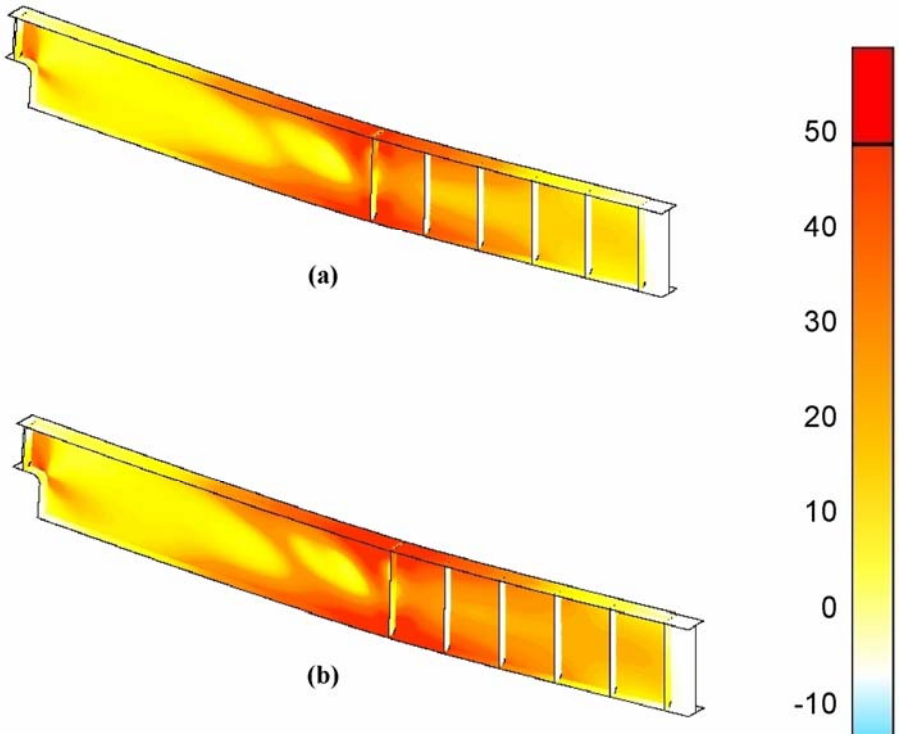

Figure 85. Von Mises Stresses Superimposed over the Deformed Shape of the Unstiffened 90-Degree Rounded Specimen with 0.5-in. Thick Web. Stresses Are Plotted at the Ultimate Load Step for (a) Elastic-Perfectly Plastic and (b) Strain Hardening Materials.

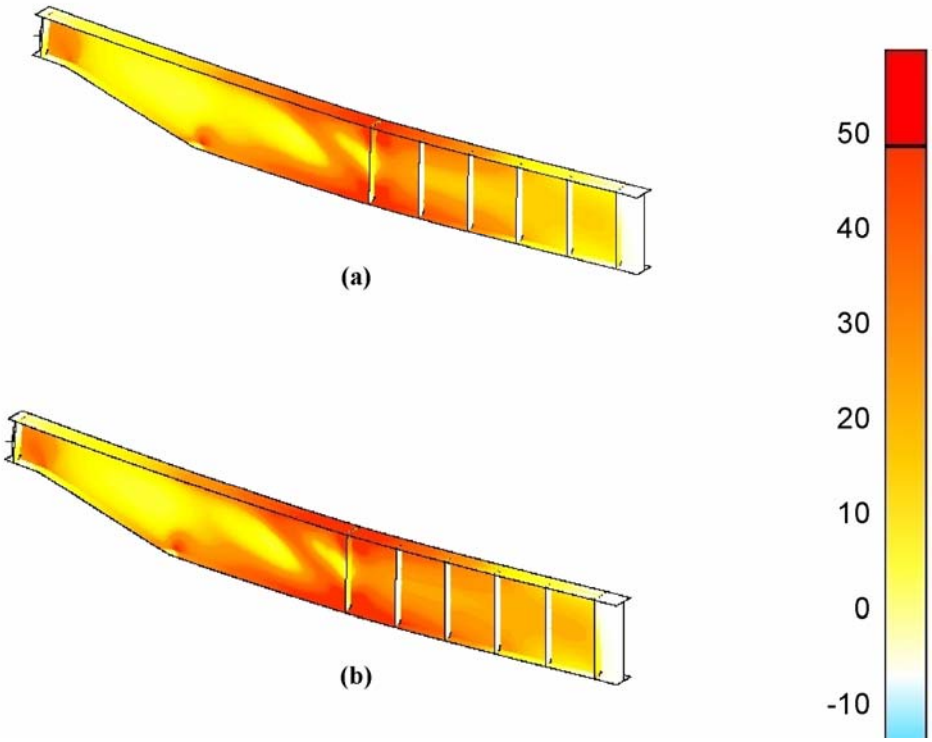

Figure 86. Von Mises Stresses Superimposed over the Deformed Shape of the Unstiffened Tapered Girder with 0.5-in. Thick Web. Stresses Are Plotted at the Ultimate Load Step for (a) Elastic-Perfectly Plastic and (b) Strain Hardening Materials.

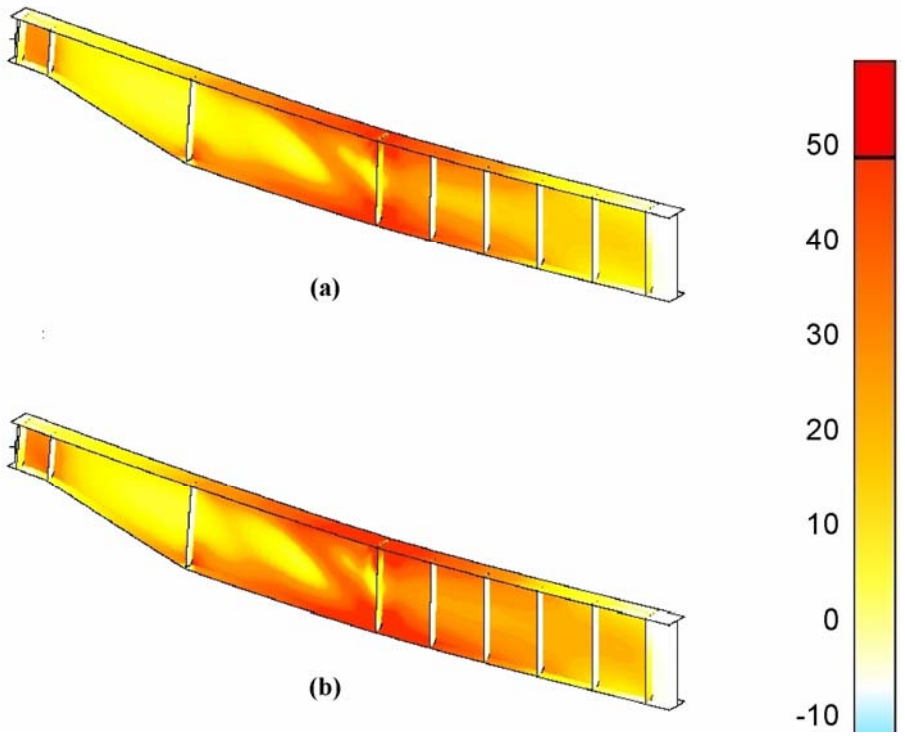

Figure 87. Von Mises Stresses Superimposed over the Deformed Shape of the Stiffened Tapered Girder with 0.5-in. Thick Web. Stresses Are Plotted at the Ultimate Load Step for (a) Elastic-Perfectly Plastic and (b) Strain Hardening Materials.

Tables 15 and 16 summarize the failure mode and strength calculations based on the AASHTO specifications and hypothetical calculations, respectively. The calculations are compared with results from the finite-element models. The "factor of safety" label on the last column is especially suspect now, since there are no test data, but it is retained as a useful means of comparing the calculation methods. As before, for the stiffened specimen, the specifications seem to provide a very good basis for both anticipating the ultimate behavior of the specimen and for determining an appropriate design strength value for the specimen. For the unstiffened specimens, the specifications do not capture the behavior very well. This time, the factor of safety is not so different among the cases considered; rather, the issue is economics. By analysis, the unstiffened specimens easily developed the yield moment of the section. In fact, all specimens "failed" by plastic collapse over the interior support. According to the current AASHTO provisions, however, the unstiffened specimens have too little shear capacity to plastify the section. This would lead a designer to add transverse stiffeners, when they are probably not needed, and add unnecessary cost to the project. Table 17 is a summary comparison

of shear force capacity calculations using AASHTO 2004 and the hypothetical calculations described above. The hypothetical calculations take advantage of the ability of the recessed end of the dap to anchor a tension field from an adjacent span. In addition, the calculations acknowledge the ability of a wide unstiffened span, up to 24 ft, to develop a full tension field.

Table 15. Comparison of AASHTO 2004 Capacity Calculations and Finite Element Results.

	AASHTO 2004		Analysis Results		
Specimen	Controlling Limit State	Tip Capacity (kips)	Mode of Failure	Maximum Load (kips)	Factor of Safety
90-Degree Rounded	Shear	275	Flexure	344	1.25
Unstiffened Taper	Shear	275	Flexure	344	1.25
Stiffened Taper	Flexure	284	Flexure	344	1.21

Table 16. Comparison of Proposed Capacity Calculations and Finite Element Results.

	0-2102 Proposed		Analysis Results		
Specimen	Controlling Limit State	Tip Capacity (kips)	Mode of Failure	Maximum Load (kips)	Factor of Safety
90-Degree Rounded	Flexure	284	Flexure	344	1.21
Unstiffened Taper	Flexure	284	Flexure	344	1.21
Stiffened Taper	Flexure	284	Flexure	344	1.21

Table 17. Shear Force Capacity Calculation Results.

	AASHTO 2004		0-2102 Proposed	
Specimen	Limit State	Nominal Capacity (kips)	Limit State	Nominal Capacity (kips)
90-Degree Rounded	Shear	275	Shear	398
Unstiffened Taper	Shear	275	Shear	398
Stiffened Taper	Shear	457	Shear	457

ULTIMATE STRENGTH ANALYSIS PART III: LOCAL STRESSES

The previous analyses provided insight into the global behavior of the round and tapered dapped details. However, concerns over fatigue behavior, particularly of the round detail, warranted further investigation. For that reason, a series of finite-element models focused on

behavior local to the dapped region. These models were refinements of the five model geometries previously described, the rounded and tapered girders with 0.5-in. thick webs.

Procedures

In Chapter 2, a technique called submodeling was described. It was used again here to investigate the local states of stress in various rounded and tapered details at static ultimate loading conditions and static service loading conditions. Specifically, the effects of stiffener placement were investigated. Five ultimate strength analyses were conducted to link the global results for the rounded and tapered details, with 0.5-in. thick webs, to local models of the appropriate dapped regions. These local models included the dapped end and an adjacent portion of the full-depth web considered sufficient to capture relevant stress-concentration effects. For the sake of completeness, the following list describes the dapped details examined:

- rounded dapped region, with no intermediate stiffeners;
- rounded dapped region, with a vertical intermediate stiffener;
- rounded dapped region, with both a vertical and diagonal intermediate stiffener;
- tapered dapped region, with no intermediate stiffeners; and
- tapered dapped region, with intermediate stiffeners.

The local models used to capture the behavior of these dapped regions are presented in Figures 88 and 89. Parents of these models were originally created as part of the case-study bridge analysis described in Chapter 2.

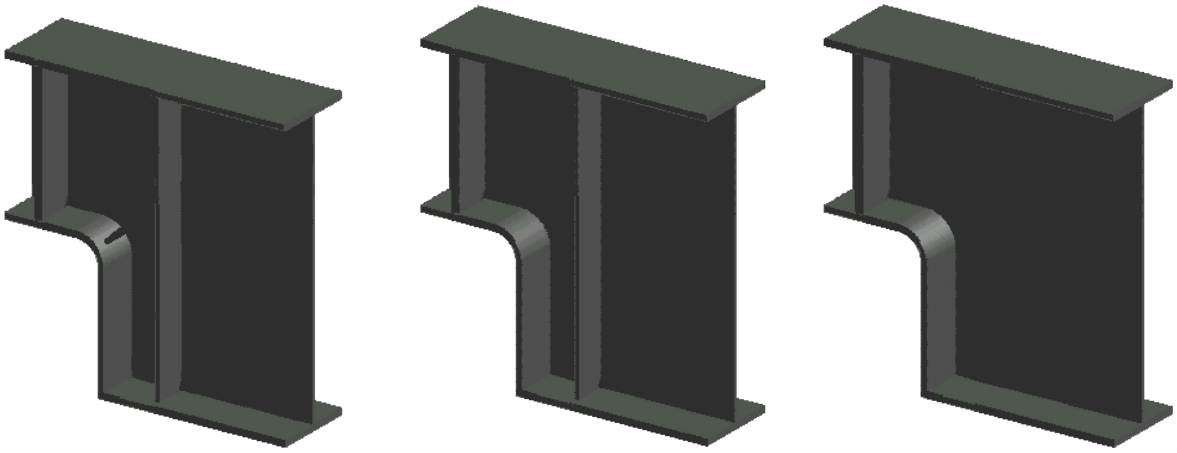

(a) (b) (c)

Figure 88. Three Local Models for Rounded Detail.

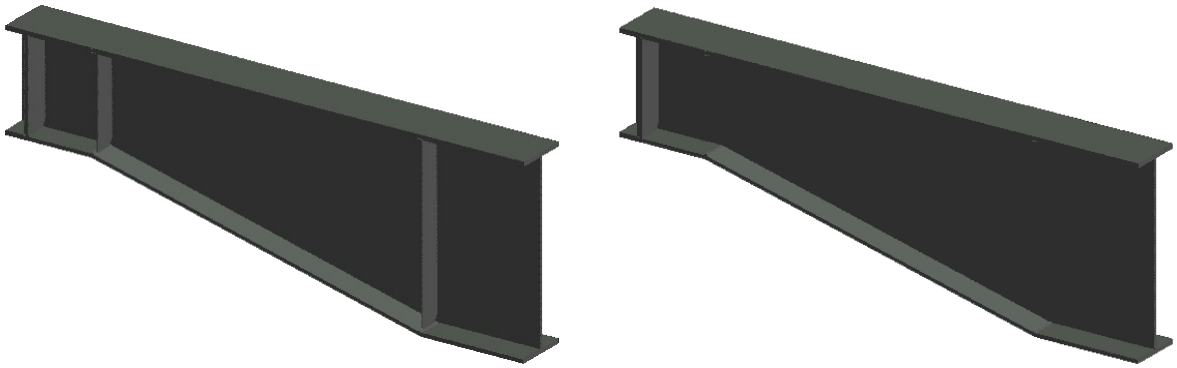

(a) (b)

Figure 89. Two Local Models for Tapered Detail.

The elastic-perfectly plastic stress-strain curve was selected for these analyses. The yield point was 50 ksi, and the modulus of elasticity was 30,000 ksi. Two sets of global analyses drove corresponding local models. The first analysis focused on ultimate strength capacity, and the second concerned realistic service loads.

The ultimate strength analysis used the Riks analyses outlined in the previous chapter. To summarize, an eigenvalue analysis introduced a geometric imperfection into the model. A Riks analysis was then performed to determine the girders' ultimate capacity. ABAQUS determined the load increments and step sizes for these analyses.

In the second set of analyses, the Riks solution was more carefully controlled. The load parameter was increased in five even increments to apply a total load of 100 kips to the girder. This load magnitude was based on the live load simulation procedure described in Chapter 2, except the WIM data used in this simulation were collected throughout 2001 from sites 502, 512, 522, 516, and 513 (as shown on the map in Figure 11 in Chapter 2). The CORSIM traffic simulation program was calibrated for the AM, PM, and off-peak period traffic on I-10, as well as for the AM peak period on US 290. A total of four simulations were run for the round dap geometry, and support reactions were gathered for I-10 and US 290 during these different times. These reactions were then examined; the maximum value of the reaction at the dapped end was approximately 90 kips. A value of 100 kips for the applied load therefore seemed likely to present a "worst-case" scenario for a static traffic loading effect. Applying a 100-kip load

facilitates a comparison of the static behavior among the dapped details under service load conditions and ultimate load conditions.

Results

Once analyzed, stress contours were made for these girders in Patran. Figures 90 through 99 display this information.

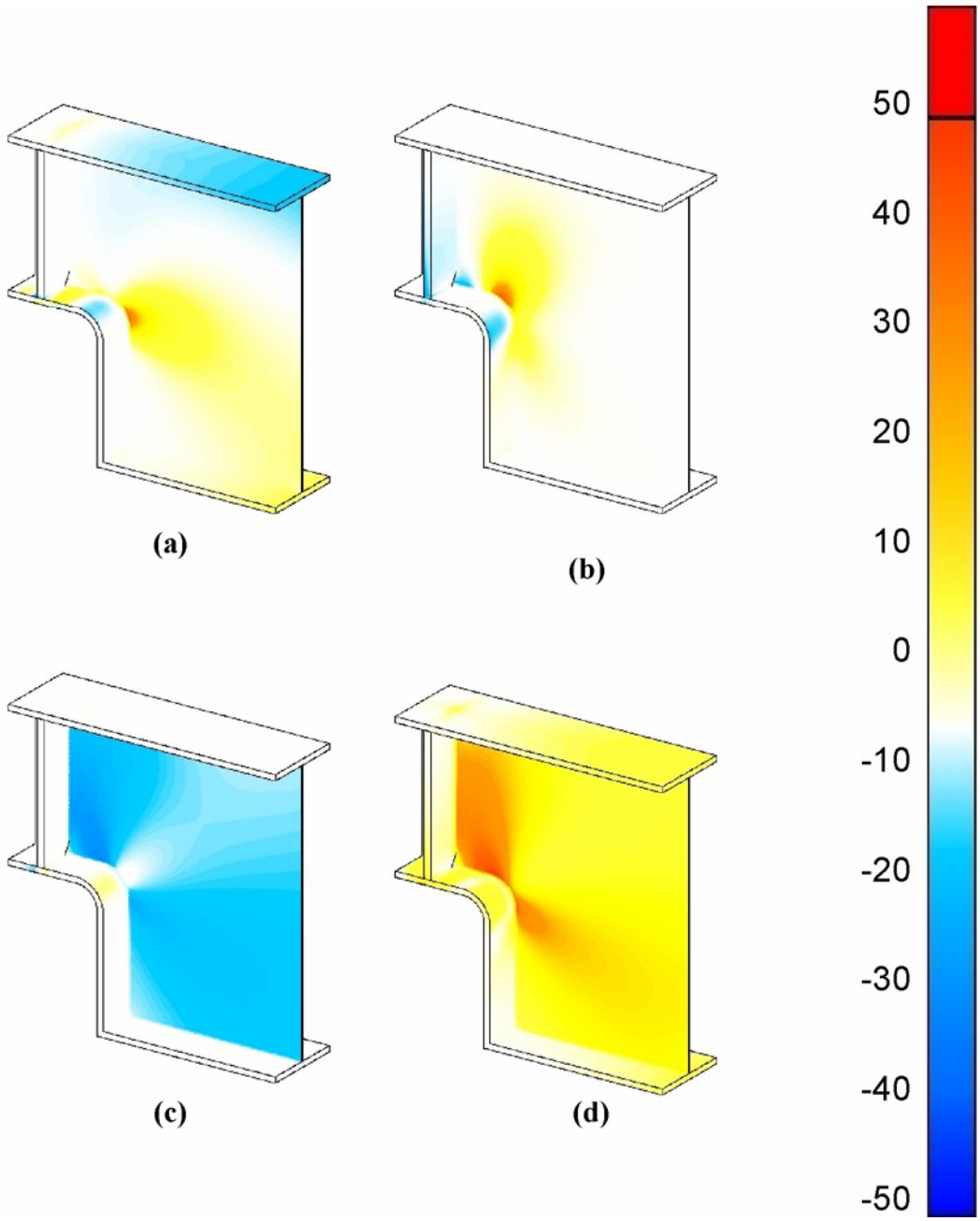

Figure 90. Stress Contour Plots of 0.5-in. Thick Web Local Models for Round Girder with No Stiffeners at Ultimate Load Capacity. (a) σ_{xx}, (b) σ_{yy}, (c) τ_{xy}, (d) von Mises Stress.

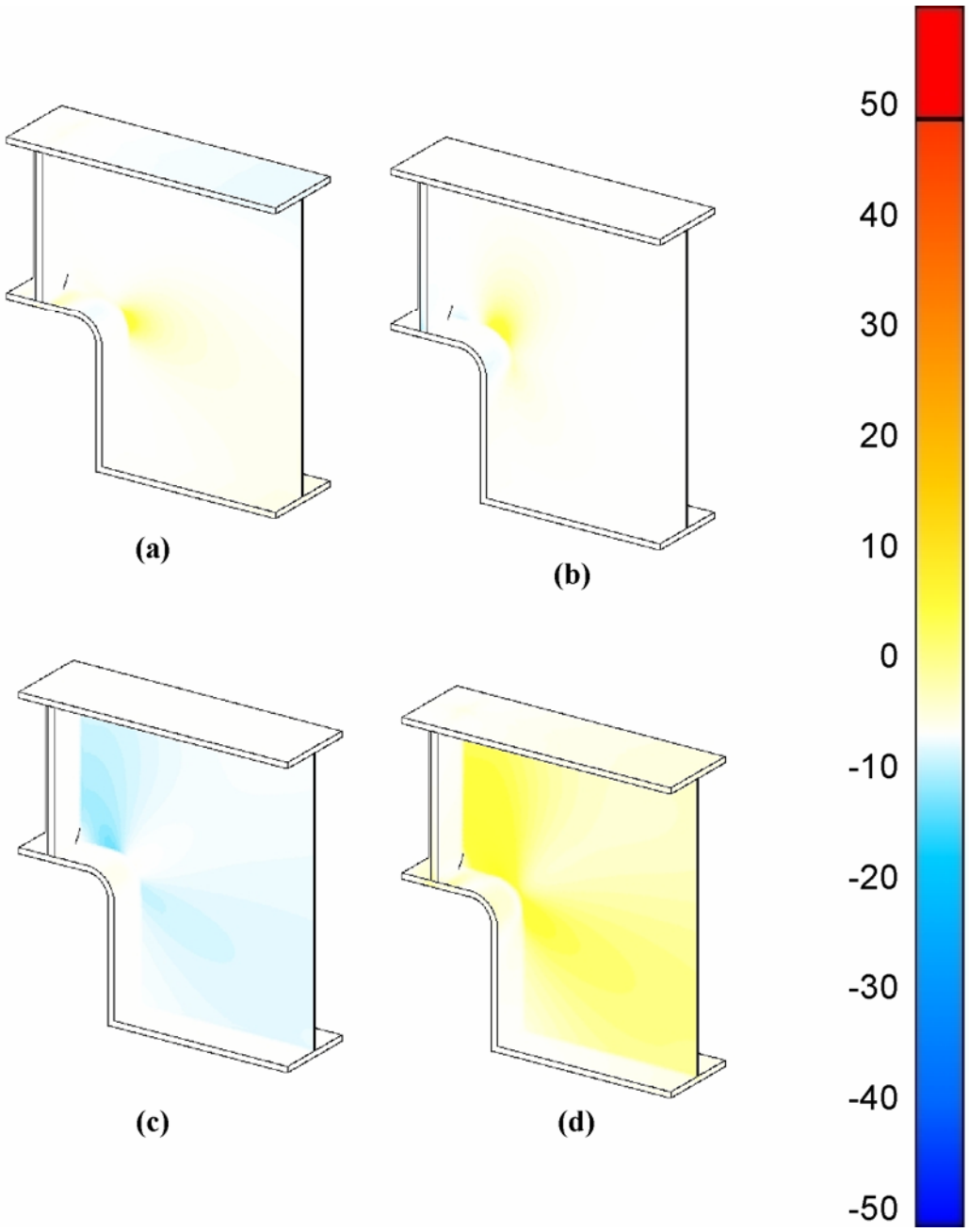

Figure 91. Stress Contour Plots of 0.5-in. Thick Web Local Models for Round Girder with No Stiffeners at 100-kip Service Load. (a) σ_{xx}, (b) σ_{yy}, (c) τ_{xy}, (d) von Mises Stress.

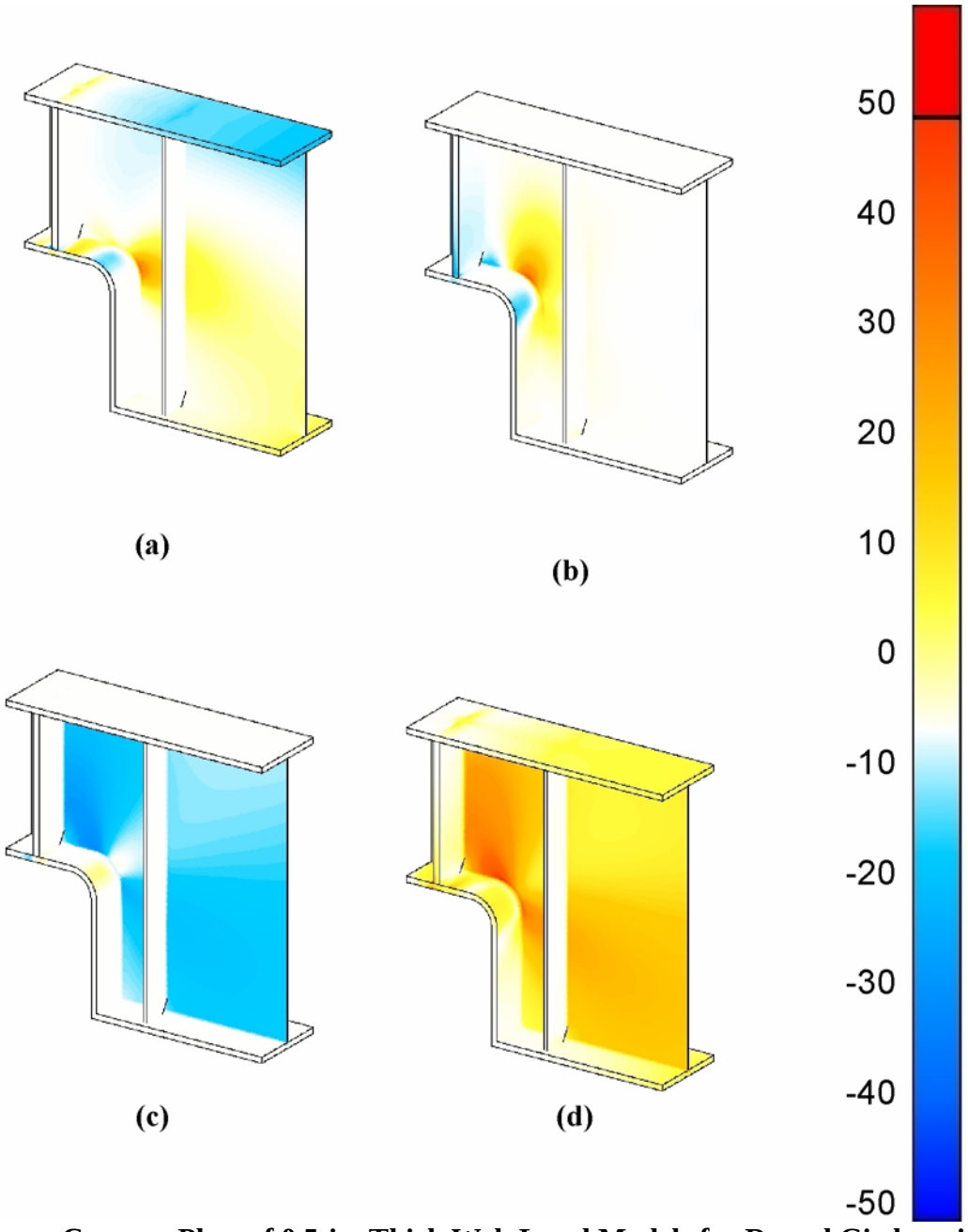

Figure 92. Stress Contour Plots of 0.5-in. Thick Web Local Models for Round Girder with Only Vertical Intermediate Stiffener at Ultimate Load Capacity. (a) σ_{xx}, (b) σ_{yy}, (c) τ_{xy}, (d) von Mises Stress.

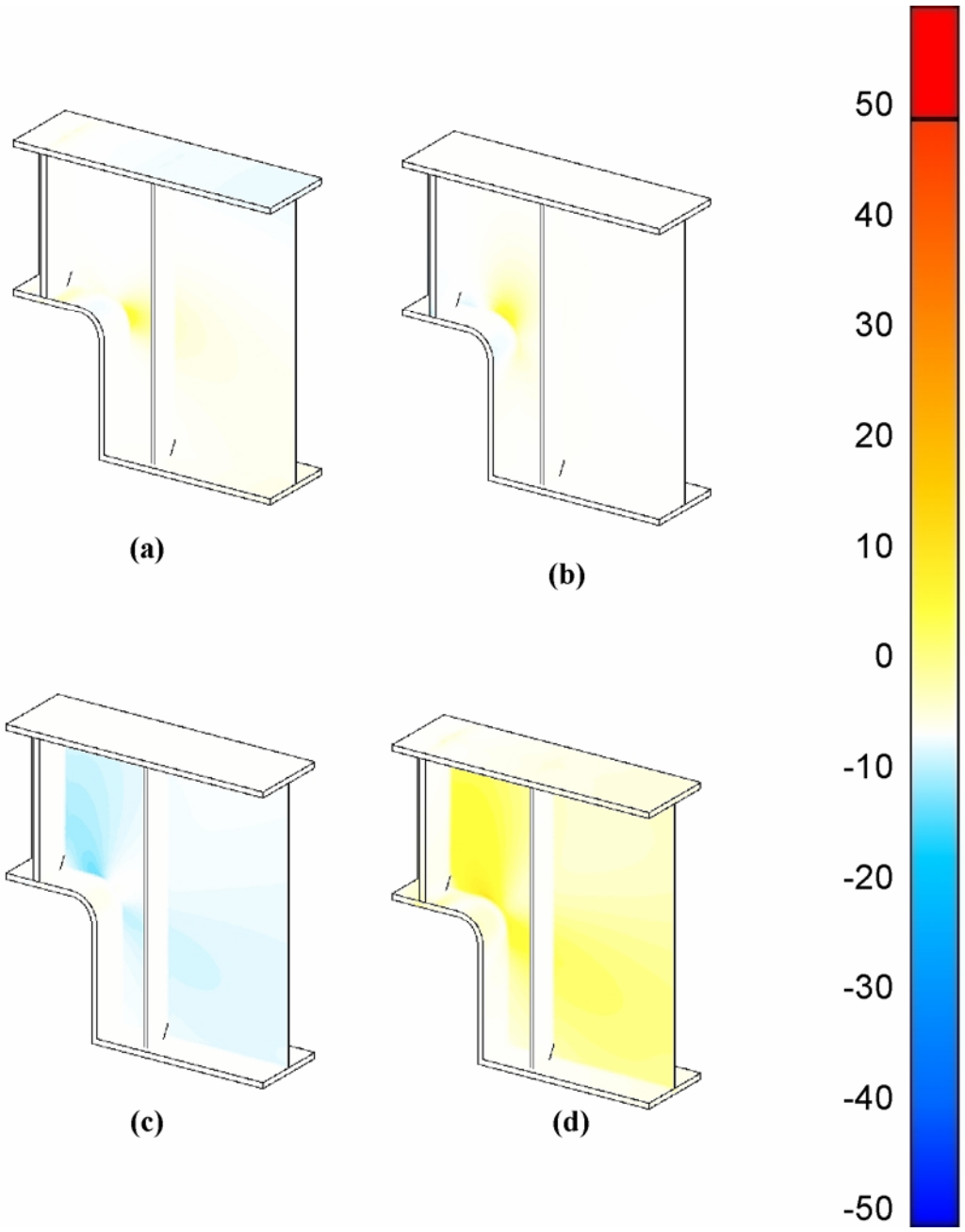

Figure 93. Stress Contour Plots of 0.5-in. Thick Web Local Models for Round Girder with Only Vertical Intermediate Stiffener at 100-kip Service Load. (a) σ_{xx}, (b) σ_{yy}, (c) τ_{xy}, (d) von Mises Stress.

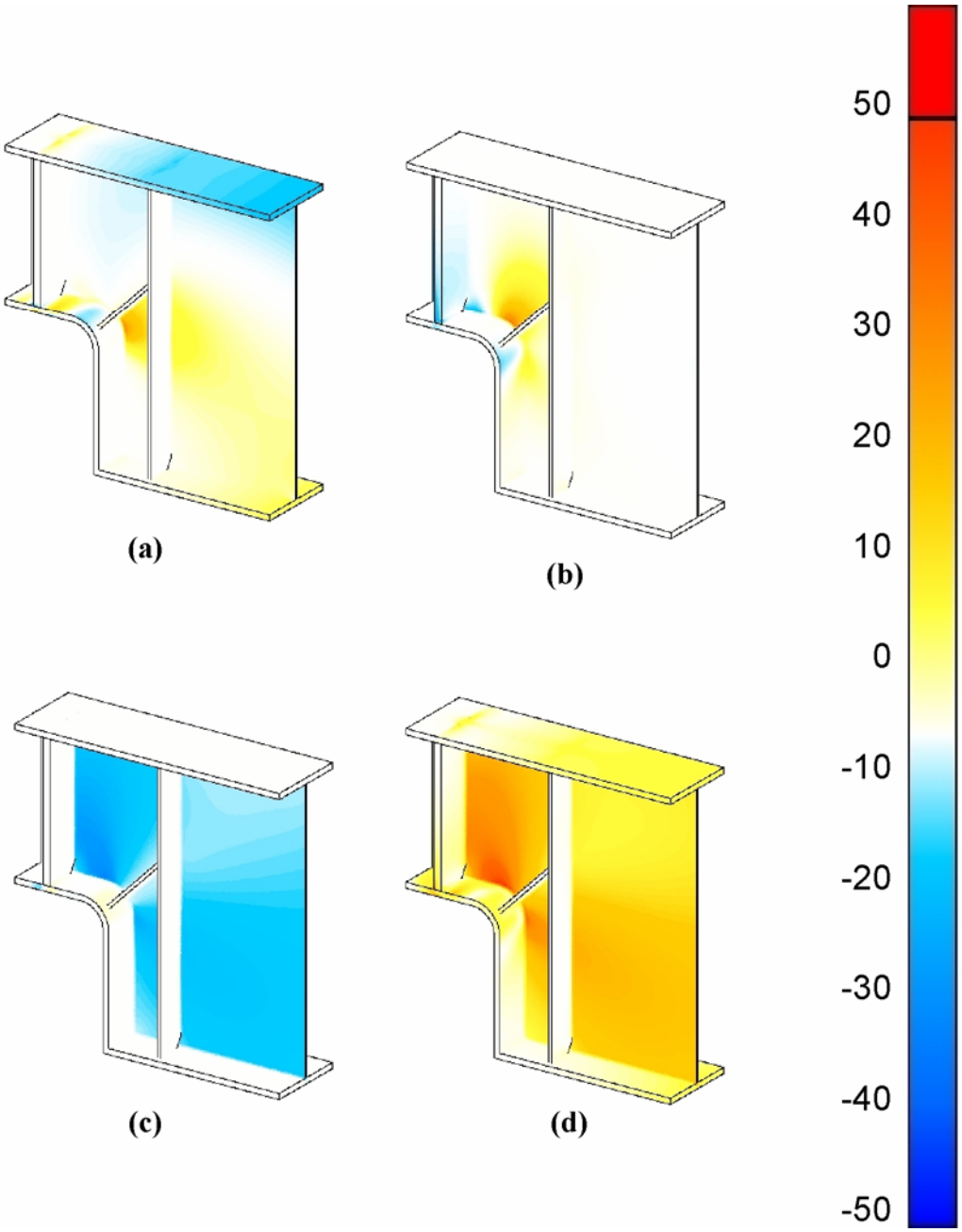

Figure 94. Stress Contour Plots of 0.5-in. Thick Web Local Models for Round Girder with Two Intermediate Stiffeners at Ultimate Load Capacity. (a) σ_{xx}, (b) σ_{yy}, (c) τ_{xy}, (d) von Mises Stress.

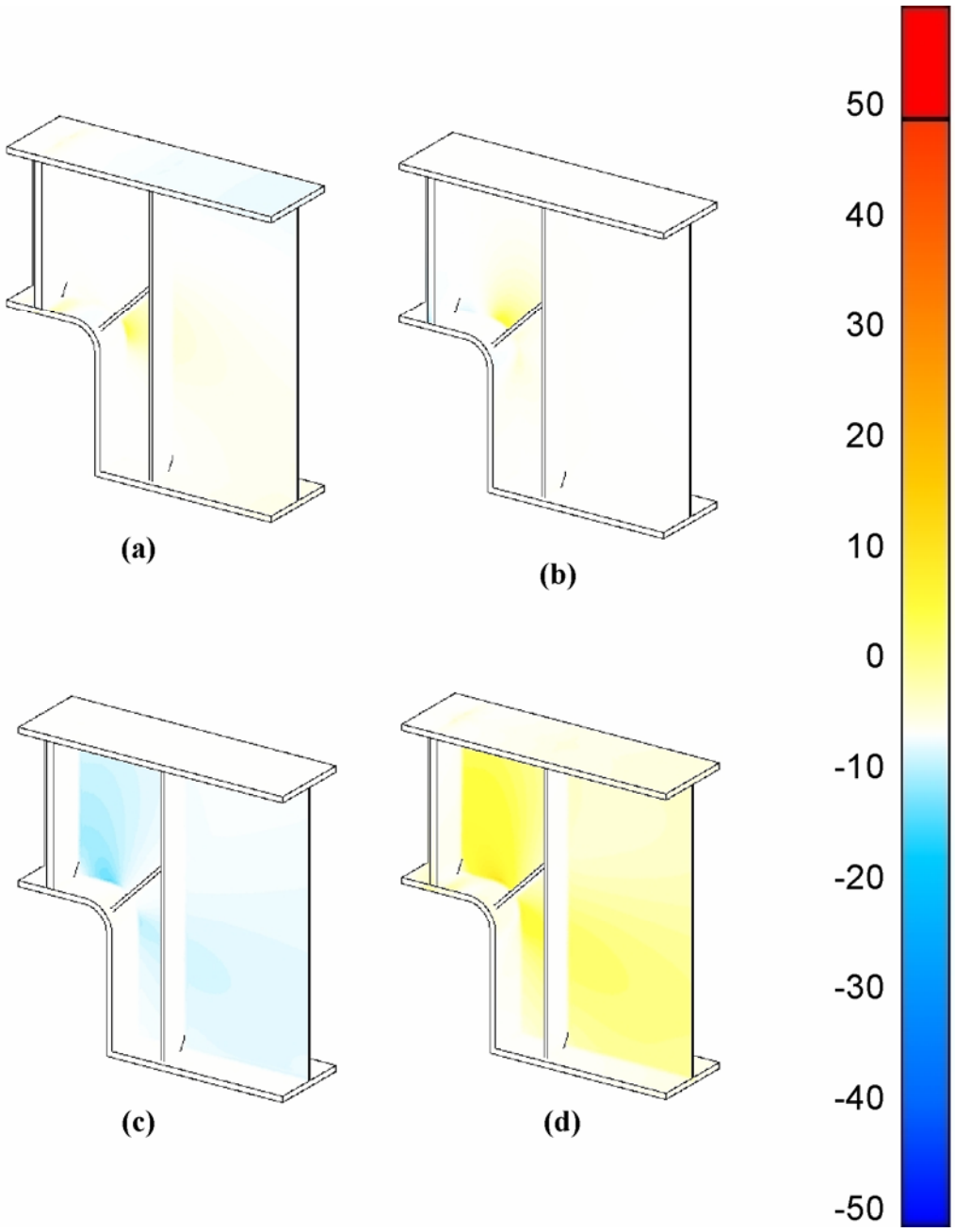

Figure 95. Stress Contour Plots of 0.5-in. Thick Web Local Models for Round Girder with Two Intermediate Stiffeners at 100-kip Service Load. (a) σ_{xx}, (b) σ_{yy}, (c) τ_{xy}, (d) von Mises Stress.

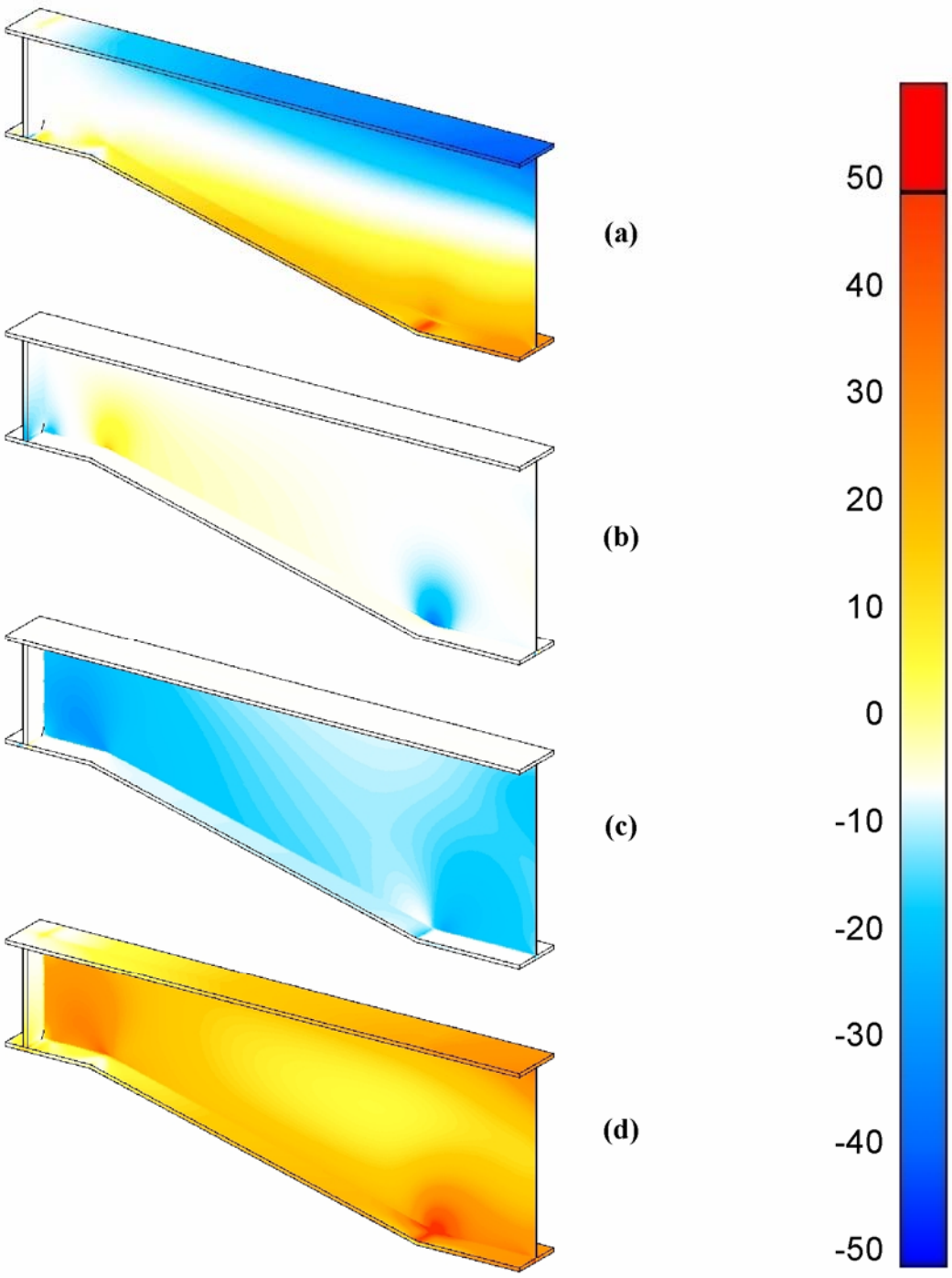

Figure 96. Stress Contour Plots of 0.5-in. Thick Web Local Models for Tapered Girder with No Stiffeners at Ultimate Load Capacity. (a) σ_{xx}, (b) σ_{yy}, (c) τ_{xy}, (d) von Mises Stress.

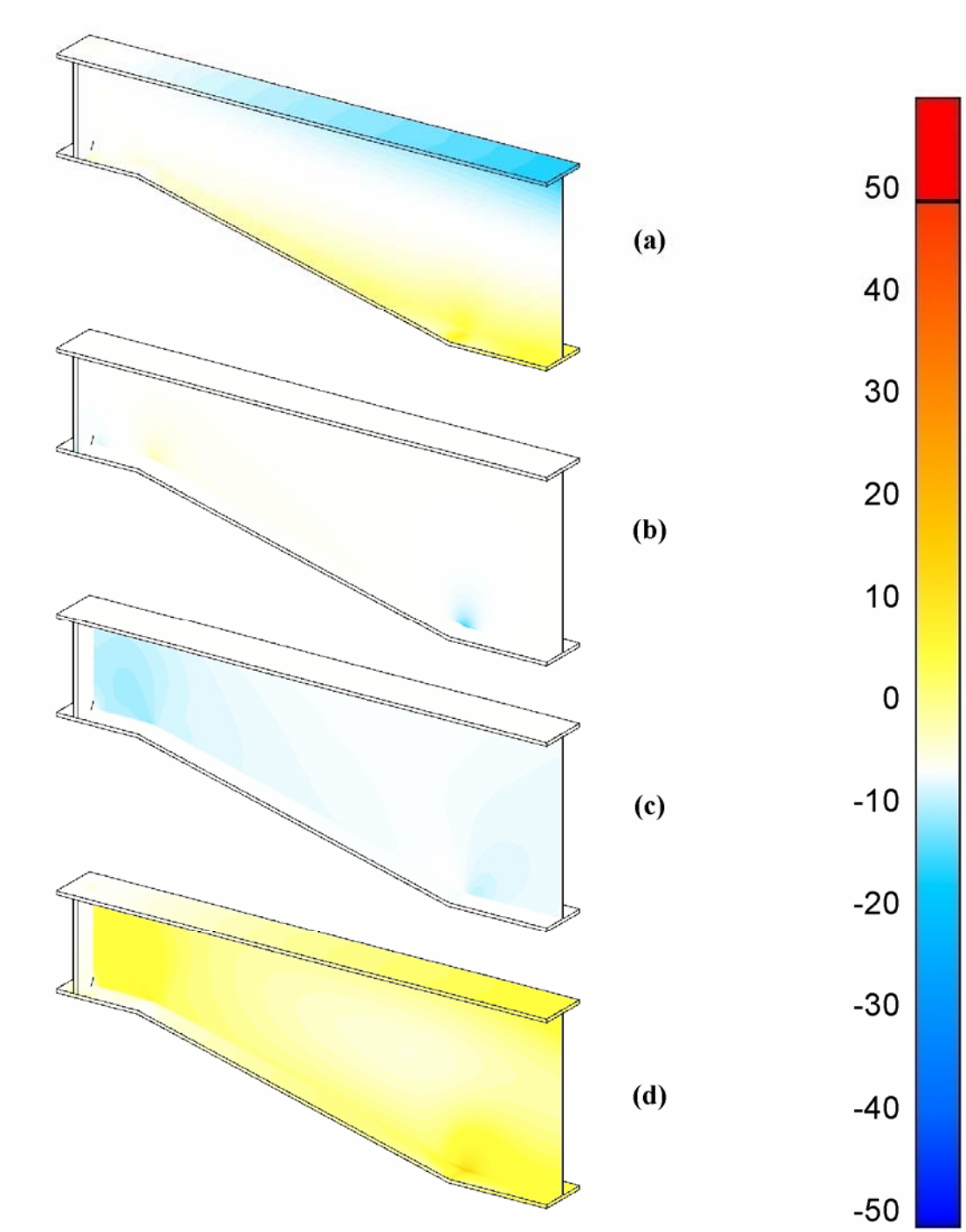

Figure 97. Stress Contour Plots of 0.5-in. Thick Web Local Models for Tapered Girder with No Stiffeners at 100-kip Service Load. (a) σ_{xx}, (b) σ_{yy}, (c) τ_{xy}, (d) von Mises Stress.

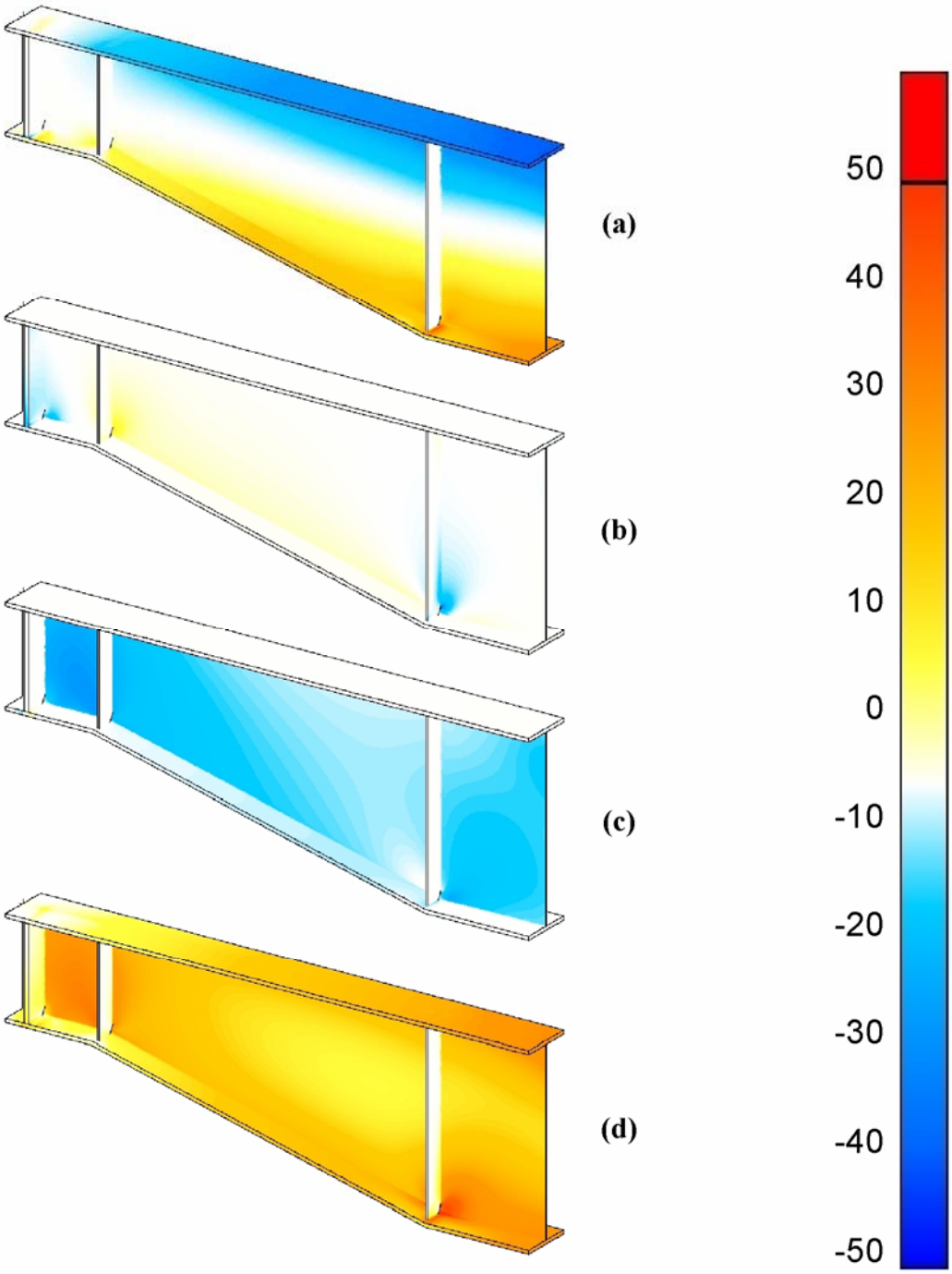

Figure 98. Stress Contour Plots of 0.5-in. Thick Web Local Models for Tapered Girder with Intermediate Stiffeners at Ultimate Load Capacity. (a) σ_{xx}, (b) σ_{yy}, (c) τ_{xy}, (d) von Mises Stress.

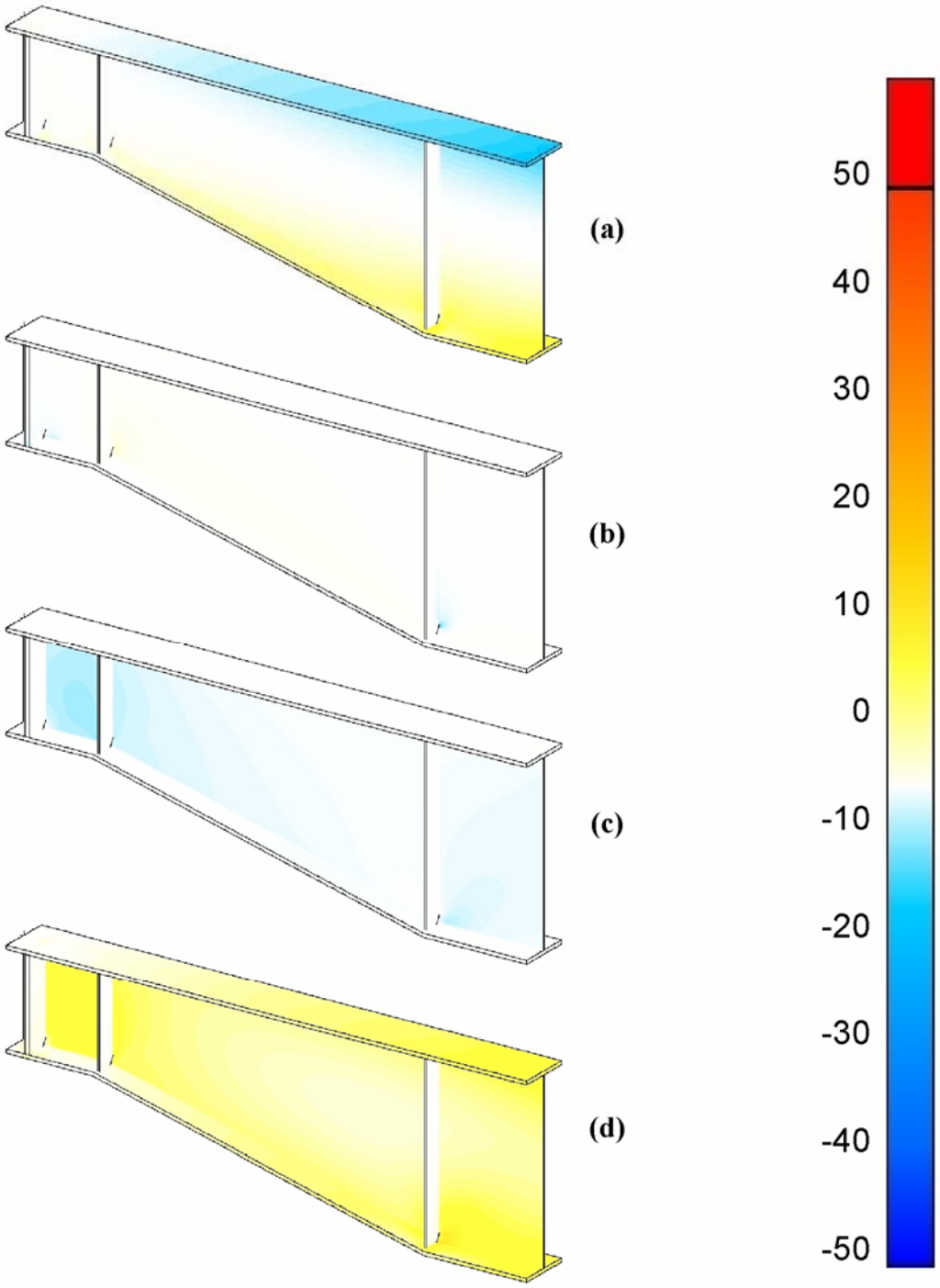

Figure 99. Stress Contour Plots of 0.5-in. Thick Web Local Models for Tapered Girder with Intermediate Stiffeners at 100-kip Service Load. (a) σ_{xx}, (b) σ_{yy}, (c) τ_{xy}, (d) von Mises Stress.

CHAPTER 5:
DAPPED GIRDER END FATIGUE FAILURES IN JAPAN

CHAPTER OVERVIEW

In Japan a dapped girder is usually referred to as a "cut-off" girder. Since the early 1960s, dapped steel girders have been used widely in Japan; a common application has been the 90-degree rounded detail. Since the mid-1970s, hundreds of instances of fatigue cracking have been reported in Japan involving this detail. A summary of this issue has been assembled with the substantial assistance of Japanese highway officials and Japanese researchers who have worked on the problem.

EXAMPLE OF FAILURE

Figure 100 is a photograph of branched fatigue cracks in a 90-degree rounded dapped detail. The photograph was taken in 1979 after the girder had been in service for approximately 15 to 20 years. The holes visible at the ends of the fatigue cracks were drilled to inhibit further propagation of the cracks. This type of cracking behavior is typical. Generally, the cracks initiate at either the root or the toe of a fillet weld where the weld joins the web plate to the curved portion of the bent flange plate. Subsequently, the cracks propagate within the web vertically and also within the web around the bent flange. The flange plate itself remains completely undamaged. Consider the stress contour plots in Figure 90 (a) and (b). By analysis, two zones of local tensile stress concentration are observed in the web plate where it joins the curved flange plate: one is located between the apex of the bend and the horizontal tangent point, and the other between the apex of the bend and the vertical tangent point. At both locations, the maximum principal stress is tensile and nearly perpendicular to the weld joining the web plate to the flange plate. One can observe that the cracks shown in Figure 100 initiated and are propagating in this zone of tensile stress concentration.

Figure 100. Fatigue Cracks in 90-Degree Rounded Detail in Japan.

ANALYSIS OF FAILURE

Figures 101 and 102 are photographs of a macroscopic specimen taken from a damaged 90-degree rounded detail. The cracking observed in this specimen is similar to that seen in Figure 100, though the specimen is not taken from that beam. Figures 103 and 104 show photomacrographs of different sections from the specimen in Figures 101 and 102. The sections shown have been polished and etched. The fillet welds are clearly visible in these macrographs, as are the heat-affected zones in the base metal. At section 1-C, seen in the bottom left of Figure 103, a fatigue crack is visible at the toe of the right-hand-side fillet weld. At section 1-D, seen in Figure 104, the crack has completely severed the web plate. At section 3-D, seen in Figure 104, another toe crack is visible. Figure 105 is a scanning electron microscope image of the crack initiation site on the fracture surface. The direction of crack propagation is indicated by an arrow in the image on the right-hand side of Figure 105.

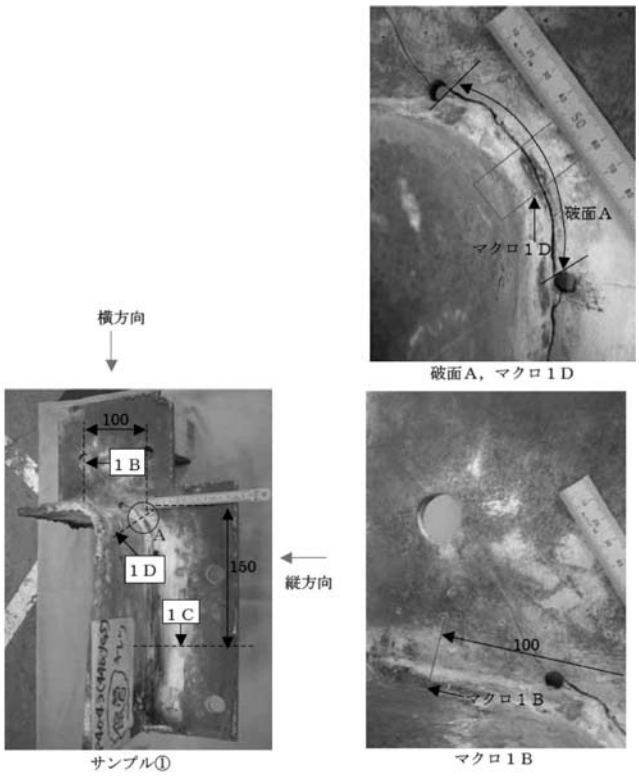

Figure 101. Macroscopic Specimen from 90-Degree Rounded Detail with Fatigue Cracks.

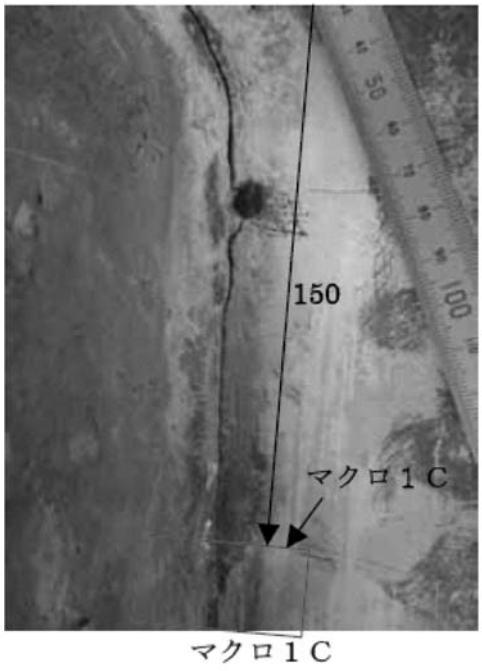

Figure 102. Closeup View of Area 1-C in Macroscopic Specimen.

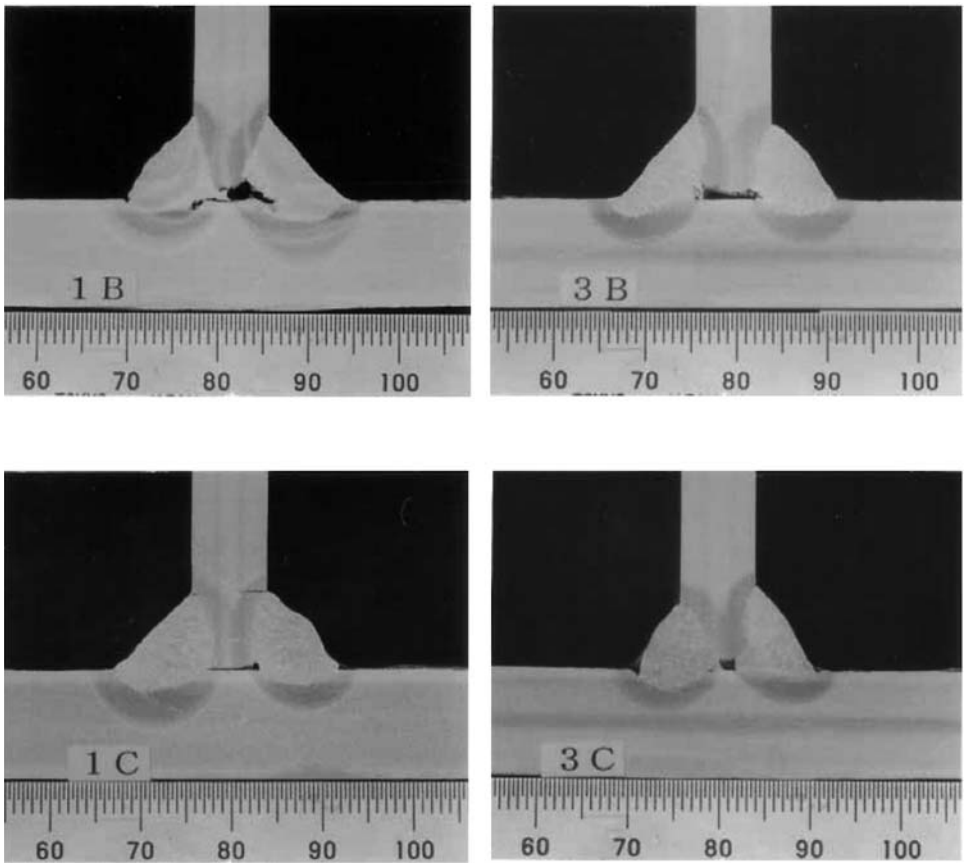

Figure 103. Photomacrographs of Etched Samples 1 and 3 (1-B, 1-C, 3-B, and 3-C).

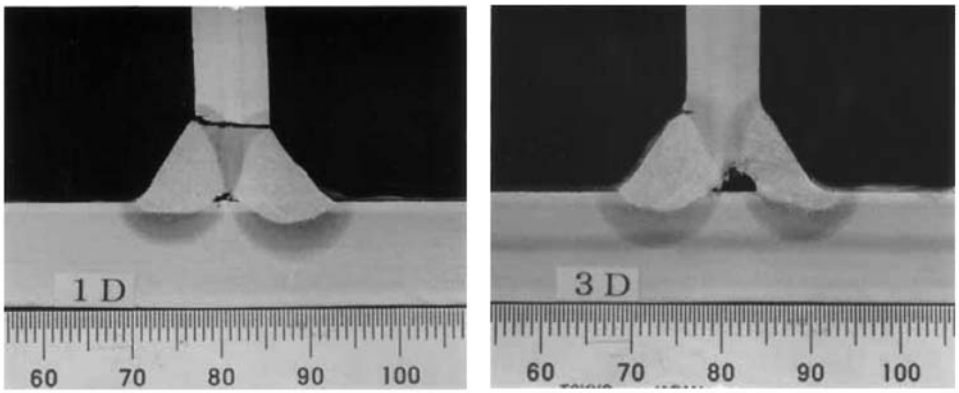

Figure 104. Photomacrographs of Etched Samples 1 and 3 (1-D and 3-D).

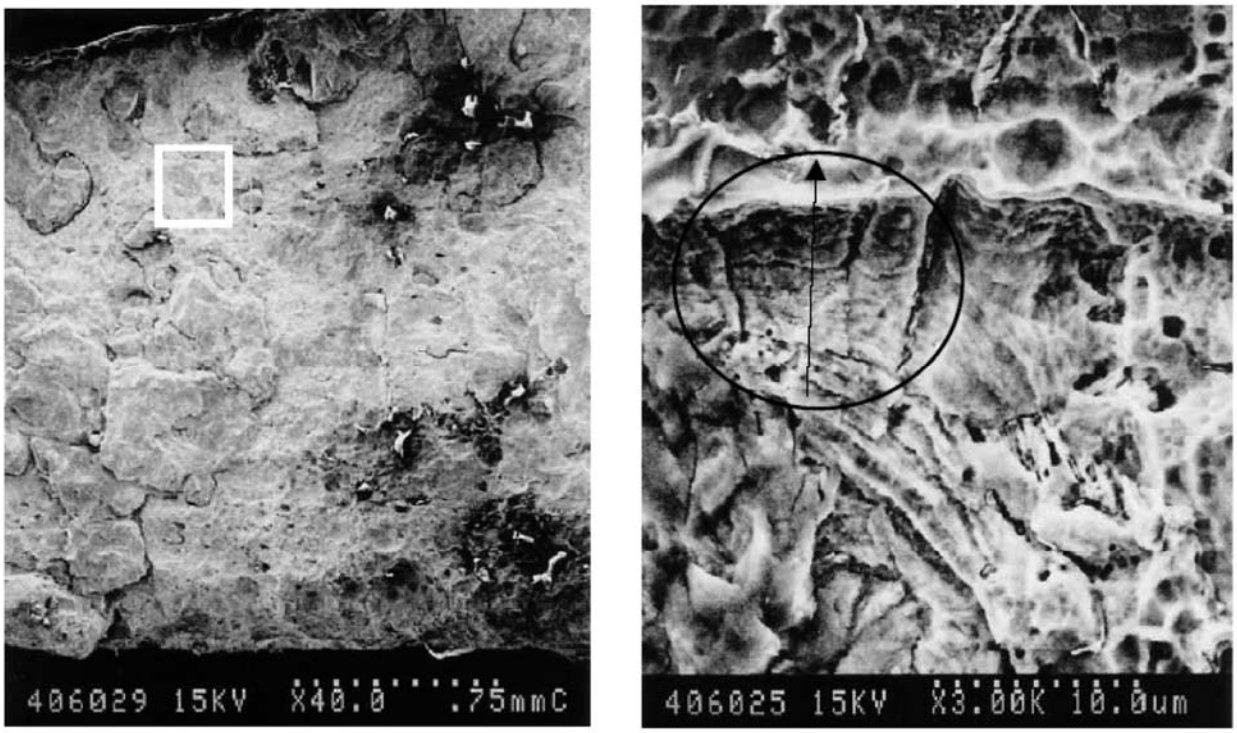

Figure 105. Scanning Electron Microscope Image of Fracture Surface.

REPAIR AND RETROFIT APPLICATIONS

Following the initial discovery of the cracks, analytical and experimental studies, including field tests, were conducted to determine the essential causes of the cracking. A recent summary of several fatigue applications in Japanese steel bridges is available in English (*22*). The studies suggested four potential contributing factors including the following: fabrication errors; interruption of the natural flow of stresses because of the 90-degree bend, thereby causing an unanticipated stress concentration; local out-of-plane distortions of the beam web; and inadequate rotation capacity of the beam seats because of corrosion (see Figure 106).

Figure 106. Corrosion of Beam Seat.

Several different repair and retrofit strategies have been adopted to mitigate the deficiencies identified in the studies. Thick coverplates were bolted to the webs to cover the cracks and provide an alternative load path for the beam-end shear force (see Figure 107). To mitigate the stress concentration effect (i.e., improve the natural flow of stress around the 90-degree bend), diagonal rib plates were attached to the webs to establish a stiff load path, bypassing the cracks (see Figure 108). To mitigate out-of-plane web distortions, stiff horizontal bracing elements were installed at the beam ends (see Figure 109). It is not clear if any measures were taken to improve the performance of the beam seats.

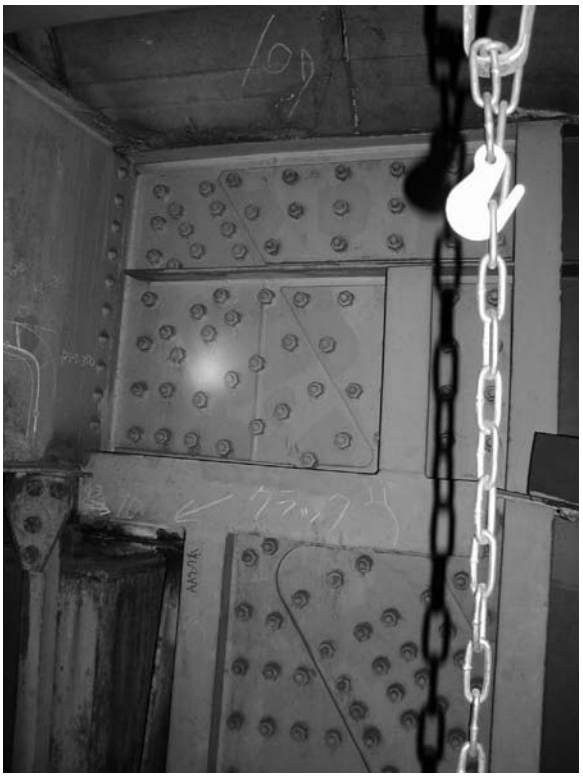

Figure 107. Coverplate Retrofit for Cracked Girder Web.

Figure 108. Diagonal Rib Installed to Improve Load Path.

Figure 109. Rib and Lateral Brace Used to Reduce Out-of-Plane Bending.

SUMMARY

In 1999, inspections determined that many fatigue cracks continued to propagate through the stop holes and beyond, despite the repairs and retrofits that had been executed in the early 1980s (e.g., see Figure 110). In 2002 a new program of construction activities commenced to repair and retrofit bridges in response to a mounting number of issues related to fatigue and seismic performance. As part of that project the dapped girders are being raised and their old supports, which also contained fatigue cracks, are being removed. New supports are being installed at a lower elevation. The cracked dap end is cut out (see Figure 111), and a new piece without a recess is attached as a bolted splice, to make the beam straight ended, and the beam is lowered onto its new support. This specific type of retrofit is not common and resulted because of the combined damage occurring in the dapped web and the short, cantilevered support bracket for the beam. There are reports in Japanese that describe other, perhaps more common, strategies for repair and retrofit of the dapped girders.

Figure 110. Fatigue Crack That Continued to Propagate after Retrofit.

Figure 111. Dap End Removed; New Support in Place for Straight Beam.

CHAPTER 6:
CONCLUSIONS

The results of this investigation support several conclusions that have relevance to the design of dapped girder ends in steel bridge structures.

ULTIMATE STRENGTH CONSIDERATIONS

- Each of the dapped girder end details considered in this project is able to develop a full tension field following shear buckling of the web plate. This includes cases in which the tension field occurs within the end panel and also cases in which the end panel is tapered.
- The ability of a dapped detail to anchor an end-panel tension field is attributable to the increased compactness of the web plate in the vicinity of the support.
- The ultimate strength behavior of girders that incorporate a 90-degree rounded detail is the same as otherwise identical girders that incorporate a 4:1 tapered detail. Hence, special intermediate stiffeners installed at flange bend locations in tapered details may not be necessary.
- When calculating the shear capacity of a tapered panel, it is conservative to assume the panel is of a uniform depth that is equal to the maximum depth of the panel.
- In light of the statements above, when a dapped detail is used, it may be possible to eliminate one or more sets of intermediate transverse stiffeners near the end of the girder.

FATIGUE CONSIDERATIONS

Notched Details

- By analysis, among the three dapped details considered in this project, notched details possessed the lowest fatigue strength.
- By analysis, two zones of local stress concentration were observed: at the reentrant corner of the notch and in the web plate at the end of the extended horizontal flange plate.

- During fatigue testing under simulated service loading, the notched detail developed a fatigue crack in the web at the end of the extended horizontal flange plate.
- At the time of this report, the project supervisor is not aware of instances where fatigue cracks have formed in notched details in service.

90-Degree Rounded Details

- By analysis, 90-degree rounded details possess intermediate fatigue strength when compared to notched details and tapered details.
- By analysis, two zones of local tensile stress concentration are observed in the web plate where it joins the curved flange plate: one is located between the apex of the bend and the horizontal tangent point and the other between the apex of the bend and the vertical tangent point. At both locations, the maximum principal stress is tensile and nearly perpendicular to the weld joining the web plate to the flange plate.
- By analysis, at service load levels, the addition of welded transverse stiffener plates that join the apex of the bent flange to the web neither increases nor reduces the local concentrations of stress.
- During fatigue testing under simulated service loading, the 90-degree rounded detail did not develop fatigue cracks.
- In Japan the 90-degree rounded detail has been used extensively for more than 40 years. For more than 20 years, this detail has been associated with severe fatigue problems in service involving both root and toe cracks in fillet welds connecting the web plate to the bent portion of the flange plate. As they propagate, the cracks generally form branches, some of which propagate around the apex of the bend, and others that are more severe propagate vertically through the web plate.

Tapered Details

- By analysis, among the three dapped details considered in this project, tapered details possess the highest fatigue strength.
- By analysis, two zones of local tensile stress concentration are observed: one is located in the web plate at the apex of the bend nearer to the support and the other in the flange plate at the apex of the bend that is farther from the support.

- By analysis, considering the bend nearer to the support, the addition of welded transverse stiffener plates that join the apex of the bend to the web plate neither increases nor reduces the local concentration of stress.
- By analysis, considering the bend farther from the support, the addition of welded transverse stiffener plates that join the apex of the bend to the web plate increases the local concentration of stress.
- During fatigue testing under simulated service loading, the tapered detail did not develop fatigue cracks.
- At the time of this report, the project supervisor is not aware of instances where fatigue cracks have formed in tapered details in service.

CHAPTER 7:
RECOMMENDATIONS

The project supervisor makes the following engineering recommendations.

NOTCHED DAPPED GIRDER END DETAIL

The project supervisor does not recommend continued use of the notched dapped girder end detail in any of its forms. Existing notched girder end details should be monitored at abbreviated inspection intervals to ensure that fatigue cracks, should they form, are detected early. Particular attention should be given to the web plate at two locations: the reentrant corner at the notch and the end(s) of any welded longitudinal plates that extend away from the notch.

90-DEGREE ROUNDED DAPPED GIRDER END DETAIL

Existing Details in Service

The project supervisor recommends monitoring existing 90-degree rounded dapped girder end details at regular inspection intervals to ensure that fatigue cracks, should they form, are detected early. Particular attention should be given to the fillet welds connecting the web plate to the flange plate in the vicinity of the apex of the bent flange plate. In addition, the ends of any welded longitudinal plates that extend from the apex of the bent flange should be given attention.

Future Design

Though rigorous statistics are not available, most of the fatigue cracks observed in this detail in Japan failed at the root of the fillet weld. This fact suggests that the local stress concentration at the bent flange plate overloaded the welds. It is also possible that the welds were fabricated poorly. For example, if the fit-up between the bent flange and web is not conformal, a nominal fillet weld could become effectively overloaded even without the presence of the stress concentration. A definitive method to avoid all of these problems is to incorporate a complete joint penetration (CJP) weld to join the web plate to the bent portion of the flange plate. Specifically, the CJP weld should “begin” some distance below the vertical tangent point, continue up and around the apex of the bend, and “end” some distance beyond the horizontal

tangent point. Denote the radius of the bend by *R*. The CJP weld could "begin" a distance *R* below the vertical tangent point and "end" a distance *R* beyond the horizontal tangent point. (The words *begin* and *end* appear in quotes because this is not meant to be guidance to the fabricator regarding a preferred direction of welding.) At the ends of the CJP weld, some means should be provided for transitioning into the nominal required fillet weld.

Not all of the fatigue cracks in this detail in Japan have been root failures. There have been a number of toe failures reported, which is a failure of the web plate itself. Use of the CJP weld improves the situation for the web plate, but it is not a definitive solution. A program of fatigue testing would be the only means of determining the actual ability of the CJP weld to prevent toe failures in the web plate of this detail.

TAPERED DAPPED GIRDER END DETAIL

Existing Details in Service

The project supervisor recommends monitoring existing tapered dapped girder end details at regular inspection intervals to ensure that fatigue cracks, should they form, are detected early. Particular attention should be given to the fillet welds connecting the web plate to the flange plate in the vicinity of the apex of the bent flange plate nearer the support. Particular attention should also be given to the welds connecting any transverse stiffeners to the tension flange in the vicinity of the apex of the bent flange plate farther from the support.

Future Design

Bend Nearer to the Support

The stress concentration in the web plate at the bend nearer to the support is not as severe as in the 90-degree rounded detail, but a similar zone of elevated stress is present there. Potential problems with fit-up in the shop also exist. The designer might want to consider using a CJP weld to join the web plate to the bent portion of the flange plate, especially for steep tapers; for example, 1:1 and steeper. As in the 90-degree rounded detail, the CJP weld should "begin" and "end" away from the apex of the bend extending at least to the points of tangency and transition smoothly into the nominal required fillet weld.

Bend Farther from the Support

The local tensile stress concentration at the bend farther from the support occurs in the flange plate. The stresses normal to the weld connecting the flange plate to the web plate are compressive. Therefore, the nominal required fillet weld connection is appropriate at this location. Analyses and tests prove that the local compressive stress in the web at this location do not reduce the capacity of the girder when transverse stiffeners are omitted. In fact, welded transverse stiffeners at this location increase the tensile stress concentration in the flange plate. If intermediate transverse stiffeners are needed in the tapered region to satisfy overall strength requirements for the girder, they should be located outside of the bent portion of the flange plate.

COLD BENDING OF STEEL PLATES

The fabrication of dapped girder end details requires some form of plate bending operation to shape the flanges. In a majority of such cases, cold-bending operations are the most cost effective. The United States, however, lacks national standards and codified provisions for cold bending steel plate during bridge fabrication. In Japan, the national standard specifications for the design of steel bridges allows cold bending of steel plates for use in main members, provided that the steel material conforms to certain requirements (*23*). The project supervisor reviewed the background data underlying the Japanese requirements and concludes they can be applied safely for the design of steel bridges in the state of Texas.

The following guidelines are recommended by the project supervisor for cold bending steel plate during bridge fabrication.

15t Requirements

- The plate shall conform to the requirements of the AASHTO Bridge Design Specifications (*21*).
- The plate may be bent, without heat assistance, to a minimum inside radius equal to 15 times the plate thickness.

7t Requirements

- The plate shall conform to the requirements of the *AASHTO LRFD Bridge Design Specifications* (*21*).

- The nitrogen content of the plate shall not exceed 0.006 percent by weight.
- The Charpy impact notch toughness of the plate shall exceed 150 Joules (111 ft-lbf) at a temperature of 0°C (32°F).
- The plate may be bent, without heat assistance, to a minimum inside radius equal to seven times the thickness of the plate.

5t Requirements

- The plate shall conform to the requirements of the *AASHTO LRFD Bridge Design Specifications* (*21*).
- The nitrogen content of the plate shall not exceed 0.006 percent by weight.
- The Charpy impact notch toughness of the plate shall exceed 200 Joules (148 ft-lbf) at a temperature of 0°C (32°F).
- The plate may be bent, without heat assistance, to a minimum inside radius equal to five times the thickness of the plate.

REFERENCES

1 Farr, J. 2001. *Virtual Representation and Analysis of Structural Systems, Presented with a Case Study*. Master's thesis, Texas A&M University, College Station, TX.

2 MacNeal-Schwendler Corporation. *MSC/Patran Version 8.5.* 1998. http://sc.tamu.edu/help/softwareDocs/patran85/ (accessed January 2001).

3 Hibbitt, Karlsson, & Sorenson, Inc. *ABAQUS Standard User's Manual Vol. I-III. Version 5.8*. 1998. Pawtucket, RI.

4 Federal Highway Administration. 1996. *Traffic Models Handbook*.

5 Aycin, M.F., and R.F. Benekohal. 1999. Comparison of Car Following Models for Simulation, Preprint, 78th Transportation Research Board Annual Meeting, Washington, D.C.

6 Rilett, L.R., K. Kim, and B. Raney. 2000. A Comparison of the Low Fidelity TRANSIMS and High Fidelity CORSIM Highway Simulation Using ITS Data. *TRB 00-0678*. College Station, TX: Transportation Research Board.

7 ITT Systems and Science Corporation. 1998. *CORSIM User's Guide.* Contract No. DTFH61-97-C-00055, FHWA, U.S. Department of Transportation, Washington, D.C.

8 Dixon, M., and L.R. Rilett. 1999. Evaluation of ITS Automatic Vehicle Identification Information for Origin-Destination Estimation, Preprint 991459, 78th Transportation Research Board Annual Meeting, Washington, D.C.

9 Cheu, R.L., X. Jin, K.C. Ng, Y.L. Ng, and D. Srinivasan. 1998. Calibration of FREESIM for Singapore Expressway Using Genetic Algorithm. *ASCE Journal of Transportation Engineering,* December, pp. 526-535.

10 Prevedouros, P., and Wang, Y. 1999. Simulation of a Large Freeway/Arterial Network with CORSIM, INTEGRATION and WATSim, Preprint, 78th Transportation Research Board Annual Meeting, Washington, D.C.

11 American Society for Testing and Materials. 1994. *Standard Specification for Highway Weigh-in-Motion (WIM) Systems with User Requirements and Test Method (E 1318-94)*. Philadelphia, PA.

12 Texas Department of Transportation. 2000. *Weigh-In-Motion System, Traffic Data Collection, Type II, Piezoelectric, Fixed and Portable* (TxDOT 780-95-91). Austin, TX.

13 Findley, W.N. 1959. A Theory for the Effect of Mean Stress on Fatigue of Metals under Combined Torsion and Axial Load or Bending. *Journal of Engineering for Industry,* 81(4): 301-306.

14 Fry, G.T., F.V. Lawrence, and A.R. Robinson. 1996. A Model for Fatigue Defect Nucleation in Thermite Rail Welds, *Fatigue & Fracture of Engineering Materials & Structures: The International Journal,* Vol. 19, No. 6.

15 Bannantine, J.A., J.J. Comer, and J.L. Handrock. 1990. *Fundamentals of Metal Fatigue Analysis*. Englewood Cliffs, NJ: Prentice-Hall, Inc.

16 Elliott, J. 2001. *Shear Capacity of Dapped Ended Steel Plate Girders*. Master's thesis, Texas A&M University, College Station, TX.

17 Hibbitt, Karlsson, and Sorenson, Inc. 1998. *ABAQUS Theory Manual Version 5.8.* Pawtucket, RI.

18 American Welding Society (ASW). 1996. *AWS Bridge Welding Code (Annex IV)*. Miami, FL.

19 Galambos, T. 1998. *Structural Stability Research Council Guide to Stability Design Criteria for Metal Structures* (fifth ed.). New York: John Wiley & Sons.
20 Lee, S., and Yoo, C. 1998. Strength of Plate Girder Web Panels under Pure Shear. *ASCE Journal of Structural Engineering,* 124(2): 184-194.
21 AASHTO. 2004. *AASHTO LRFD Bridge Design Specifications* (third ed.).
22 Pengphon, Saturn, Chitoshi Miki, Shuichi Ono, Tetsuhiro Shimozato, and Atsushi Shibuya. 2004. Cause Identification of Fatigue Cracks in Plate Girder-on-Steel Frame Pier Bridge. *Japan Society of Civil Engineers, Journal of Structural Mechanics and Earthquake Engineering,* 21(1): 43s-56s.
23 Japan Road Association. March 2002. *Specifications for Highway Bridges Part I: Common*. In Japanese. p. 110, Selection of Steel, Section 1.6.2.3, and p. 112, Commentary to Section 1.6.2.3.